Dipl.-Ing. Bernd Oberdorfer

Atomic Free Volume in Bulk Nanocrystalline Metals studied by Dilatometry and Positron Annihilation

DOCTORAL THESIS

for obtaining the academic degree of
Doktor der technischen Wissenschaften

Doctoral Programme Technical Physics

Graz University of Technology

Supervisor:
Univ.-Prof. Dr. Roland Würschum
Institute of Materials Physics

Graz, March 2012

Eidesstattliche Erklärung

Ich erkläre an Eides statt, dass ich die vorliegende Arbeit selbständig verfasst, andere als die angegebenen Quellen/Hilfsmittel nicht benutzt, und die den benutzten Quellen wörtlich und inhaltlich entnommenen Stellen als solche kenntlich gemacht habe.

Graz, am ....

Unterschrift

Statutory Declaration

I declare that I have authored this thesis independently, that I have not used other than the declared sources/resources, and that I have explicitly marked all material which has been quotes either literally or by content from the used sources.

....

date signature

Abstract

Atomic free volume – a key parameter in the characterization of bulk nanocrystalline materials – is known to exist in high excess concentration in severely plastically deformed metals. For the purpose of analyzing free volume-type defects, such as vacancies, dislocations, and grain boundaries, samples of Fe, Ta, Ni, and Cu were deformed by means of high-pressure torsion (HPT).

The HPT deformed samples were investigated mainly by the method of high-precision difference dilatometry, which represents a novel approach in the characterization of excess free-volume defects. For all analyzed samples high absolute concentrations of excess free volume of the order of some 10^{-3} could be determined. Making use of crystallite size data obtained from electron microscopy, the amount of free volumes localized at the different lattice defects could be estimated. In the case of Ni and Cu, where defect annealing occurred in several sub-stages, specific defects could be discerned according to their corresponding annealing stage. In particular, the fundamental parameter of grain boundary excess volume e_{GB}, i.e., the volume expansion of a grain boundary, could be revealed. Values of $e_{\mathrm{GB}} = 36\,\mathrm{pm}$ and $e_{\mathrm{GB}} = 34\,\mathrm{pm}$ for Ni and Cu were obtained, respectively. Furthermore, defect kinetics was studied by variation of the dilatometric heating rate. By means of Kissinger- and JMAK-type analysis, activation energies for the recrystallization were determined in good agreement with literature data. Finally, a characteristic anisotropy of the length change with respect to the sample orientation could be found which, in the case of Ni, could be correlated with the shape anisotropy of the crystallites. A vacancy relaxation model, potentially explaining this issue, was presented.

The complementary method of positron annihilation Doppler broadening measurements at the positron beam of the FRMII, Garching, clearly identified the annealing of atomic free volume defects, supporting the annealing characteristics deduced from dilatometry. Further characterization of the open volume defects were performed by means of positron lifetime spectroscopy.

In conclusion, the combination of the macroscopic approach of dilatometry and the microscopic approach of positron annihilation brought a more profound understanding of the complex atomic defect structure of bulk nanocrystalline metals.

Contents

1 Introduction

Over the last decade bulk nanocrystalline metals have gained growing interest due to their substantially improved material properties and the associated great potential for applications [1–3]. An excellent method for the production of bulk nanocrystalline metals is high pressure torsion (HPT), as it allows continuous severe plastic deformation up to very high strains [4, 5].

Nanocrystalline materials in general are characterized by a high concentration of structural atomic defects. Inherent to these structural defects, such as vacancies, dislocations and grain boundaries, is free volume, an excess volume compared to the perfect crystal lattice. These free volume-associated defects play a decisive role in the atomic processes occurring during severe plastic deformation but also highly affect the physical properties of the deformed material itself. Free volumes are directly related to the grain boundary energy [6] and the atomic self-diffusion [7].

The issue of free volume is particularly relevant in HPT processed nanocrystalline metals, as there are are evidences for high vacancy concentrations as well as high dislocation densities in HPT-Cu and Ni [8, 9]. These materials are gaining interest not only

since they can be produced in ever-increasing dimensions [10]. However, specific studies for the determination of the absolute free volume concentration in plastically deformed metals are rare and difficult to realize. This represents the starting point for the present work, approached by means of especially two methods, namely high-precision difference dilatometry and positron annihilation spectroscopy. The investigated materials were Fe and Ta as well as Ni and Cu as bcc and fcc model systems, respectively.

The characterization of non-equilibrium excess free volume in solids by means of difference dilatometry represents a novel access, only feasible since length change measurements can be performed with sufficient high precision. The greatest advantage over other methods is the possibility to determine the absolute concentration of free volumes in HPT deformed materials. Since difference dilatometry operates with linear heating, measurements with different heating rates allow the analysis of defect and recrystallization kinetics, with the benefit of discerning the individual defects according to their different annealing stages. Consequently, important parameters such as vacancy concentration or dislocation density can be specified. In particular, difference dilatometry is used in the present work to determine the grain boundary excess volume, a fundamental parameter for the physics of grain boundaries.

An ideal complement to the macroscopic dilatometric measurements is the microscopic approach of positron annihilation. Doppler broadening of positron-electron annihilation radiation and positron lifetimes spectroscopy yield specific information on vacancies, dislocations and grain boundaries. For the purpose of studying the fast defect annealing kinetics of severely plastically deformed metals the high-intensity positron beam at the neutron source FRMII of the TU Munich, was employed for the first time. The combination of high-precision dilatometric measurements with *in-situ* positron annihilation spectroscopy provides a deep insight in the constitution and annealing of the complex atomic defect structure of bulk nanocrystalline metals.

This work was realized in cooperation with:

- Erich Schmid Institute of Materials Science, Austrian Academy of Sciences, Leoben, Austria.
- Physics of Nanostructured Materials, Faculty of Physics, University of Vienna, Austria.
- Physics Department E 21 and FRM II, Technical University Munich, Garching, Germany.

Parts of this dissertation are already published in the following journals:

- B. Oberdorfer, B. Lorenzoni, K. Unger, W. Sprengel, M. Zehetbauer, R. Pippan and R. Würschum, Absolute concentration of free volume-type defects in ultrafine-grained Fe pre-pared by high-pressure torsion, *Scripta Mater.* **63** (2010) 452-455.
- B. Oberdorfer, E.-M. Steyskal, W. Sprengel, W. Puff, P. Pikart, C. Hugenschmidt, M. Zehetbauer, R. Pippan and R. Würschum, *In-situ* probing of fast defect annealing in Cu and Ni with a high-intensity positron beam, *Phys. Rev. Lett.* **105** (2010) 146101-1 - 146101-4.
- B. Oberdorfer, E.-M. Steyskal, W. Sprengel, R. Pippan, M. Zehetbauer, W. Puff and R. Würschum, Recrystallization kinetics of ultrafine-grained Ni studied by dilatometry, *J. Alloys Comp.* **509** (2011) 5309-5311.
- E.-M. Steyskal, B. Oberdorfer, W. Sprengel, M. Zehetbauer, R. Pippan and R. Würschum, Direct Experimental Determination of Grain Boundary Excess Volume in Metals, *Phys. Rev. Lett.*, accepted: Nov 28, 2011.
- R. Würschum, B. Oberdorfer, E.-M. Steyskal, W. Sprengel, W. Puff, P. Pikart, C. Hugenschmidt and R. Pippan, Free volumes in bulk nanocrystalline metals studied by the complementary techniques of positron annihilation and dilatometry, *Physica B*, accepted: Jan 11, 2012.

2

Basics & State of Research

The attractive potential of **bulk nanocrystalline metals** can be traced back to their improved material properties such as increased strength in combination with good ductility. For the production of bulk nanocrystalline metals the "top-down" approach, i.e. the processing of initially coarse-grained materials by severe plastic deformation (SPD) is the most prospective [1–3].

The most common SPD methods are high-pressure torsion (HPT) and equal channel angular pressing (ECAP). HPT utilizes high hydrostatic pressure for avoiding cracks and voids and facilitating structural refinement upon deformation [4, 11].

A central parameter in affecting material properties is **free volume**, i.e., the excess volume compared to the perfect lattice of a single crystal. The free volume in a real polycrystal can be localized at structural defects like vacancies, dislocation or grain boundaries.

A high vacancy concentration in SPD-processed materials was indirectly concluded by Sauvage et al. [12, 13] analyzing the solubility of Fe clusters in Cu-Fe and by Mazilkin et al. [14] explaining the process of demixing in supersaturated Al alloys.

Evidence for vacancies in SPD-processed pure metals could also be obtained by means of X-ray line profile analysis (XPA), electrical resistometry (RER), and differential scanning calorimetry [8, 15, 16]. These studies indicate a vacancy concentration in the order of magnitude of 10^{-4}, being significantly higher than the equilibrium concentration. This value is in good accordance with theoretical considerations on the athermal production of vacancies and their influence in fatigue experiments [17]. In the above mentioned studies Refs. [8, 15, 16] also very high dislocations densities of the order of $10^{15}\,\mathrm{m}^{-2}$ could be observed.

The observed grain sizes of SPD-processed metals, ranging from the nanometer- to the ultra-fine-grained regime, manifest a high number of grain boundaries. The amount of free volume localized at grain boundaries – the **grain boundary excess volume** – is therefore a fundamental parameter for the characterization of nanocrystalline metals. This excess volume correlates directly to the grain boundary energy [6] and is of importance for the grain boundary diffusion and segregation [7] as well as for the grain boundary electrical resistance [6].
In addition to the issue of excess free volume localized at conventional grain boundaries, there are evidences for non-equilibrated grain boundary structures, discernible by enhanced diffusivities in these metals as determined by tracer diffusion studies [18–22]. Upon annealing at slightly elevated temperatures, decreased diffusivity values of conventional grain boundaries were observed. There are strong indications that this structural relaxation of the non-equilibrium grain boundaries is connected to the annealing of free volume in these SPD-processed metals [19].

Despite the relevance of free volumes described above, direct and specific studies of

the type, amount and kinetics of free volume in SPD materials are scarce. A novel approach for this purpose is the method of **high-precision dilatometry**.

In the 1960s already Simmons and Balluffi used differential dilatometry to specify experimentally the concentration of vacancies in thermal equilibrium in Al, Au and Cu [23–26] based on an idea of Feder and Novick [27]. In these measurements the relative expansions of the lattice constant $\Delta a/a$ (by means of X-rays) as well as of the macroscopic length $\Delta\ell/\ell$ were determined simultaneously upon annealing up to the melting point. At high temperatures near the melting point, a difference between $\Delta a/a$ and $\Delta\ell/\ell$ due to the formation of additional lattice sites – taken up by thermal vacancies – could be observed. The vacancy concentration amounts to $C_\mathrm{v} = 3 \cdot (\Delta\ell/\ell - \Delta a/a)$ assuming isotropic distribution of sources and sinks of vacancies.

In contrast to differential dilatometry *time-dependent* dilatometry is able to characterize defect kinetics. This was applied for intermetallic compounds with high vacancy migration enthalpies using a 2-beam laser interferometer [28]. These high enthalpies give rise to long equilibration times after rapid temperature changes, enabling studies of the concentration as well as formation and migration enthalpies of vacancies. Time-dependent dilatometry was also applied for measurements of the reversible relative length changes in Zr-Cu-Ni-Nb-Al bulk metallic glass yielding the excess free volume at the glass transition [29].

For the determination of *irreversible* length changes due to free volume annealing in this work, a time-dependent difference dilatometer (not to be confused with the differential dilatometry experiments of Simmons and Balluffi) is employed for the first time. (For an extensive description of the high-precision difference dilatometer see Sec. 3.2.1.) The simultaneous length change measurements upon linear heating of a HPT-deformed and an undeformed reference sample enables the separation of the irreversible shrinkage from the reversible thermal expansion. The irreversible shrinkage

– being due to defect annealing upon heating – is directly visible in the difference curve of the two simultaneous measurements. In contrast to the other dilatometric techniques, the difference dilatometry allows the analysis of all free-volume associated defect types, not only vacancies [30]. Hence, also dislocations and grain boundaries in the relaxed as well as in the non-relaxed state can be studied. A distinction of all these defects is moreover possible, in the case that their annealing occurs in different temperature stages. With knowledge of the grain sizes in the individual stages, fundamental parameters such as the grain boundary excess volume can be determined directly [31]. In addition, the possibility of varying the linear heating rate offers an analysis of defect kinetics, applying thermal analysis methods [32].

To the same degree **positron annihilation spectroscopy** represents a powerful analysis method for the characterization of nanomaterials, allowing the determination of the different types of structural defects as well as the kinetics of these defects upon annealing. For this purpose the positrons – being trapped into defects like vacancies, dislocations and grain boundaries – can be analyzed regarding the energy of their annihilation γ-quanta (Doppler broadening spectroscopy) or their lifetimes prior to annihilation (positron lifetime measurements, see Sec. 3.3).

In 1988 already Schaefer et al. [33] investigated nanocrystalline Fe by means of positron lifetime measurements. Since this pioneering era systematical positron annihilation studies regarding structural free volume were performed in a variety of nanomaterials synthesized by different methods such as cluster condensation [34], SPD [35], ball-milling [36] or crystallization of amorphous alloys [37]. More recent studies [38, 39] investigated SPD processed alloys by means of 2-dimensional Doppler broadening spectroscopy. Furthermore a modeling of diffusion-limited positron trapping at grain boundaries in nano- to micrometer-grained materials is given in [40, 41].

Positron studies of other groups on SPD processed metals were performed e.g. by

Čížek et al. [42, 43], by Van Petegem et al. [44] and by Krause-Rehberg et al. [45]. Not least these studies underscore the significance of positron annihilation for the characterization of SPD processed materials.

In this work for the first time the annealing of structural defects in HPT-Ni and Cu was analyzed *in-situ*, using the high-intensity positron beam of the positron source NEPOMUC at the Heinz-Meier Leibnitz neutron reactor (FRMII, Garching, Technical University Munich, see Sec. 3.3.2). The high intensity of the positron beam allows measurements of Doppler broadening spectra in the time scale of minutes, fast enough in order to capture the annealing process. A successful combination of the positron annihilation technique with dilatometry was achieved by applying for both methods the identical temperature program on identically prepared samples. This direct correlation of the microscopic approach of positron annihilation and the macroscopic of dilatometry allow the clear identification of free volume defects [46].

3 METHODS

3.1 High Pressure Torsion

For the production of bulk nanocrystalline metals the SPD method of high pressure torsion (HPT) was applied in the present work [4, 11]. This deformation method, with the benefit of achieving very large strains easily, gains interest not only since HPT samples can prepared in increasingly large dimensions [47].

In principle the HPT process is a shear deformation between two anvils of which one is rotated. Onto the disc-shaped billet between the anvils a hydrostatic pressure up to 6 GPa is applied to avoiding sliding during deformation. Fig. 3.1 illustrates the HPT processing by means of a scale model of the large HPT facility installed at the Erich-Schmid Institute, Austrian Academy of Sciences, Leoben, Austria. The usable sample size is 30 mm in diameter and 7 mm in height.

In addition to the large HPT facility a smaller one is available, which is able to handle sample sizes up to 14 mm and which is also equipped with a measuring unit of the tor-

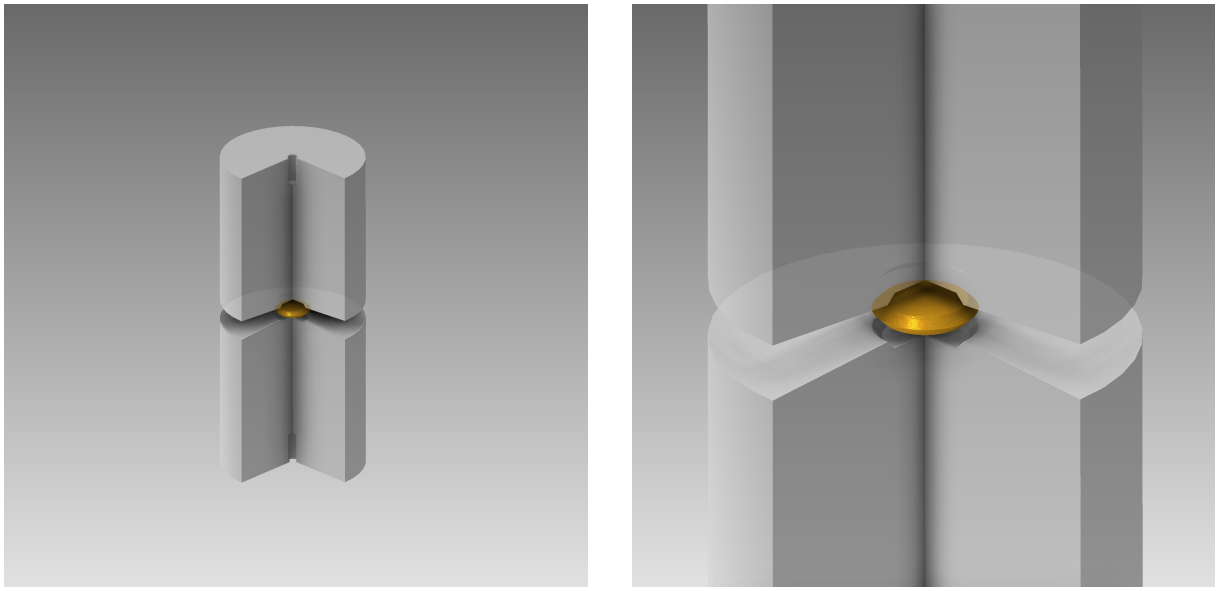

Figure 3.1: Left: sectional scale model of the HPT facility. Right: detailed view with the disc-shaped billet between two steel anvils. The dimensions of the billet are 30 mm in diameter and 7 mm in height.

sional moment. Further measured parameters are rotational speed and time. The torsional moment of the anvils can be plotted as a function of the equivalent strain, which can be used to determine the saturation deformation of HPT metals (see Fig. 4.15). For an extensive description of the HPT facilities see [10].

Prior to HPT deformation the samples were pressed into the disc-shaped gap between the anvils and thereafter annealed in high vacuum for 1 hour at a homologous temperature of 0.5 - 0.6 to ensure recovery from upsetting. In the case of Ta only ca. $0.3\,T_{\mathrm{m}}$ was reached due to the high melting point of Ta. For sufficient friction between anvils and sample, the samples were sandblasted after annealing. During deformation the disc slightly flattens, losing some material in radial direction. Nevertheless, this procedure well approximates the idealized HPT deformation, i.e., that without any change of the sample geometry [10].

Upon deformation a structural refinement sets in, beginning with the formation of dislocations. These dislocations get assembled, at first at grain boundaries, later also within the grains, forming cell blocks with different orientations. With increasing strain the misorientation increases and new grain boundaries are formed. Finally a saturation in refinement is reached (for pure metals) resulting in a uniform granular microstructure [5]. This saturation microstructure is the smallest achievable and does no longer get refined with increasing strain. Furthermore the original grain structure disappears completely, so that at very high strains greater than $\varepsilon = 32$ an initially single crystal sample is hardly discernible from that of a polycrystal [48].

The shear angle γ and the equivalent strain $\varepsilon_{\mathrm{eq}}$ achieved by means of HPT can be calculated by (according to [5])

$$\gamma = \frac{2\pi r n}{h} \quad , \tag{3.1}$$

$$\varepsilon_{\mathrm{eq}} = \frac{\gamma}{\sqrt{3}} \quad , \tag{3.2}$$

with r the radius in the HPT disc, n the number of HPT revolutions, and h the height of the disc. Due to the lateral dimensions of the sample, an uncertainty $\Delta\varepsilon_{\mathrm{eq}}$ arises, which is calculated by assuming a radius uncertainty of $\Delta r = 1\,\mathrm{mm}$.

The microstructure is obviously radius-dependent for equivalent strain values $\varepsilon_{\mathrm{eq}}$ below the saturation deformation as demonstrated by means of scanning electron micrographs of HPT-Ta with 1 revolution at different radii (see below, Fig. 4.13).

Regarding the homogeneity of the saturated microstructure, coarse-grained structures and reduced microhardness in the near-surface part of HPT-Fe discs were observed [49]. However, these surface regions were removed for the present measurements. The samples of HPT-Cu were stored in a freezer prior to measurements, to prevent anticipated defect annealing.

3.2 Dilatometry

3.2.1 Principle

The primary method of measurement in this work is difference dilatometry employing a high precision dilatometer (Linseis, L75VD500 LT) in vertical set-up. This method allows measurements of the irreversible length change due to the annealing of free volume. Fig. 3.2 exhibits schematically the principle of difference dilatometry. By means of simultaneous length change measurement of a HPT-deformed and an undeformed sample the length change difference $\Delta\ell_{\mathrm{v}}$ upon linear heating is determined. Since the two samples are of the same material, the superimposed length change $\Delta\ell_{\mathrm{t}}$ due to the thermal expansion cancels out. Hence, $\Delta\ell_{\mathrm{v}}$ arising upon heating is due to the annealing

of deformation-induced excess free volume. The quantity used for further considerations is the net relative length change difference $\Delta\ell/\ell_0$:

$$\frac{\Delta\ell}{\ell_0} = \left.\frac{\Delta\ell}{\ell_0}\right|_{\text{sample}} - \left.\frac{\Delta\ell}{\ell_0}\right|_{\text{reference}} \tag{3.3}$$

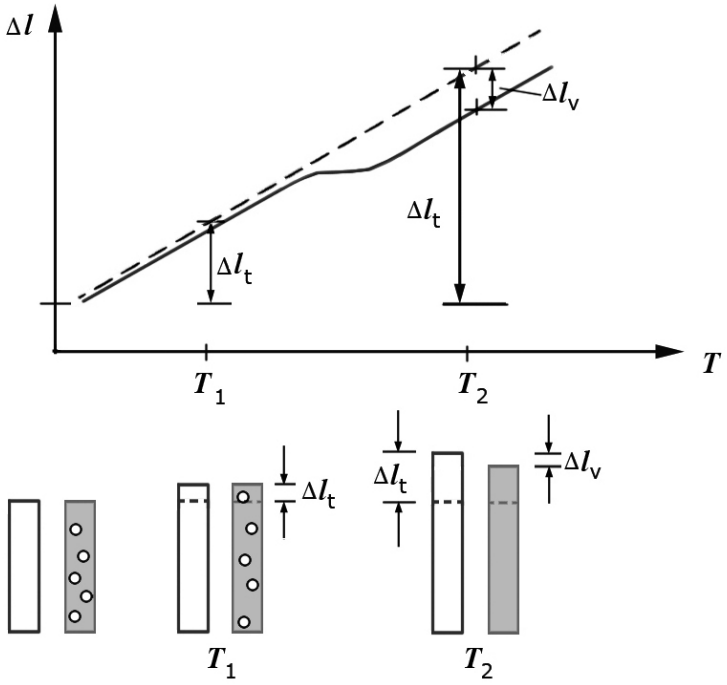

Figure 3.2: Principle of the difference dilatometric measurement of an HPT-deformed sample (shaded) and an undeformed reference (white) upon linear heating. Superimposed to the thermal expansion $\Delta\ell_\mathrm{t}$ is the irreversible length change difference $\Delta\ell_\mathrm{v}$, arising due to the annealing of HPT-induced defects. Picture taken from [50], courtesy of Elsevier Ltd.

With the assumption that the deformation-induced defects anneal out isotropically, the total annealed free volume $\Delta V/V_0$ can be approximated by

$$\frac{\Delta V}{V_0} \approx 3 \cdot \frac{\Delta \ell}{\ell_0} \quad , \tag{3.4}$$

$\Delta\ell/\ell_0$ being the difference of the relative length changes of the HPT and reference sample. Apart from vacancy-type defects the free volume of a HPT-deformed sample can be localized at dislocations and grain boundaries.

According to Hirth and Lothe [51] the excess free volume of dislocations

$$\left.\frac{\Delta V}{V_0}\right|_{\text{disl}} = 0.5 \cdot b^2 \rho_{\text{disl}} \tag{3.5}$$

is related to the dislocation density ρ_{disl} and the magnitude of the Burgers vector

$$b = \|\vec{b}\| = \frac{a}{2}\sqrt{h^2 + k^2 + l^2}\,, \tag{3.6}$$

where a denotes the lattice constant and h, k, and l the Miller indices of the Burgers vector. For bcc and fcc metals $\vec{b}$ parallel to $\langle 111 \rangle$ and $\langle 110 \rangle$, respectively.

The free volume associated with grain boundaries (GB)

$$\left.\frac{\Delta V}{V_0}\right|_{\text{GB}} = 3 \cdot e_{\text{GB}} \left(\frac{1}{d_{\text{initial}}} - \frac{1}{d_{\text{final}}} \right) \tag{3.7}$$

can be calculated from the removal of GBs in the wake of crystallite growth. e_{GB} denotes the grain boundary excess volume, and d_{initial} and d_{final} the grain diameter at the beginning and at the end of the grain growth, respectively.

Fig. 3.3 a) shows the setup of the Linseis dilatometer with the Ar flow meter on the right and the inlet for the liquid nitrogen on the left. In b) the opened measuring unit

(a) Linseis L75VD500 dilatometer

(b) Dilatometer measuring unit

Figure 3.3: Linseis dilatometer. (a) Front view with the inlets for argon gas and liquid nitrogen. (b) Detailed view of opened measuring unit with two vertical push rods and thermocouple element in the background.

with two vertical quartz rods pushing on sample and reference is visible. Directly behind the push rods the thermocouple element for a direct temperature measurement is located.

The measuring principle according to Fig. 3.2 is exemplary demonstrated by the measurement of Fig. 3.4 which shows the relative length change of a deformed HPT-Fe sample and of a well-annealed Fe reference sample upon linear heating and cooling with a constant rate of $3\,\mathrm{K/min}$. An irreversible relative length change difference opening up upon the first heating cycle can be observed. Subtracting the length change of the deformed from that of the undeformed sample, the irreversible shrinkage of the deformed sample due to the annealing of excess free volume becomes visible. The fact, that both samples behave the same in the second heating cycle, proves the irreversibility of the annealing process.

For the error analysis of this method, measurements under the same conditions but without any samples were performed. As shown in Fig. 3.5 the maximum absolute deviation between the two blank push rods amounts to $87\,\mathrm{nm}$. Related to a mean sample length of $7\,\mathrm{mm}$ this yields a relative length change error $\Delta(\Delta\ell/\ell_0)$ of 1.2×10^{-5}.

The relative length change difference of one and the same reference sample, obtained from two subsequent measurements amounts to $\Delta(\Delta\ell/\ell_0) = 6 \times 10^{-5}$ (shown in [52]). This 5 times higher error clearly demonstrates the advantage of simultaneous measurements.

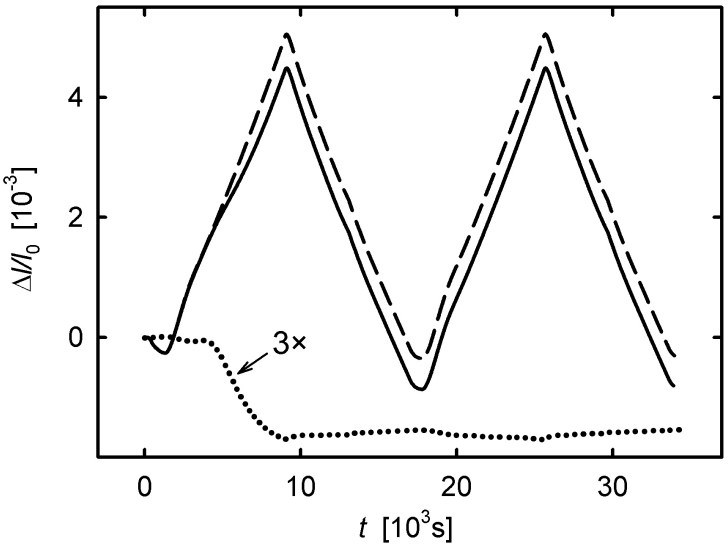

Figure 3.4: Relative length change $\Delta\ell/\ell_0$ of HPT-Fe (—) and of a well-annealed Fe reference sample (- - -) upon linear thermal cycling with 3 K/min. The difference between the deformed and the undeformed sample ($\cdots$) represents the irreversible shrinkage due to the annealing of structural defects.

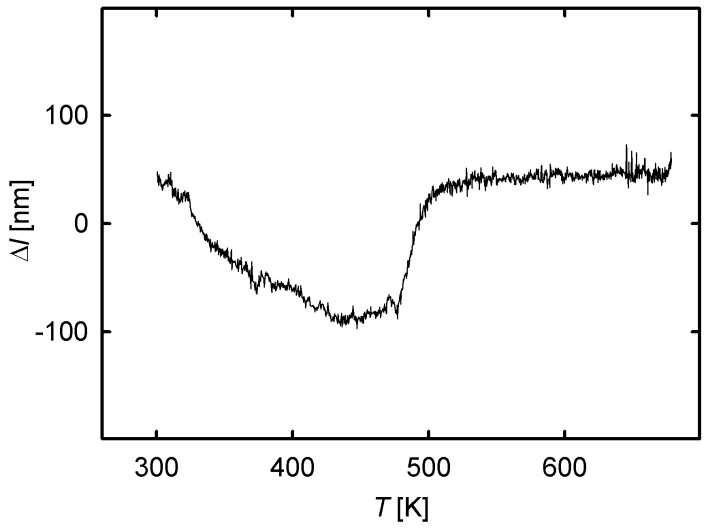

Figure 3.5: Test of measuring accuracy. Length difference obtained from a reference measurement performed without samples with the blank push rods being in contact with the base plate of the sample holder. The maximum absolute length change difference of 87 nm corresponds to an error of $\Delta(\Delta\ell/\ell_0) = 1.2 \times 10^{-5}$ for a sample length of 7 mm.

3.2.2 Calibration

For precise kinetic studies based on variations of the heating rate, any apparatus-inherent temperature lag has to be carefully taken into account. For this purpose, calibration measurements[1] were performed by making use of the Curie temperature T_C of the ferro- to paramagnetic phase transition of high-purity Ni [54]. This heating rate-independent phase transition is characterized by a λ-shaped peak in the relative length change curve, arising from a change of the thermal expansion coefficient at the phase transition [55]. Applying higher heating rates, a shift of the λ-shaped peak to higher temperatures could be observed. Fig. 3.6 exhibits this apparent Curie temperature as a function of the heating rate.

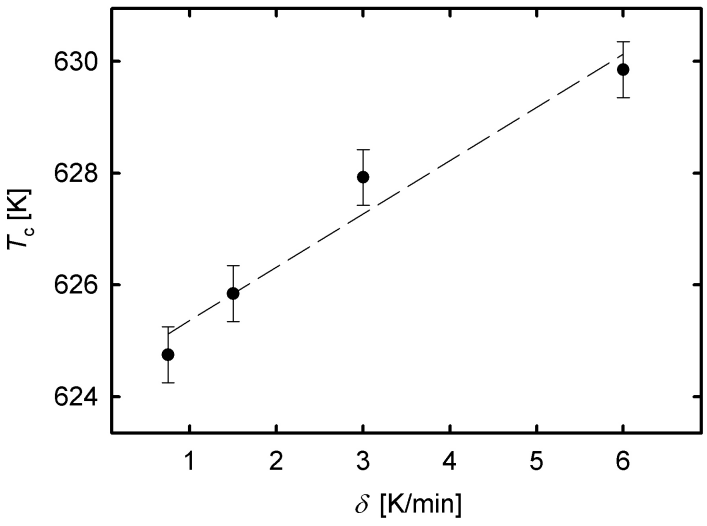

Figure 3.6: Calibration of the dilatometer. Shift of the apparent Curie temperature T_C of high-purity Ni with the heating rate δ of 0.75, 1.5, 3 and 6 K/min; (- - -) indicating the regression line.

[1] The measurements, evaluations and discussions regarding the calibration of the dilatometer were done by Katrin Unger within the framework of her bachelor thesis under my co-supervision [53].

The regression line yields $0.95\,\delta\,[\mathrm{K\,min^{-1}}] + 624.7\,\mathrm{K}$. Thus, the negative slope $-0.95\,\delta$ is directly the required relative correction for all temperatures determined by dilatometry upon linear heating with a heating rate of δ. The y-axis intercept of the regression line corresponds to the real Curie temperature which, however, is slightly lower than the literature value of $631.4\,\mathrm{K}$ [56]. However, the Curie temperature is strongly depending on the sample purity and, furthermore, for most evaluations of dilatometric results the absolute temperature is not required. Therefore, the following correction was applied in order to determine the temperature T from the temperature T_m measured at the heating rate δ: $T = T_\mathrm{m}(1 - 0.95\,\delta\,[\mathrm{K\,min^{-1}}])$.

3.2.3 Orientation and sample preparation

Dilatometric and electron microscopy investigations were performed on different orientated samples. In Fig. 3.7 the orientation of the electron microscopy samples is defined, according to the viewing direction (axial, tangential and radial) in relation to the HPT deformation axis.

For dilatometry prism-shaped samples with dimensions of $3 \times 3 \times 7\,\mathrm{mm^3}$ were prepared. The dilatometric samples are defined with regard to the direction of the relative length measurement as depicted in Fig. 3.8. In the preparation process special attention was paid to the plane-parallelism of the top and bottom plane of the sample. Fig. 3.9 shows a cut HPT-Fe disc with dilatometry samples prepared in axial direction.

3.2.4 Kissinger analysis

For the analysis of the thermally activated annealing processes the method of H. E. Kissinger [57] can be applied. The shift of the temperature of the maximum transformation rate with the heating rate can be evaluated by means of an Arrhenius-type plot, resulting in the activation energy Q of the annealing process. Starting from the equation [57]

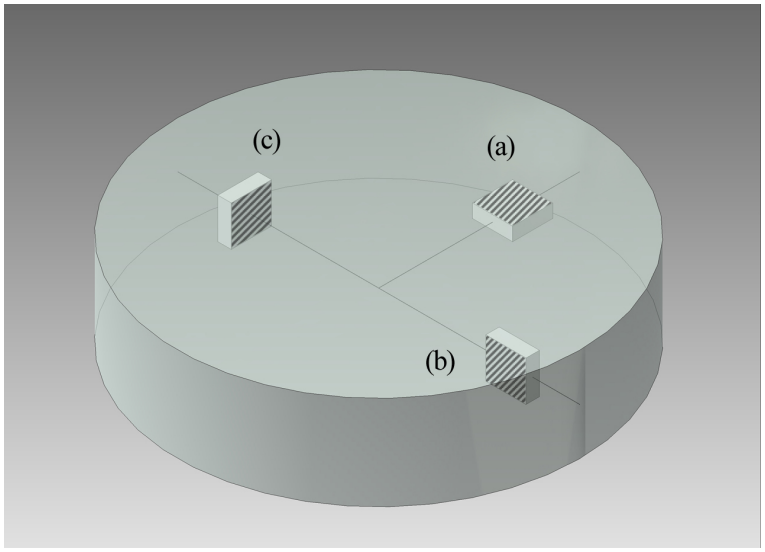

Figure 3.7: Definition of the viewing direction in the HPT discs: (a) axial, (b) tangential, and (c) radial direction in relation to the HPT axis, the hatched area indicating the plane of the samples examined by electron microscopy.

$$A \cdot \exp\left(-\frac{Q}{k_{\mathrm{B}} T_{\mathrm{p}}}\right) = \frac{\delta\, Q}{k_{\mathrm{B}} T_{\mathrm{p}}^2} \quad , \tag{3.8}$$

with A the pre-exponential frequency factor, T_{p} the peak temperature of the maximum transformation, δ the heating rate and k_{B} the Boltzmann constant, the equation for the so-called Kissinger plot reads as:

$$\ln \frac{\delta}{T_{\mathrm{p}}^2} = -\frac{Q}{k_{\mathrm{B}} T_{\mathrm{p}}} + d \quad . \tag{3.9}$$

Varying δ causes a shift of the temperature peak of the maximum transformation T_{p}. The Kissinger plot is a semilog plot of $\ln(\delta/T_{\mathrm{p}}^2)$ as a function of $1/T_{\mathrm{p}}$. Hence, the slope of the linear regression line represents $-Q/k_{\mathrm{B}}$. The y-axis intercept d is related to the pre-exponential frequency factor A with $A = Q \cdot \exp(d)/k_{\mathrm{B}}$.

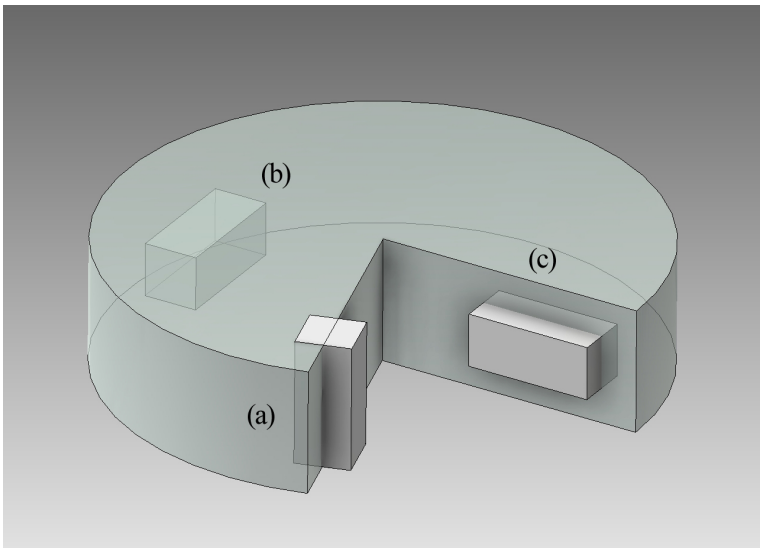

Figure 3.8: Scheme of a HPT-disk (diameter: 30 mm, height: 7 mm) with the dilatometric samples (dimensions: $3 \times 3 \times 7\,\mathrm{mm}^3$) in (a) axial, (b) tangential, and (c) radial direction in relation to the HPT axis.

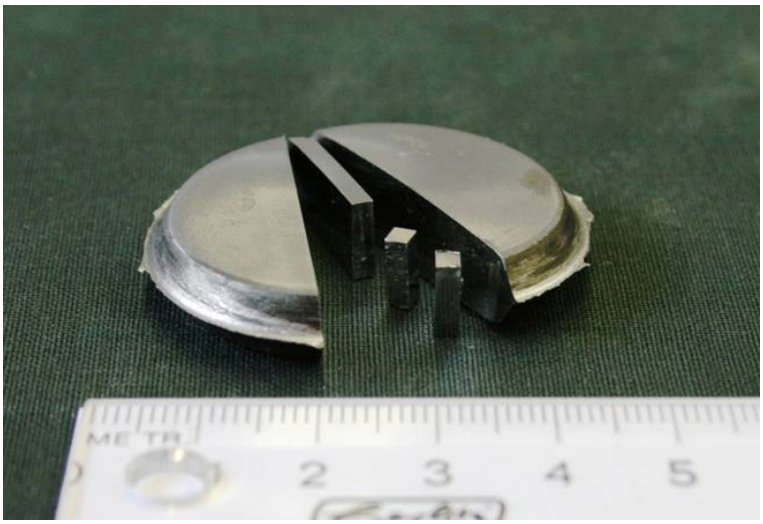

Figure 3.9: HPT-Fe disc cut in half together with dilatometric samples prepared in axial direction.

In combination with dilatometry the Kissinger analysis in this work is used for the determination of recrystallization activation energies of HPT-deformed materials.

A more sophisticated analysis basing on the theory of Johnson, Mehl, Avrami, and Kolmogorov, which takes also into account the shape of the dilatometric difference curves is presented in Sec. 4.3.4.

3.3 Positron Annihilation

Positron (e^+) annihilation spectroscopy has proven being a powerful technique for the analysis of structural defects in SPD materials [39]. For this work the methods of positron annihilation lifetime spectroscopy (PALS) for defect characterization and of *in-situ* coincident Doppler-broadening measurements (CDB) for the annealing kinetics were employed.

3.3.1 Standard laboratory technique

The PALS measurements were performed in the standard laboratory technique using a conventional ^{22}Na positron source in sandwich geometry, i.e., the source is placed between two identical samples. The positron lifetime is measured by means of $\gamma\gamma$-coincidence technique using the $1.28\,$MeV γ-quantum of ^{22}Ne as start signal and the $511\,$keV e^+e^--annihilation quantum as stop signal.
The resulting positron lifetime spectra of ca. 5×10^6 counts were evaluated by means of the program "pfposfit" [58]. The measurements were performed with a time resolution of $220\,$ps. The contribution of e^+ annihilation in the source material and the source carrier (Al foil) to the total annihilation was deducted, applying a source correction. The correction regarding the source material was $690\,$ps with $6\,\%$ for the HPT-Fe and Ta measurements and $350\,$ps with $6\,\%$ in the case of Ni and Cu. For the aluminium foil an appropriate correction of $250\,$ps with 14 and $19\,\%$, was applied, respectively.

3.3.2 High intensity positron beam

The *in-situ* Doppler broadening experiments were performed at the positron source NEPOMUC of the Heinz-Meier Leibnitz neutron reactor (FRMII, Garching, Technical University Munich). The principle of positron generation is illustrated in Fig. 3.10. Thermal neutrons are captured in ^{113}Cd which gives rise to high-energy γ-radiation. The positrons are generated by means of pair production. These initially fast e^+ are moderated in platinum resulting in an intensity of 9×10^8 positrons per second at an energy of 1 keV. The intensity of the remoderated beam used for the annihilation experiments amounts to 5×10^7 positrons per second [59].

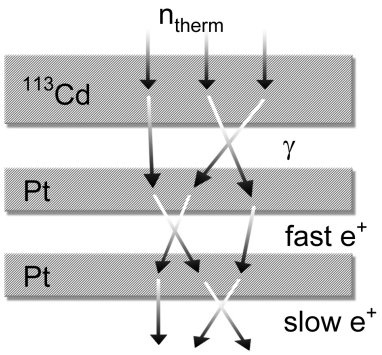

Figure 3.10: Principle of positron generation at the FRMII, TU Munich. Thermal neutrons are captured in ^{113}Cd under emission of high-energy γ-radiation, causing e^+e^--pair production in platinum. The fast e^+ are moderated in another platinum foil.

This high-intensity positron beam has been applied for the first time to study fast defect annealing kinetics on a timescale of minutes, which is roughly 10 times faster than with conventional laboratory techniques [60].

The CDB measurements were performed in high vacuum with the *in-situ* annealing

realized by means of a heater bulb positioned underneath the sample holder. For succeeding dilatometric measurements the temperature was logged by a pyrometer focused on a spot of graphite deposited on the sample. The sample holder was kept on $-20\,\mathrm{kV}$ potential, sample heating by the accelerated positrons can be neglected. Each spectrum of 10^6 counts could be accumulated within $60\,\mathrm{s}$ by means of high-purity Ge detectors with an energy resolution of $\Delta E = 1.35\,\mathrm{keV}$ (at $511\,\mathrm{keV}$).

From the Doppler broadening spectra the so-called S-parameter (shape-parameter) was numerically deduced, an integral line parameter characterizing the central part of the Doppler-broadened positron-annihilation line at $511\,\mathrm{keV}$. The energy range for the calculation amounts to 6.8×10^{-3} of $511\,\mathrm{keV}$. Since the broadening of the annihilation line is mainly due to the momentum of the annihilating electron, the S-parameter specifies the annihilation with low momentum valence electrons. Hence, the S-parameter is increased in material exhibiting a high amount of free volume. Exemplarily Fig. 3.11 shows the Doppler broadening of the annihilation line for HPT-Fe in the as-deformed state as well as after annealing at $800\,\mathrm{K}$.

3.3.3 Sample preparation

For the PALS measurements in sandwich geometry (see above) two identical samples with a mass per unit area of at least $150\,\mathrm{mg/cm^2}$ is necessary to ensure the annihilation inside the samples. Furthermore attention was paid to a minimum sample area of $7 \times 7\,\mathrm{mm^2}$ for covering the positron source completely. The sample surface was ground and polished manually.

The CDB samples had similar dimensions of ca. $7 \times 7 \times 1\,\mathrm{mm^3}$. Since the penetration depth of the slow positrons is much less, more attention was paid to the surface treatment. Thus, in addition to automated grinding and polishing, the CDB samples were electropolished to avoid preparation induced surface artefacts.

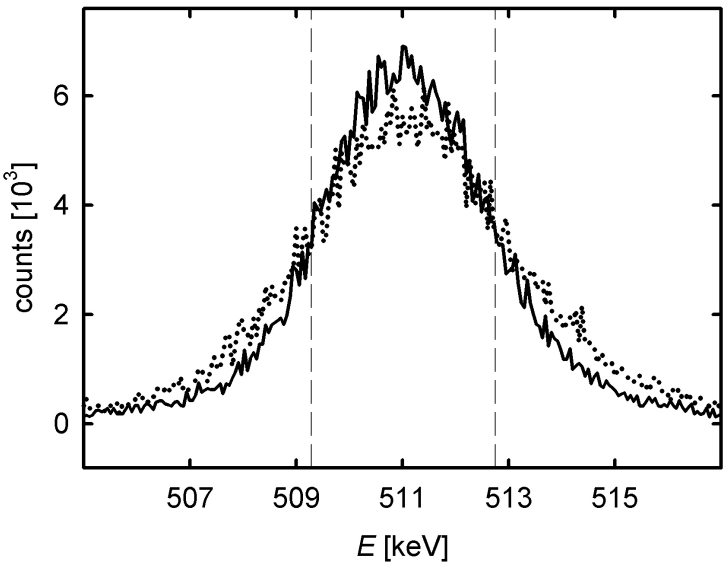

Figure 3.11: Doppler broadening of the e^+e^--annihilation line of HPT-Fe as-deformed (—) and after annealing at 800 K ($\cdots$). A higher number of counts for the as-deformed sample in the central part of the peak is clearly visible. The energy range for calculation of the S-parameter is indicated by (- - -).

3.4 SEM and microhardness

The scanning electron microscope (SEM) studies were performed at the Erich-Schmid Institute of Materials Science, Austrian Academy of Sciences at Leoben. The electron microscope used for the grain size analysis was a LEO 1525 field emission SEM (nominal resolution: $1.5\,\mathrm{nm}$ at $20\,\mathrm{kV}$), equipped with a back scattering detector. For the definition of the viewing direction within the HPT disc, see Fig. 3.7.

It is a well-known problem to determine crystallite sizes from cross-sectional views [61]. In this work, for the analysis of the SEM images, the grain boundaries (GB) were traced on transparent foils, digitalized and analyzed by means of the program "ImageJ" [62]. In doing so the area A of each grain was determined (grain area method). These grain size data were used for statistical analysis by means of histograms. Assuming spherical grains, the grain diameters d of all grains were calculated by $\sqrt{4A/\pi}$ taking properly into account the grains at the edges and corners of the micrograph (cf. [63]). The mean grain size d_m is given by the arithmetic mean value of the diameter-histogram. In contrast to area-averaged or area-weighted grain data, which is more robust with respect to very small grains [64], the diameter-averaged grain data is better comparable to that determined with the line intercept method (see next).

In those micrographs which showed a strong shape anisotropy of the crystallites, the line intercept method was applied to determine the mean grain shapes. In doing so several parallel lines with the total length L in the preferential direction a were drawn counting the number of intersections n with the grain boundaries. The mean grain intercept in the preferential direction is then given by $d_a = L/n$. The same was done in the perpendicular direction b to determine the grain aspect ratio d_a/d_b as well.

The microhardness measurements were performed by means of a Vickers hardness tester. In this process a pyramidal diamond tip is indented with a certain force into the

polished surface of the material to be measured. The microhardness number in [HV] can then be calculated by the force in [kp] divided by the indentation area in [mm^2]. Usually in the unit also the force in kp is specified, i.e. [HV1] means an applied force of $1\,kp$. All measurements in this work were performed with a force of $1\,kp$ ($9.81\,N$). The calculation of the microhardness number was done automatically by means of an optical microscope and the computer program "Buehler Omnimet".

4 Experimental Results

Body-centered cubic Metals

4.1 Iron

Regarding materials with a body-centered cubic (bcc) crystal structure the main focus of investigation in this work is on iron. Two degrees of purity were analyzed: ARMCO™ low-purity iron with a purity of 99.8 % and high-purity iron with 99.98 %. Tab. 4.1 shows the detailed chemical analysis of which carbon leaps out with a concentration difference of almost one order of magnitude. Carbon impurites in iron play a crucial role regarding deformation and structural refinement behaviour as well as defect stabilization [65].

Four different samples of ARMCO-Fe with 1, 5, 8 and 10 HPT revolutions were analyzed. Those with 1 and 10 revolutions were deformed at room temperature with a hydrostatic pressure of 2.2 GPa and were primarily used for positron annihilation mea-

Table 4.1: Chemical analysis of iron. The values for ARMCO-Fe were taken from [47]. The high-purity Fe was analyzed by the manufacturer (ChemPur GmbH). Elements with concentrations less than 3 ppm are omitted for high-purity Fe.

Sample	Elements and concentration [weight ppm]										
Armco-Fe	C	Cr	Cu	Mn	Ni	P	S	Si			
	70	200	200	800	300	80	110	70			
High-purity Fe	Al	B	C	Co	Cr	Ni	O	P	S	Si	Ta
	14	3	9	42	5	25	37	5	5	23	10

surements. The samples with 5 and 8 revolutions, which were available already, were used for dilatometry and scanning electron microscopy (SEM) imaging. All ARMCO-Fe disks had a diameter of $30\,\mathrm{mm}$ and a height of $7 - 8\,\mathrm{mm}$.

4.1.1 Annealing behaviour and microstructure

For a first characterization of the state after severe plastic deformation, microhardness measurements on polished cross sections of the HPT-disk were performed (Fig. 4.1). For the undeformed samples a mean value of the microhardness of $74\,\mathrm{HV1}$ is obtained. This value increases up to $400\,\mathrm{HV1}$ after deformation. Unsurprisingly, ARMCO-Fe with 1 revolution shows the largest gradient in microhardness over the radius. The relatively low hardness of the sample with 8 revolutions is maybe due to a different HPT-routine.

According to literature the saturation deformation of ARMCO-Fe is reached at an equivalent strain of $\varepsilon_{\mathrm{eq}} = 23$ [66]. This value can be considered as the limit for further structural refinement and defect densification.

For the investigation of the microstructure, scanning electron microscopy (SEM) imag-

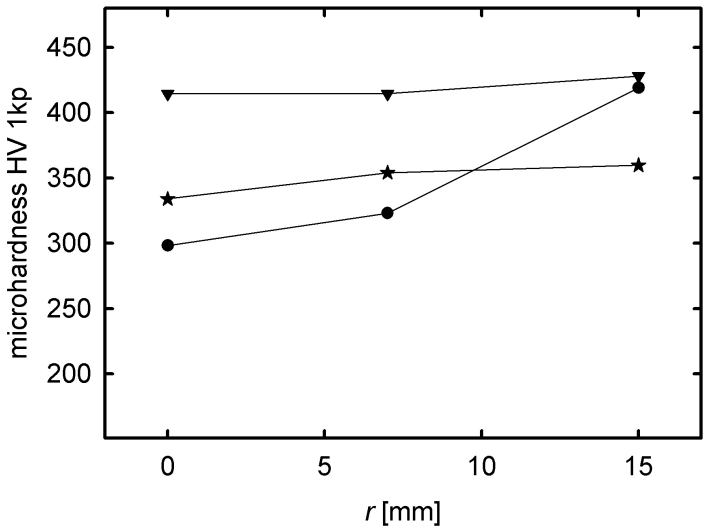

Figure 4.1: Microhardness measurements of ARMCO-Fe with 1 (–●–), 5 (–▼–) and 8 revolutions (–★–) as a function of the radial position (radius r) in the HPT-disk.

ing was performed. For this purpose three samples with different annealing states were prepared, namely in the as received-state (AR) and after linear heating with 3 K/min up to 673 K as well as up to 753 K, which are the same temperature profiles as in the dilatometric measurements (Fig. 4.4). The micrographs shown in Fig. 4.2 reveal a fine lamellar grain structure in the as received-state, which undergoes coarsening in the two following stages losing the lamellar structure entirely.

As described in Sec. 3.4 the SEM images were analysed with repect to grain size and grain size distribution. The results are shown in the histograms in Fig. 4.3. All three samples are showing a unimodal logarithmic Gaussian type distribution. The mean grain sizes are 144 nm in the AR state, 214 nm for annealing up to 673 K and 406 nm for 753 K. The last value may not be considered as statistically reliable due to the limited number of grains used for analysis.

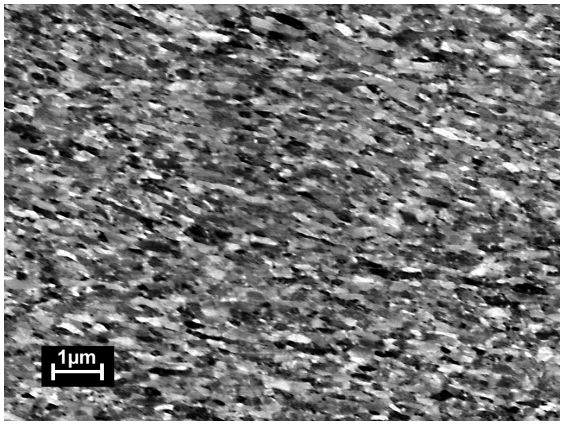

(a) Armco-Fe AR

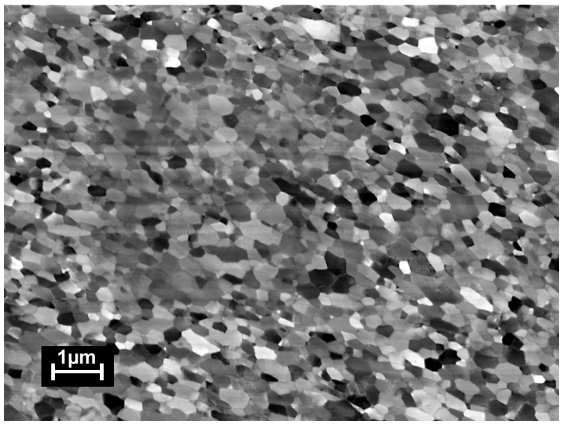

(b) Armco-Fe 673 K

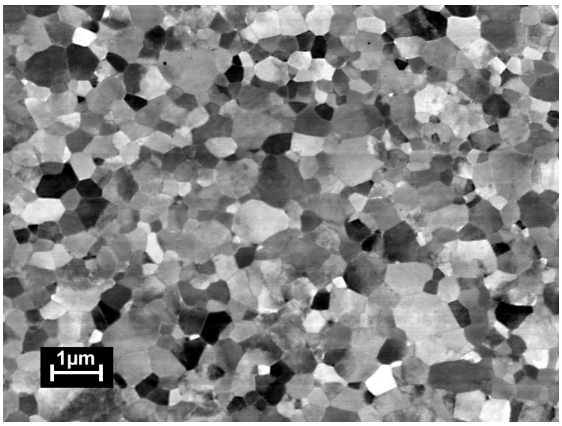

(c) Armco-Fe 753 K

Figure 4.2: Scanning electron micrographs in axial direction of Armco-Fe with 8 revolutions at different annealing steps. Magnification: 10 000.

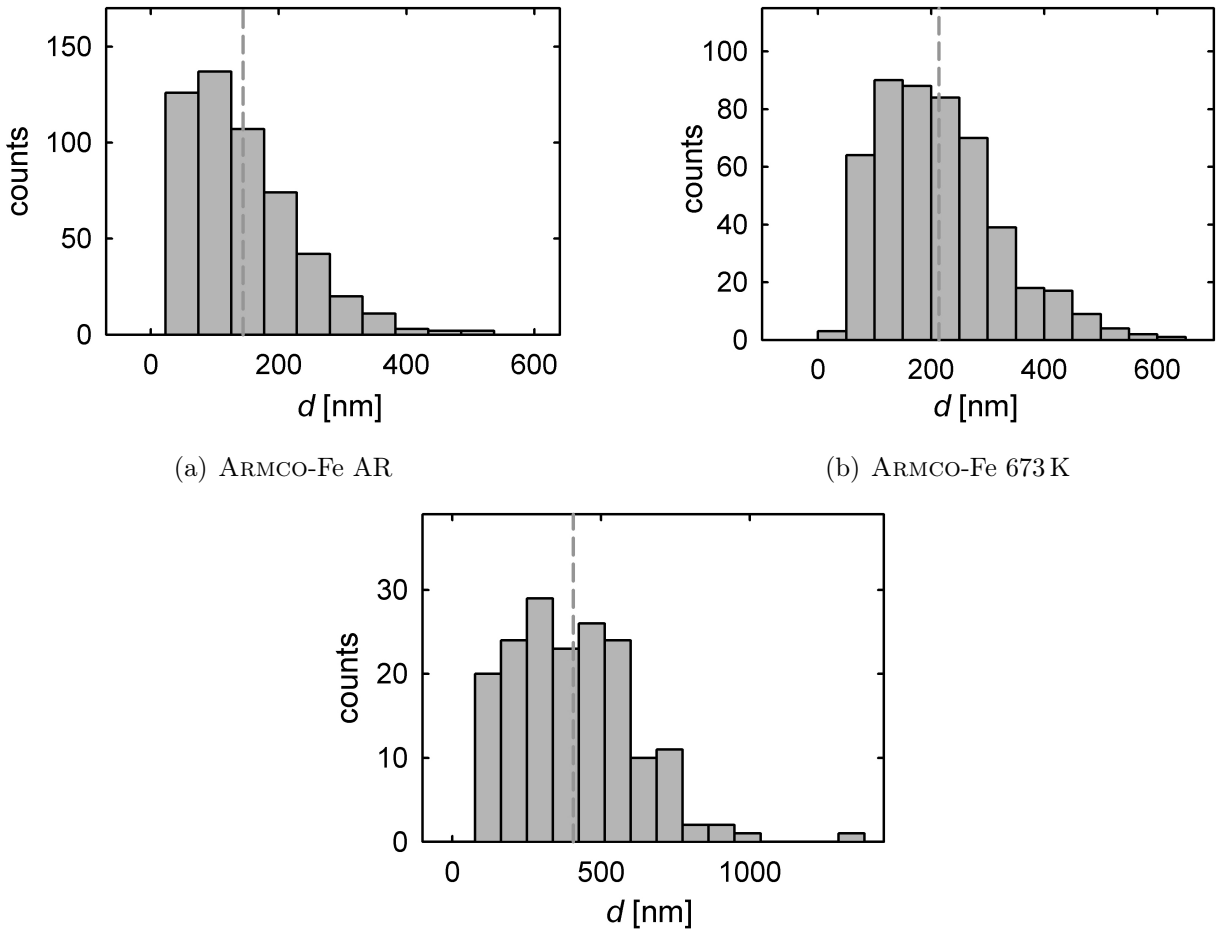

(a) Armco-Fe AR

(b) Armco-Fe 673 K

(c) Armco-Fe 753 K

Figure 4.3: Histograms of the grain size distribution of Armco-Fe with 8 revolutions at different annealing steps as determined from SEM micrographs (Fig. 4.2). The mean grain size diameter is indicated by (- - -).

Fig. 4.4 shows a dilatometric difference curve of a ARMCO-Fe iron sample in axial direction upon linear heating with $3\,\mathrm{K/min}$ up to $673\,\mathrm{K}$. From around $400\,\mathrm{K}$ up to ca. $700\,\mathrm{K}$ a total relative length shrinkage of nearly 6×10^{-4} can be observed. The difference curve is sigmoidal without any substructures. The temperature derivative exhibits one very pronounced minimum peak at about $500\,\mathrm{K}$. These characteristics of recovery in one single stage within a broad temperature range is typical of HPT-Fe samples in axial direction.

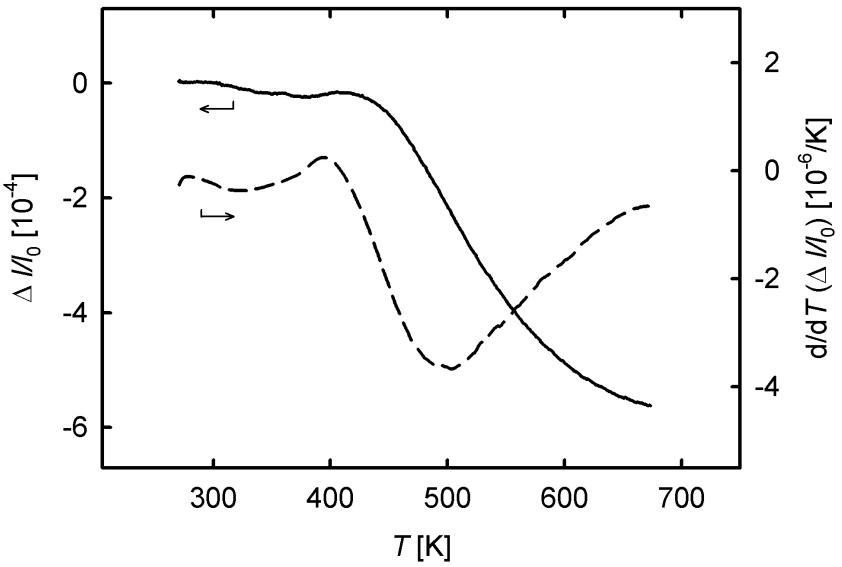

Figure 4.4: Dilatometric difference curve (—) of ARMCO-Fe in axial direction upon linear heating with $3\,\mathrm{K/min}$ up to $673\,\mathrm{K}$ and the derivative after smoothing (- - -) showing one pronounced minimum peak at $500\,\mathrm{K}$.

$\Delta\ell/\ell_{0,\,\mathrm{total}}$ of all dilatometric measurements performed on ARMCO-Fe is shown in Tab. 4.2. There is no systematic dependence of the degree of deformation. For instance, the lowest state of deformation of one revolution shows a medium relative length change of $9 - 10 \times 10^{-4}$. The highest $\Delta\ell/\ell_{0,\,\mathrm{total}}$ of 13.2 was measured with ARMCO-Fe 5r at $6\,\mathrm{K/min}$, a sample, whose equivalent strain $\varepsilon_{\mathrm{eq}}$ is below the saturation deformation of $\varepsilon_{\mathrm{eq}} = 23$. Measurements with a systematic variation with the heating rate were obtained for ARMCO-Fe 8r at $1.5 - 6\,\mathrm{K/min}$ and 5r at $0.75 - 3\,\mathrm{K/min}$. These data were

Table 4.2: Dilatometric measurements on ARMCO-Fe in axial direction. Heating rate δ (in [K/min]), equivalent strain ε, according to Eq. 3.1 and 3.2, and total relative length change $\Delta\ell/\ell_{0,\mathrm{tot}}$ (in $[10^{-4}]$) of all measurements performed on ARMCO-Fe with 8, 5 and 1 HPT revolutions (r). For the error analysis see Sec. 3.2.1. The maximum temperature was 673 K with the exception of the 6 K/min measurements, for which the maximum temperature was 753 K.

ARMCO-Fe 8r			**ARMCO-Fe 5r**			**ARMCO-Fe 1r**		
δ	ε	$\Delta\ell/\ell_{0,\mathrm{tot}}$	δ	ε	$\Delta\ell/\ell_{0,\mathrm{tot}}$	δ	ε	$\Delta\ell/\ell_{0,\mathrm{tot}}$
0.75	31	-10.2	0.75	17	-9.0	3.00	5	-9.7
1.50	38	-5.6	1.50	35	-8.6	6.00	7	-9.4
3.00	47	-5.4	3.00	29	-8.6			
6.00	27	-6.2	6.00	24	-11.8			
			6.00	20	-13.2			

used for a detailed analysis of the recrystallization kinetics (Sec. 4.1.3).

The mean values of the total relative length changes taken at 673 K are $\Delta\ell/\ell_{0,\,\mathrm{total,mean}} = -6.7 \times 10^{-4}$ for 8r, -10.1×10^{-4} for 5r and -9.6×10^{-4} for 1r. The lower value of the relative length change of ARMCO-Fe 8r is supported by the lower microhardness in this sample (Fig. 4.1). As explained in Sec. 4.1.4 and 4.3.2 in more detail, the total relative length change has to be entirely attributed to the annealing of open-volume structural defects. Hence $\Delta\ell/\ell_{0,\,\mathrm{total,mean}}$ can be used to calculate the total average release of free volume by using Eq. 3.4 yielding a value of

$$\left.\frac{\Delta V}{V_0}\right|_{\mathrm{total}} = -(2-3)\cdot 10^{-3}\,, \tag{4.1}$$

for all ARMCO-Fe samples, assuming isotropic defect annealing. As will be discussed more detailed in Chap. 5, this amount of atomic free volume can not exclusively be

attributed to the removal of dislocations and relaxed grain boundaries but also indicates the annealing of vacancy-type defects and the relaxation of non-equilibrium grain boundaries.

Positron annihilation

For further analysis of the microstructure of HPT-Fe also positron annihilation spectroscopy was performed, namely positron lifetime measurements[1] with the standard laboratory equipment using ^{22}Na and Doppler broadening S-parameter measurements with both, a high-intensity positron beam and the standard technique.

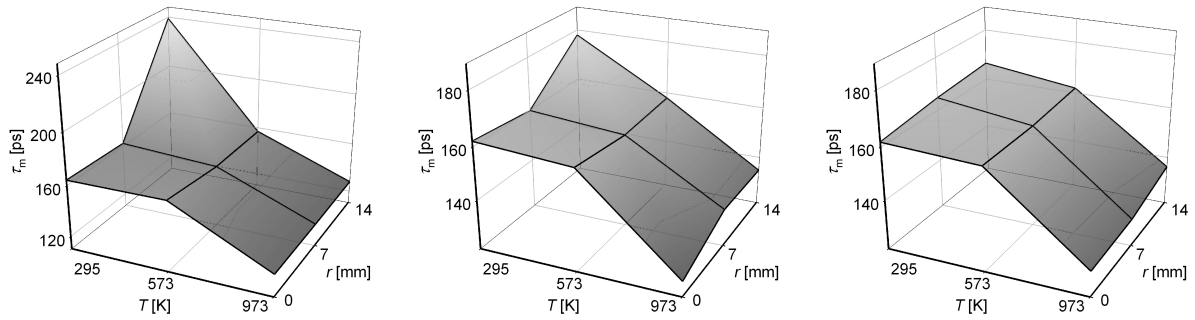

(a) ARMCO-Fe 1r (b) ARMCO-Fe 5r (c) ARMCO-Fe 8r

Figure 4.5: Mean positron lifetime τ_m of ARMCO-Fe with a) 1, b) 5 and c) 8 revolutions as a function of the annealing temperature T and the radial position (radius r) in the HPT-disk.

Fig. 4.5 shows the mean positron lifetime τ_m of ARMCO-Fe with 1, 5 and 8 revolutions measured by means of the standard laboratory technique. Each sample was measured

[1] The positron lifetime measurements and evaluations on HPT-Fe were done by Univ.-Prof. Dr. Werner Puff, Graz University of Technology.

at radial positions of 0, 7 and 14 mm in the as-received state as well as after annealing at 573 and 973 K for 1h. The highest e^+-lifetimes of $\tau_m = 239$ and 178 ps could be observed for the samples 1r and 5r at $r = 14$ mm prior to annealing. Towards the centre of the HPT-disk a reduced value of ca. 162 ps occurs. This indicates positron trapping at dislocations in the centre of the disk taking into account literature data of e^+-lifetimes of 167 ps at dislocations [67] and of 175 ps at single vacancies [68]. The higher lifetimes at $r = 14$ mm are probably due to trapping at vacancy agglomerates. It is worth mentioning that the highest lifetime of 239 ps is observed in the sample with the shortest time spent between preparation and measurement. The 8r sample at room temperature only shows a small decrease alongside the radius starting from a lower value of 167 ps. At 573 K all samples reveal a lifetime of ca. 160 ps as characteristic of e^+-trapping at dislocations. After annealing at 973 K for 1 hour a mean e^+ lifetime of about 130 ps in all samples throughout the radius could be detected. The literature values for the e^+ free lifetime in the bulk are ranging from $\tau_f = 110$ ps [65] up to 117 ps [67], so at this annealing temperature still some structural defects as e^+-trapping sites seem to be present. It can be pointed out, that the HPT-Fe 8r sample at room temperature showed the lowest variation of both e^+ lifetime and microhardness at relatively low values (cf. Fig. 4.1).

For a more detailed analysis of the defect annealing characteristic of HPT metals an *in-situ* measurement by means of a high-intensity positron beam is required. For this purpose measurements were done at the NEPOMUC facility at the FRM II in Garching (see Sec. 3.3.2). The high number of moderated positrons enables studies of the fast defect annealing and offers to combine the results with dilatometric studies of the annealing of free volume which are on the same time scale.

Fig. 4.6 shows the Doppler broadening S-parameter curve of ARMCO-Fe AR. The decreasing S-parameter upon heating suggests an annealing of structural defects up to recrystallization in a manner of one broad stage very similar to that of the relative length change observed with dilatometry (Fig. 4.4). Afterwards the measurement was

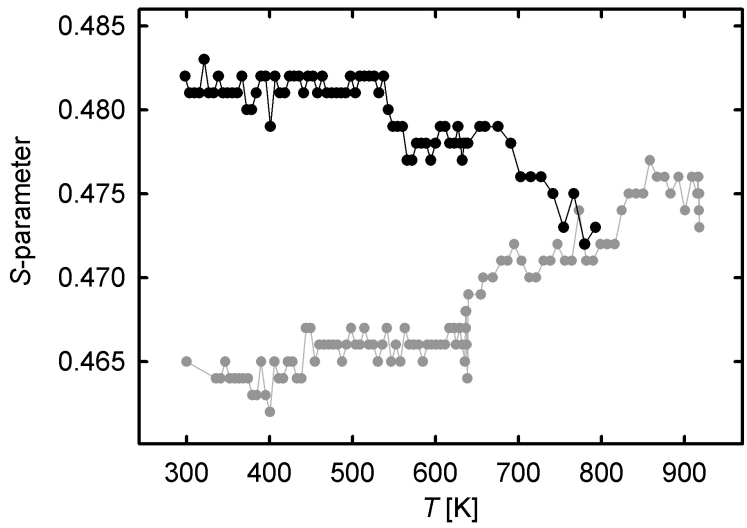

Figure 4.6: Doppler broadening S-parameter curve of ARMCO-Fe AR (–●–) measured in-situ upon heating with ca. 5 K/min. A second run after annealing at 800 K serves as reference curve (–●–).

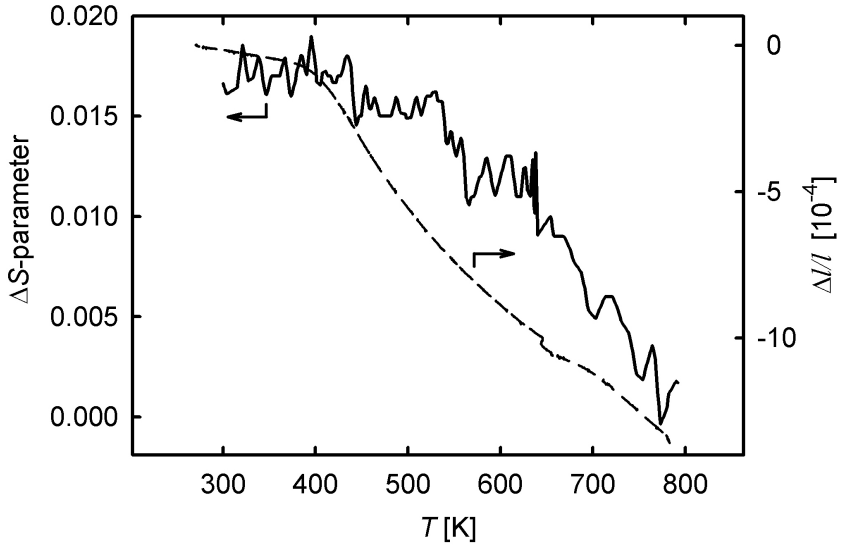

Figure 4.7: Doppler broadening ΔS-parameter curve (—) and dilatometric difference curve (- - -) of ARMCO-Fe upon heating with ca. 5 K/min.

immediately repeated to obtain a pseudo-reference curve which shows the increase of the S-parameter with the temperature exclusively due to the thermal expansion of the lattice. The characteristics of the reference measurement were analogously observed for the W-parameter of Fe in literature [69] (page 51).

Fig. 4.7 shows the interpolated difference curve of the two subsequent measuring runs in Fig. 4.6. The recording of the used temperature profile (quasi-linear heating with ca. $5\,\mathrm{K/min}$) allowed a dilatometric measurement with the same $T(t)$ profile on a sample of the same HPT disk. The resulting relative length change curve (dashed line, right ordinate) shows a continuous shrinkage from ca. $400\,\mathrm{K}$ up to the maximum temperature of $773\,\mathrm{K}$[2]. The annealing characteristics observed by the two complementary techniques of e^+ annihilation and dilatometry fit together very well. However, a considerable shift of the ΔS-parameter to higher temperatures is clearly observable. This shift is even much more pronounced at the recrystallization stage of fcc metals and can be explained with the saturation trapping of e^+ at defects for small crystallite sizes (see Sec. 4.3.1, 4.4.1 and Chap. 5).

4.1.2 Influence of sample purity

For investigation of the influence of impurities on the annealing behaviour of HPT-Fe also high-purity iron samples were prepared and analyzed[3]. The dilatometric measurements (Fig. 4.8) reveal generally similar annealing characteristics for samples prepared in axial direction, however the defect annealing in high-purity Fe starts about

[2] The little notch at ca. $650\,\mathrm{K}$ is a result of a discontinuity in the temperature profile $T(t)$ due to a repositioning of the heater bulb during the S-parameter measurement. Whereas this discontinuity had apparently no effect on the S-parameter, it caused this measurement artefact in the relative length change curve.

[3] The preparation, dilatometric measurements, evaluations and discussions on high-purity Fe were done by Boris R. Scherwitzl within the framework of his master thesis under my co-supervision [52].

80 K earlier and reaches its maximum already at 400 K which is about 100 K less than in ARMCO-Fe.

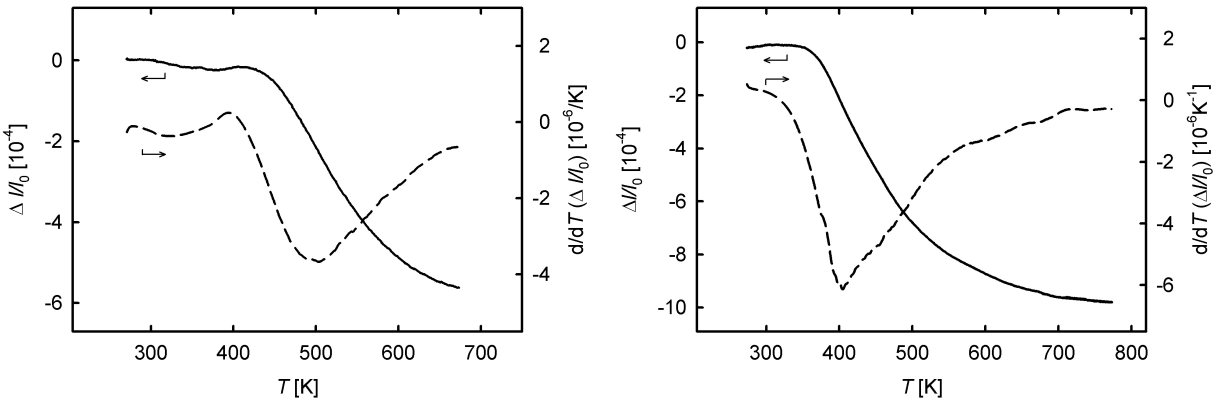

(a) ARMCO-Fe (b) High-purity Fe

Figure 4.8: Dilatometric difference curves (—) of a) ARMCO-Fe (identical to Fig. 4.4) and b) high-purity Fe in axial direction upon linear heating with 3 K/min up to 673 K and 773 K, respectively. For the derivative curves after smoothing (- - -) the shift of the minimum with the purity can clearly be discerned.

This behaviour can obviously be explained with the different sample purity in the order of one magnitude. Especially the carbon impurities are known for playing a crucial role for defect stabilization and recrystallization [65].

Also the different values for the total relative length change are remarkable (Fig. 4.8). This fact is all the more interesting if one considers the larger grain size in the as-deformed state (see Fig. 4.9 a)) and, as a consequence of that, the lower contribution of grain boundaries to the free volume in the case of high-purity Fe. The higher total relative length change of nearly 10×10^{-4} in the case of HP-Fe is due to the fact that the overall annealing of defects is shifted to lower temperatures and the maximum annealing temperature applied has even been 100 K higher. As the e^+ annihilation measure-

ments at the e^+ beam (Fig. 4.7) have shown, there is defect annealing up to 773 K also in the case of ARMCO-Fe. Hence, the annealing of structural defects in Fig. 4.8 a) is not finished at the maximum temperature of 673 K applied in dilatometry for ARMCO-Fe.

Table 4.3: Dilatometric measurements on high-purity (HP) Fe as well as on ARMCO-Fe in tangential direction (other values for ARMCO-Fe see Tab. 4.2). Heating rate δ (in [K/min]), equivalent strain ε, according to Eq. 3.1 and 3.2, total relative length change $\Delta\ell/\ell_{0,\mathrm{tot}}$ (in $[10^{-4}]$). For HP-Fe in tangential direction also the relative elongation $\Delta\ell/\ell_{0,+}$ is given (see Sec. 4.1.4). For the error analysis see Sec. 3.2.1. The maximum temperature in each run was 773 K.

High-purity Fe axial			**High-purity Fe tangential**			
δ	ε	$\Delta\ell/\ell_{0,\mathrm{tot}}$	δ	ε	$\Delta\ell/\ell_{0,\mathrm{tot}}$	$\Delta\ell/\ell_{0,+}$
0.75	22	-10.5	0.75	24	-2.5	1.6
1.50	30	-8.6	1.50	24	2.6	4.0
1.50	22	-10.8	3.00	19	2.6	3.0
3.00	30	-9.8	6.00	34	2.4	3.1
3.00	22	-10.6				
6.00	40	-10.2				
6.00	22	-10.3				
High-purity Fe radial			**ARMCO-Fe tangential**			
δ	ε	$\Delta\ell/\ell_{0,\mathrm{tot}}$	δ	ε	$\Delta\ell/\ell_{0,\mathrm{tot}}$	$\Delta\ell/\ell_{0,+}$
6.00	31	-4.5	6.00	n.a.	-6.9	-0.6

Tab. 4.3 shows the results of all dilatometric measurements performed on high-purity Fe. Samples in all three orthogonal directions of the HPT-deformed disc (see scheme Fig. 3.8) were prepared. All axial as well as the radial samples showed an overall

length shrinkage similar to those at the axial ARMCO-Fe samples (Tab. 4.2). However, the tangential samples showed a far more complex behaviour with at first an elongation $\Delta\ell/\ell_{0,+}$ and a following slightly smaller length shrinkage (Sec. 4.1.4). The total relative length $\Delta\ell/\ell_{0,\mathrm{tot}}$ change in the tangential HP-Fe samples is positive except for the lowest heating rate.

For the axial direction of HP-Fe a mean value $\Delta\ell/\ell_{0,\,\mathrm{total,mean}}$ of the relative length change of $(-10.1\pm0.7)\cdot10^{-4}$ is obtained. Like in Sec. 4.1.1 $\Delta\ell/\ell_0$ can be used to calculate the total release of free volume (Eq. 3.4):

$$\left.\frac{\Delta V}{V_0}\right|_{\mathrm{total}} = -3.03 \times 10^{-3}\ . \tag{4.2}$$

Fig. 4.9 shows SEM images of high-purity Fe in axial direction at annealing steps of AR, 508, 648, and $773\,\mathrm{K}$. These particular annealing steps were chosen on the basis of the special results of the length change measurements in tangential direction (see Sec. 4.1.4). A continuous grain growth beginning from a) $320\,\mathrm{nm}$ in the AR state over b) $480\,\mathrm{nm}$ and c) $1010\,\mathrm{nm}$ up to d) $4900\,\mathrm{nm}$ at $773\,\mathrm{K}$ can be observed. These mean values were determined following the procedure described in Sec. 3.4. The grain size histograms of high-purity Fe [52] have a very similar shape like those of ARMCO-Fe (Fig. 4.3).

However, there are substantial differences in the initial grain size and also the grain shapes between the high and low purity samples. While the grains of ARMCO-Fe exhibit a strong lamellar shape, those of HP-Fe are virtual spherical. The larger grain size of HP-Fe can be explained with a dynamic recrystallization during the HPT deformation procedure (see Chap. 5).

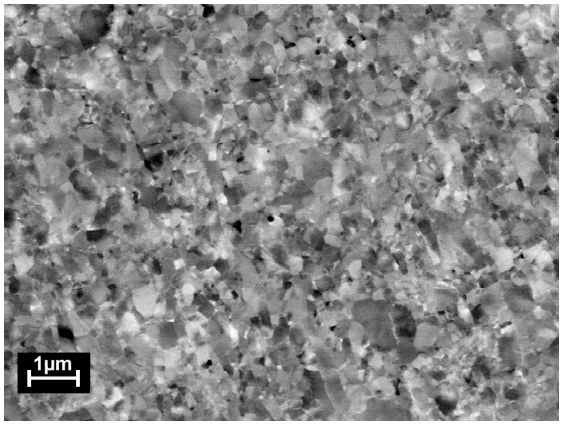

(a) High-purity Fe AR

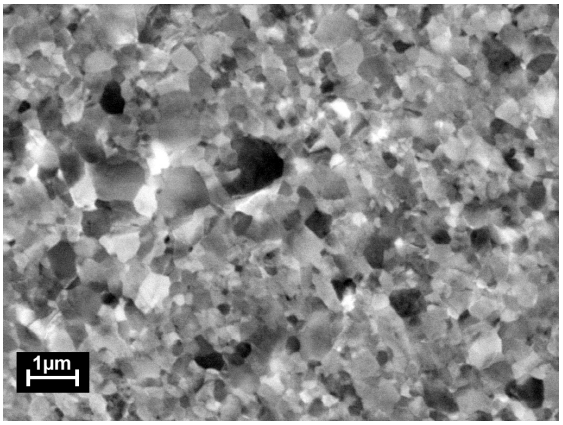

(b) High-purity Fe 508 K

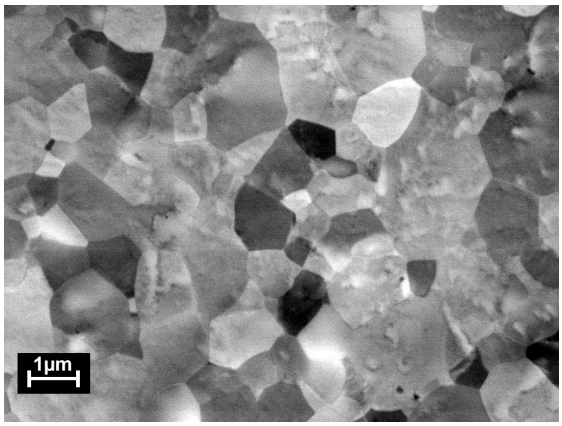

(c) High-purity Fe 648 K

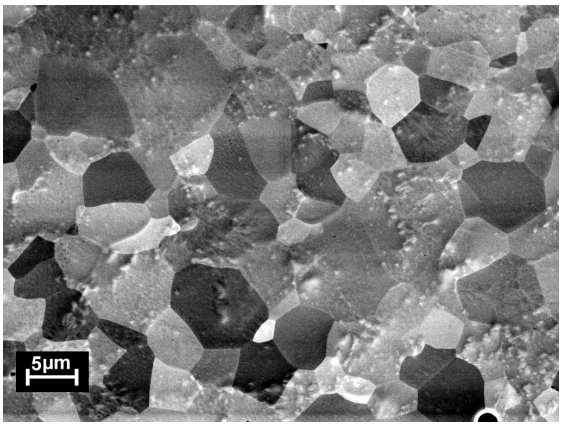

(d) High-purity Fe 773 K

Figure 4.9: Scanning electron micrographs of high-purity Fe with 10 revolutions at different annealing steps (cf. Sec. 4.1.1 and Fig. 4.2). Magnification: 10 000 in (a-c), 2 000 in (d).

4.1.3 Analysis of kinetics

For analysis of the annealing kinetics of HPT-Fe, dilatometry measurements were performed at different heating rates ranging from 0.75 up to 6 K/min. Fig. 4.10 exemplifies the resulting shift of the relative length change curves for ARMCO-Fe with 8 revolutions.

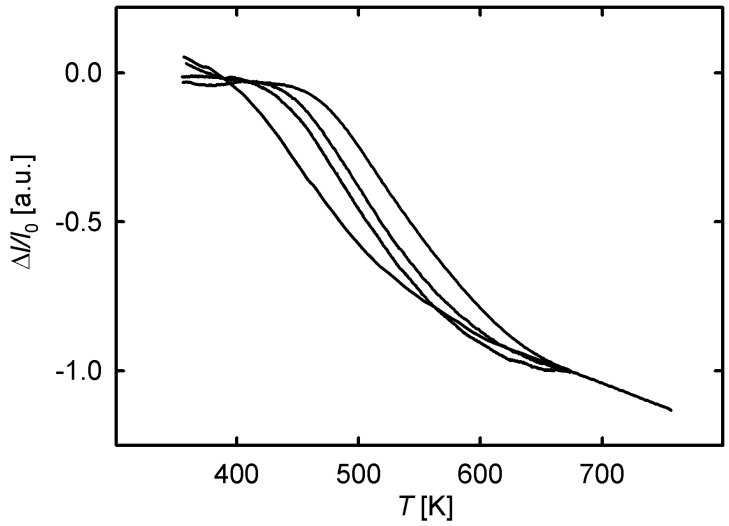

Figure 4.10: Relative length change $\Delta\ell/\ell_0$ of ARMCO-Fe 8r vs. the temperature T at different heating rates of (from left to right) 0.75, 1.5, 3 and 6 K/min (see also Tab. 4.2). For demonstrating the shift with temperature, the length change curves have been normalised yielding $\Delta\ell/\ell_0 = -1$ at 673 K for each sample.

The minima T_p of the temperature derivatives (see e.g. Fig. 4.4) correspond to the maxima of recrystallization transformation. Their shift can be analysed by means the method of Kissinger (see Sec. 3.2.4). The corresponding semilog plot for all ARMCO-Fe samples is shown in Fig. 4.11.

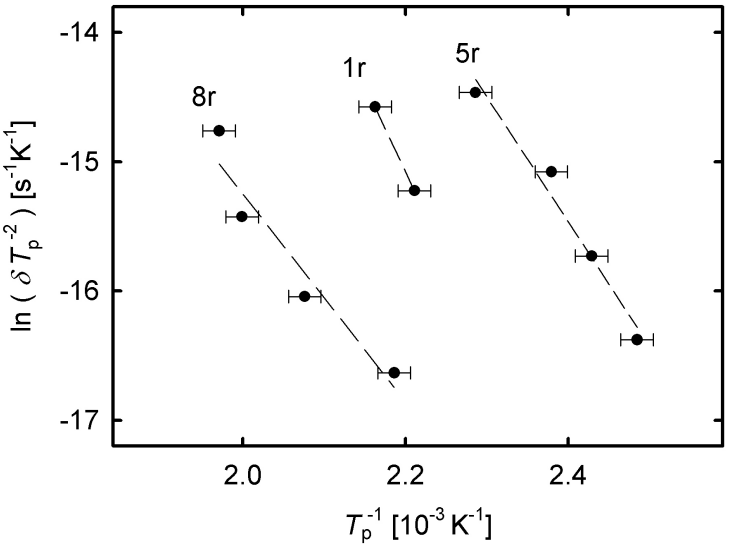

Figure 4.11: Kissinger plots (•) of HPT ARMCO-Fe samples with 1, 5 and 8 revolutions (1r, 5r, 8r) and the appropriate regression lines (- - -). The T_p are the minima of the temperature-derivative of the relative length change curve. The horizontal error bars characterize the uncertainty of the T_p-determination from the plot. The vertical ones are smaller than the symbol size.

The slopes of the regression lines can be used to calculate the activation energy Q of the recrystallization (Eq. 3.9). For ARMCO-Fe with 5r a value Q of 0.83 ± 0.03 eV and for 8r of 0.69 ± 0.05 eV is derived. The respective error is deduced from the regression analysis. For 1r a reliable Q-value cannot be given since only two data points are available. It is worthwhile to mention that the annealing in the case of Fe 8r takes place at general higher temperatures than at Fe 5r. The reason for this could be found in some unknown HPT-deformation parameters of these samples like deformation temperature or pressure.

The Kissinger analysis of HP-Fe [52] revealed an activation energy of 0.75 ± 0.02 eV, lying between the values for ARMCO-Fe with 5 and 8r. In literature a value for the activation energy of the recrystallization of HPT-Fe of $Q = 0.93 \pm 0.10$ eV is reported [70] (see discussion Chap. 5).

4.1.4 Orientation-dependent measurements

Like it was already anticipated in Tab. 4.3 the dilatometric measurements[4] were performed in three orthogonal directions defined with respect to the HPT deformation axis *axial*, *radial* and *tangential* (see Fig. 3.8). While there is no substantial difference in the annealing behaviour of the samples prepared in axial and radial direction (for radial measurements see [52]), the tangential samples delivered relative length changes of quite a different nature, i.e., an overall elongation was mostly observed.

In Fig. 4.12 relative length change measurements in axial and tangential direction upon annealing with $3\,\mathrm{K/min}$ are depicted. While the axial measurement shows a total relative length shrinkage, the tangential sample exhibits at first an elongation until a peak

[4] The preparation, dilatometric measurements, evaluations and discussions on high-purity Fe were done by Boris R. Scherwitzl within the framework of his master thesis under my co-supervision [52].

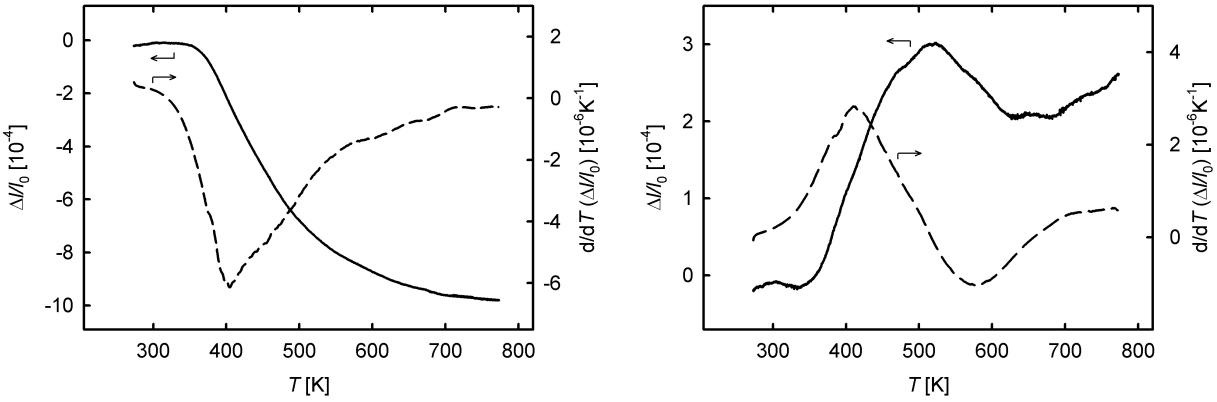

(a) High-purity Fe axial

(b) High-purity Fe tangential

Figure 4.12: Dilatometric difference curves (—) of high-purity Fe samples in a) axial and b) tangential direction upon linear heating with 3 K/min up to 773 K and their derivatives after smoothing (- - -).

at 508 K where a relative length shrinkage up to 648 K sets in. The subsequent minor re-elongation observed above 680 K is not characteristic for all tangential measurements.

To clarify the situation in the tangential samples, the temperatures at the elongation peak at 508 K and at the shrinkage minimum at 648 K of HP-Fe were taken as two further annealing steps for the SEM imaging (Fig. 4.9) beside the AR and the final state at 773 K. The spherical grains and the continuous grain growth in the course of these annealing steps do not provide an indication of anisotropies in the microstructure which could explain such an elongation.

A tentative explanation for the elongation in tangential direction could be macrostress. A preliminary analysis of HPT-deformed metals regarding macrostresses was performed for HPT-Ni by means of X-ray diffractometry (XRD). However, first results of these ongoing measurements yielded no indication for high compressive stresses neither in axial nor in tangential direction (see Sec. 4.3.2).

4.2 Tantalum

The second investigated metal with bcc crystal structure was tantalum[5]. The samples purity amounts to 99.9 %. The chemical analysis is given in Tab. 4.4. Tantalum was analyzed in more detail regarding the amount of deformation. Six small discs with a diameter of $d = 14$ mm and one large disc with $d = 30$ mm were HPT deformed with 1, 3 and 5 revolutions and with 10 revolutions, respectively. The small discs served for microhardness and positron lifetime measurements, the large one for dilatometry. All samples were also characterized by the scanning electron microscope.

Table 4.4: Chemical analysis of tantalum impurities according to specification of manufacturer (Plansee Holding AG). Elements with concentrations less than 20 ppm are omitted.

Sample	**Elements and concentration [weight ppm]**											
Ta	Al	C	Co	Fe	Mo	N	Nb	Ni	O	Si	Ti	W
	20	30	20	100	100	30	400	50	100	50	50	100

4.2.1 Annealing behaviour and microstructure

The evolution of the microstructure upon increasing deformation can be seen very well in Fig. 4.13 which shows SEM micrographs of HPT-Ta 1r at different radii of 0, 3 and 6 mm. The corresponding equivalent strain $\varepsilon_{\mathrm{eq}}$ (Eq. 3.1, 3.2) amounts to 0, 12 and 23. At the centre, which theoretically should be deformation-free, one can see a very in-

[5] The dilatometric measurements and evaluations on HPT-Ta were done by Anna Weitzer within the framework of her bachelor thesis under my co-supervision.

homogeneous distorted microstructure with pores of micrometer size. At a radius of 3 mm already small grains with isolated larger ones have formed. At 6 mm and an $\varepsilon_{\mathrm{eq}}$ of 23, a homogeneous microstructure with even smaller grains can be observed.

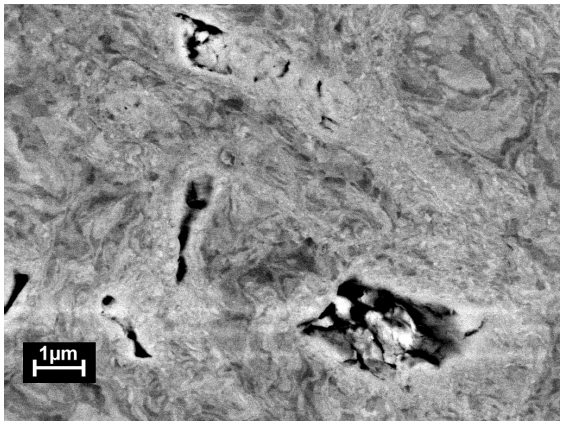

(a) HPT-Ta 1r, $r = 0\,\mathrm{mm}$

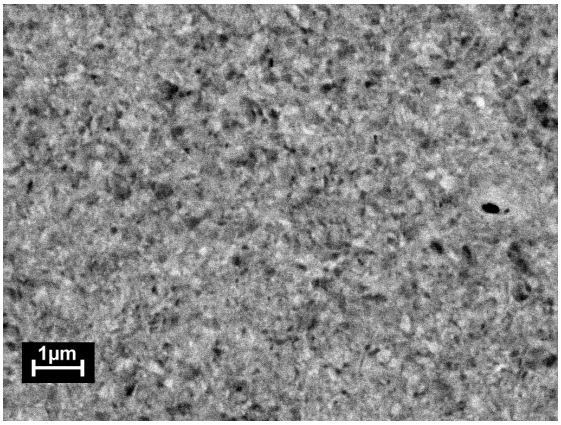

(b) HPT-Ta 1r, $r = 3\,\mathrm{mm}$

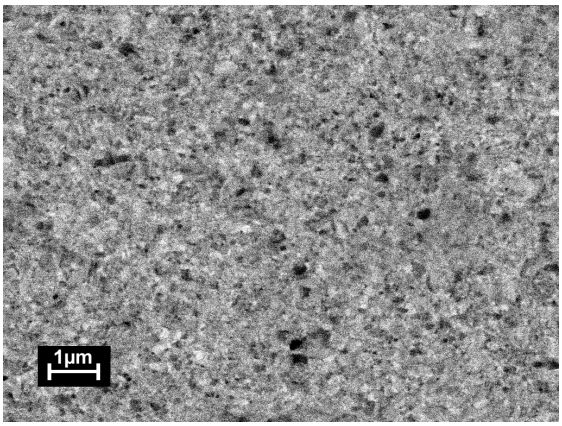

(c) HPT-Ta 1r, $r = 6\,\mathrm{mm}$

Figure 4.13: Scanning electron micrographs of HPT-Ta with 1 revolution at different radii. Magnification: 10 000.

This gradient of deformation can also be seen in the microhardness measurements depicted in Fig. 4.14. The microhardness of three of the small samples with a diameter

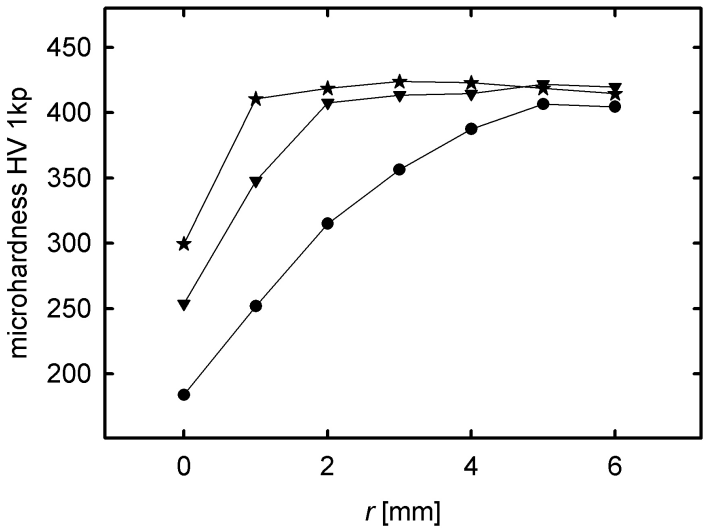

Figure 4.14: Microhardness measurements of HPT-Ta with 1 (–●–), 3 (–▼–) and 5 revolutions (–★–) as a function of the radial position (radius r) in the HPT-disk.

of $d = 14$ mm were tested alongside the radius in steps of 1 mm. The initial microhardness prior to deformation was 86 HV1. The hardness at the centre of the HPT disc increases by more than a factor of two after a deformation of one revolution already (cf. Fig. 4.13 a)). With increasing radius HV increases up to more than 400 at $r = 6$ mm. This increase of hardness with the radius occurs much faster in the case of 3r and 5r, where a maximum is reached at 2 and 1 mm, respectively. With these radii a saturation deformation of $\varepsilon_{\mathrm{eq}} = 18 \pm 5$ can roughly be estimated for which no further increase in microhardness and grain refinement can be expected.

During the HPT deformation of the small samples ($d = 14$ mm), the torsional moment of the anvils was logged (see Sec. 3.1) and plotted as a function of the equivalent strain calculated for a disc radius of 6 mm (Eq. 3.1, 3.2). Fig. 4.15 shows these plots for HPT-Ta 1r, 3r and 5r. All three curves increase very steeply. The torsional moment M attains a saturation value (ca. 660 Nm) at a deformation of $\varepsilon_{\mathrm{eq}} = 17 \pm 1$. This value is rather

similar to that deduced from microhardness measurements but can be considered as more precise compared to the latter one.

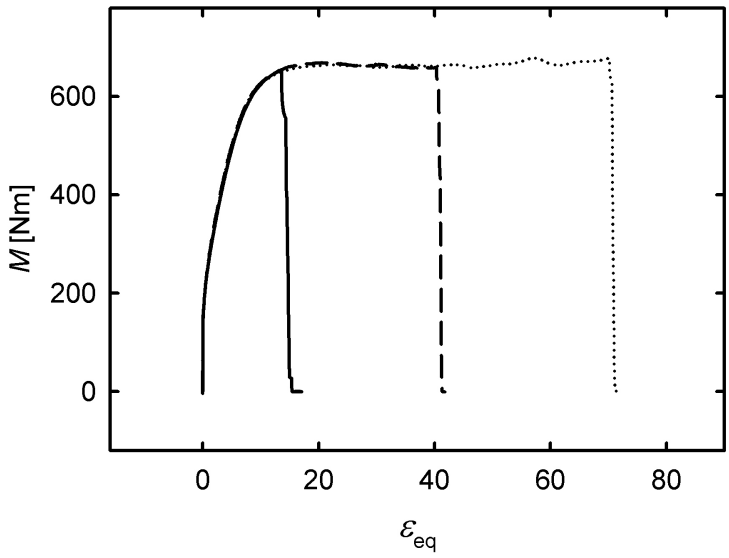

Figure 4.15: Torsional moment M of the anvils of the HPT facility during deformation of HPT-Ta (small samples) with 1 (—), 3 (- - -) and 5 ($\cdots$) HPT revolutions as a function of the equivalent strain ε_{eq} calculated for a radius of 6 mm. Saturation deformation is reached at $\varepsilon_{eq} \approx 17$.

Fig. 4.16 shows a dilatometric measurement of HPT-Ta 10r in axial direction upon linear heating with $1.5\,\mathrm{K/min}$ up to a maximum temperature of $773\,\mathrm{K}$. A relative length shrinkage in the temperature range from 400 to ca. $700\,\mathrm{K}$ with a total stroke of 3.2×10^{-4} can be observed. Like in the case of HPT-Fe (Fig. 4.4, 4.8) the annealing of free volume takes place in one broad stage. However, the Ta curve does not show a perfect sigmoidal shape and exhibits a quite constant slope in the range from 400 to around $520\,\mathrm{K}$ followed by a narrow and steeper sigmoidal-type annealing, as indicated by the minimum peak of the derivative curve in Fig. 4.16. This type of annealing behaviour could be observed for all measurements performed on Ta.

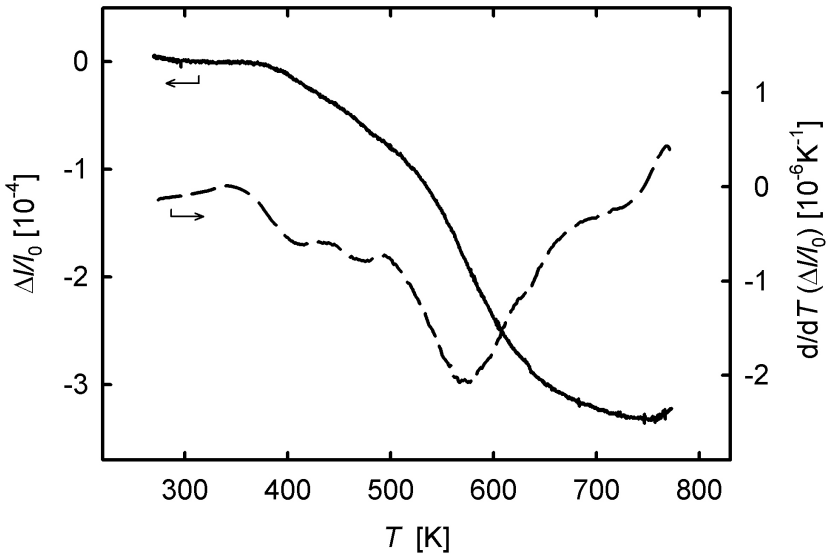

Figure 4.16: Dilatometric difference curve (—) of HPT-Ta upon linear heating with 1.5 K/min up to 773 K and the derivative after smoothing (- - -) showing a minimum peak at 570 K.

In Tab. 4.5 the values of the total relative length change $\Delta\ell/\ell_{0,\mathrm{tot}}$ of all dilatometric measurements performed on HPT-Ta are summarized. The samples were prepared from the disk at a constant radius of $14\,\mathrm{mm}$ in the saturation deformation zone. Due to the disk geometry only specimens in axial direction could be prepared. The different measurements showed only little variation of $\Delta\ell/\ell_{0,\mathrm{tot}}$ yielding a mean value of $(-3.0\pm 0.4)\times 10^{-4}$. Attributing this relative length change to the annealing of structural defects totally, the average released volume in HPT-Ta can be denoted to

$$\left.\frac{\Delta V}{V_0}\right|_{\mathrm{total}} = (-9.0 \pm 1.3)\times 10^{-4}\,, \tag{4.3}$$

according to (Eq. 3.4) assuming isotropic defect annealing. The contributions of the various types of structural defects to this total free volume are discussed in Chap. 5.

Table 4.5: Dilatometric measurements on HPT-Ta. Heating rate δ (in [K/min]), equivalent strain ε, according to Eq. 3.1 and 3.2 ($\Delta\varepsilon = 5$) and the total relative length change $\Delta\ell/\ell_{0,\mathrm{tot}}$ (in $[10^{-4}]$) of all measurements performed on HPT-Ta in axial direction. For the error analysis see Sec. 3.2.1. Maximum temperature in each run was 773 K.

HPT-Ta 10r		
δ	ε	$\Delta\ell/\ell_{0,\mathrm{tot}}$
0.75	70	-2.8
1.50	70	-3.2
3.00	70	-2.5
6.00	70	-3.5

Fig. 4.17 shows SEM micrographs of HPT-Ta 10r in the AR state and after the annealing at 773 K in the dilatometer. While d is – comparatively with other HPT materials – very small in the AR state ($d_{\mathrm{m}} \approx 50$ - 100 nm) the grains grow only a little up to $d_{\mathrm{m}} \approx 150$

- 200 nm. However, it has to be stated that the two SEM samples were prepared in different orientations, tangential and axial (see Sec. 3.2.3).

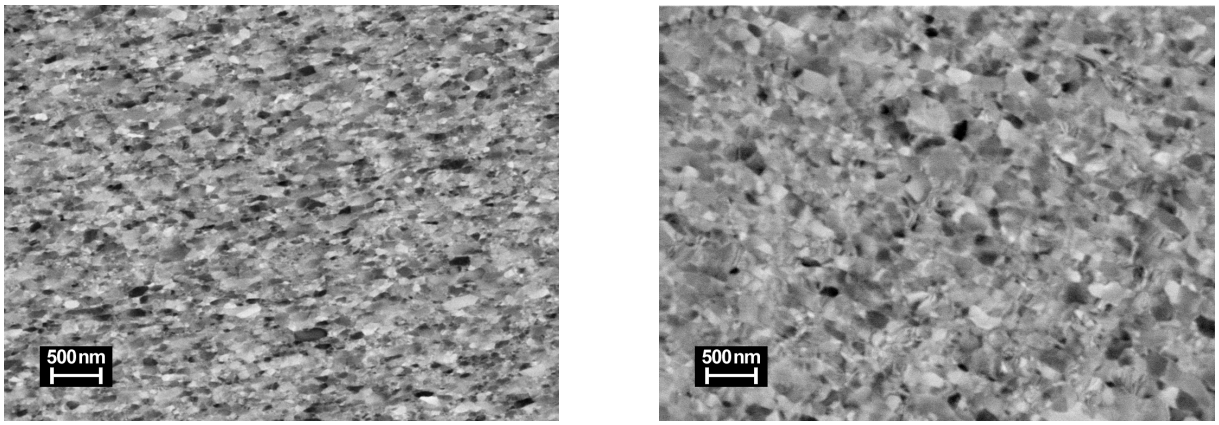

(a) HPT-Ta AR tangential (b) HPT-Ta 773 K axial

Figure 4.17: Scanning electron micrographs of HPT-Ta with 10 revolutions AR in tangential and annealed at 773 K in axial direction. (For definition of the viewing direction see Fig. 3.7.) The magnification is 20 000 in both micrographs.

Positron annihilation

HPT-Ta was also analyzed by means of Doppler broadening spectroscopy at the high-intensity e^+ beam of the FRM II (see Sec. 3.3.2). As described in Sec. 4.1.1 an interpolated ΔS-parameter curve was obtained (Fig. 4.18) reconstructing a pseudo-reference curve after the first measurement. Since no substantial change of the ΔS-parameter upon annealing up to 952 K can be observed, saturation e^+ trapping due to a very high defect concentration can be concluded even for the annealed state, where substantial length shrinkage has occured according to dilatometry (see superimposed $\Delta\ell/\ell_0$-curve in Fig. 4.18).

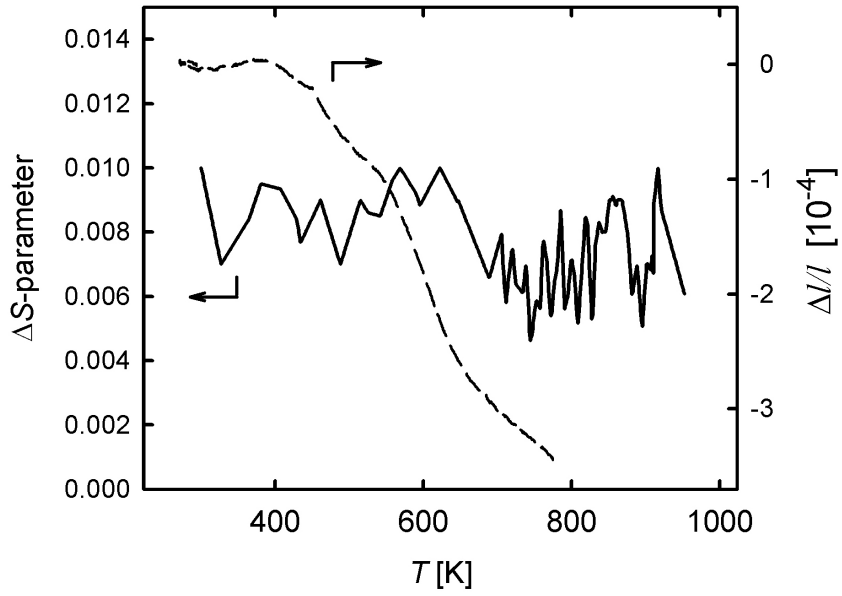

Figure 4.18: Doppler broadening ΔS-parameter curve of HPT-Ta (—) upon heating with ca. 5 K/min and dilatometric difference curve (- - -) with a heating rate of 6 K/min.

Beside the Doppler broadening measurements also the positron lifetime in the AR state has been determined: The small HPT-Ta samples ($d = 14\,\mathrm{mm}$) with 1, 3 and 5 revolutions were analyzed at the centre and at the border of the HPT disc. Since the spatial resolution of the e^+ lifetime spectroscopy in the standard laboratory is only $\approx 4\,\mathrm{mm}$, no substantial difference between the two radial positions could be detected. The degree of deformation has no appreciable effect on the e^+ lifetime as well. The mean e^+ lifetime value τ_m amounts to $193 \pm 2\,\mathrm{ps}$. According to literature data such a lifetime in Ta can be attributed to single vacancies [71, 72].

4.2.2 Analysis of kinetics

The dilatometric measurements presented in Tab. 4.5 were performed at different heating rates to study the annealing kinetics of HPT-Ta. The shift of the temperature T_p of

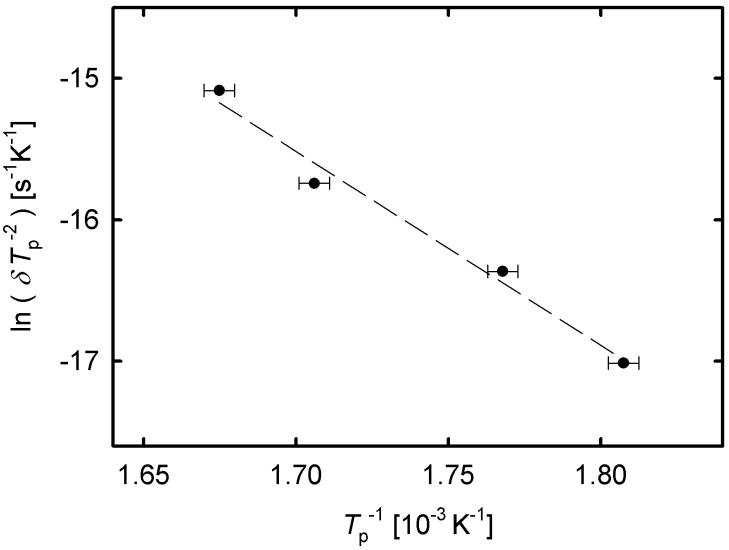

Figure 4.19: Kissinger plot (•) of HPT-Ta with 10 revolutions. The activation energy Q deduced from linear regression (- - -) amounts to 1.18 eV.

the minimum peak of the derivative curve (Fig. 4.16) was analyzed by the method of Kissinger (Sec. 3.2.4) yielding a semilog plot shown in Fig. 4.19.

From the regression analysis of the Kissinger plot an activation energy Q of 1.18 ± 0.02 eV for the annealing process can be deduced according to Eq. 3.9. The error of Q is taken from the regression analysis.

FACE-CENTERED CUBIC METALS

4.3 Nickel

The first investigated material with face-centered cubic crystal structure was Ni[6]. The sample purity was $99.99+\,\%$ (see Tab. 4.6). Two billets with a diameter of 30 and a height of $10\,\mathrm{mm}$ were prepared and deformed at room temperature with 5 HPT revolutions under a hydrostatic pressure of $2.2\,\mathrm{GPa}$. These two samples served for comprehensive studies ranging from dilatometric measurements, scanning electron microscopy (SEM) including electron backscattering diffractometry (EBSD), positron annihilation to X-ray diffractometry (XRD) for macro stress analysis.

4.3.1 Annealing behaviour and microstructure

For the dilatometric studies of HPT-Ni samples with an equivalent strain ranging from $\varepsilon_{\mathrm{eq}} = 12 - 30$ were prepared. According to literature [74], saturation deformation for Ni at this purity is reached for an HPT-induced equivalent strain of $\varepsilon_{\mathrm{eq}} \approx 10$. The microstructure size at this amount of plastic deformation is the smallest achievable and

[6] The preparation, dilatometric measurements, evaluations and discussions on HPT-Ni were done by Eva-Maria Steyskal within the framework of her master thesis under my co-supervision [73].

Table 4.6: Chemical analysis of nickel according to specification of manufacturer (Goodfellow Cambridge Ltd.). Elements with concentrations less than 1 ppm are omitted.

Sample	**Elements and concentration [weight ppm]**								
Ni	Al	C	Ca	Co	Cr	Cu	Fe	Ta	V
	2.9	8.0	1.0	1.9	2.1	2.0	12.2	1.0	8.1

does not refine upon further deformation [48]. Thus it is ensured that all dilatometric samples have the same microstructure size.

Fig. 4.20 shows a dilatometric difference curve and its derivative at a heating rate of $3\,\mathrm{K/min}$. In contrast to the dilatometric measurement of the bcc metals Fe and Ta (Fig. 4.4, 4.16) the difference curve of Ni shows a substructure of 3 stages. The first stage - in the following referred to as stage A - ranging from 350 to $453\,\mathrm{K}$ shows a relative slow continuous length shrinkage. However, the subsequent second stage (B) exhibits a distinct sigmoidal annealing of free volume up to $493\,\mathrm{K}$. The last stage C extends to the maximum temperature of $673\,\mathrm{K}$ and mostly shows a small continuous shrinkage. Accordingly the temperature derivative has a small minimum peak in stage A and a pronounced one in stage B. Stage C usually does not show any obvious characteristics.

In Tab. 4.7 all axial measurements with the heating rate δ, the equivalent strain ε, the relative length changes $\Delta\ell/\ell_0$ and the minimum peak temperatures T_p in the respective stages are listed. $\Delta\ell/\ell_0$ exhibits no systematic dependence on the equivalent strain ε as it was to be expected due to the saturation deformation of all samples. The minimum peak temperatures T_p shift to higher temperatures with increasing heating rate, which is used for the kinetics analysis in Sec. 4.3.4.

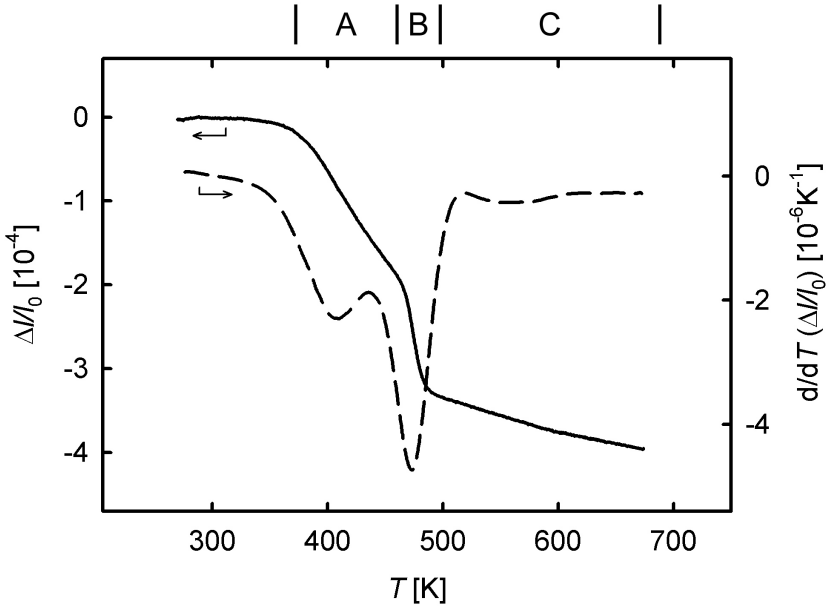

Figure 4.20: Dilatometric difference curve (—) of HPT-Ni upon linear heating with 3 K/min up to 673 K. The derivative after smoothing (- - -) showing minimum peaks at 395 and 472 K. A, B, and C indicate the different annealing stages.

Table 4.7: Dilatometric measurements on HPT-Ni. Heating rate δ (in [K/min]), equivalent strain ε, according to Eq. 3.1 and 3.2 (uncertainty $\Delta\varepsilon = 3$), relative length changes $\Delta\ell/\ell_0$ (in $[10^{-4}]$) in total and for the individual stages A and B as well as the temperatures T_p (in [K]) at the minimum peaks of the temperature derivatives in stage A and B. All measurements were performed on samples in axial direction. For the error analysis see Sec. 3.2.1. The maximum temperature in each run was 673 K.

HPT-Ni 5r axial

δ	ε	$\Delta\ell/\ell_{0,\mathrm{tot}}$	$\Delta\ell/\ell_{0,\mathrm{A}}$	$\Delta\ell/\ell_{0,\mathrm{B}}$	$T_{\mathrm{p,A}}$	$T_{\mathrm{p,B}}$
0.3	30	-9.9	-1.4	-3.7	388	439
1.5	30	-3.3	-1.5	-1.6	392	459
1.5	20	-4.2	-1.5	-2.3	395	463
1.5	12	-3.8	-1.5	-1.7	397	461
3.0	30	-5.6	-1.6	-1.7	394	472
3.0	20	-4.9	-2.0	-1.9	395	472
3.0	12	-4.0	-1.7	-1.7	403	473
6.0	30	-4.3	-1.9	-1.7	409	478
6.0	30	-3.7	-1.8	-1.6	408	478
6.0	20	-3.1	-1.1	-1.3	420	482
6.0	12	-5.7	-1.7	-2.0	414	480
6.0	12	-3.0	-1.3	-1.6	419	479
6.0	20	-3.7	-1.2	-1.6	438	480
10.0	30	-4.1	-1.8	-2.0	430	490

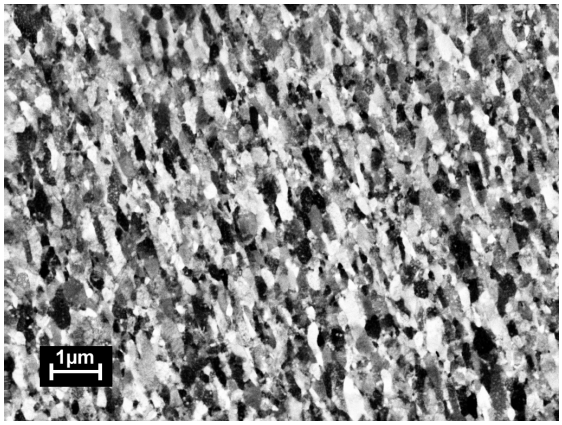

(a) HPT-Ni AR

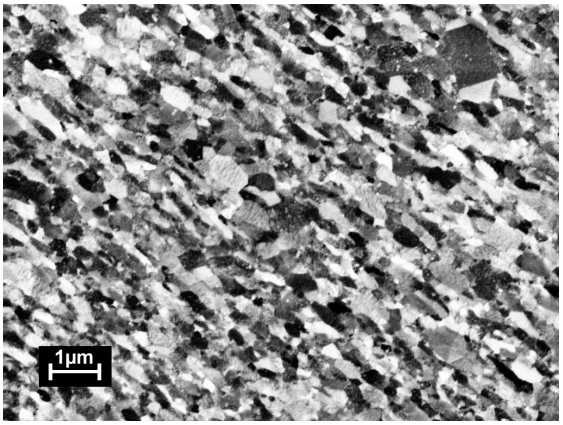

(b) HPT-Ni 453 K

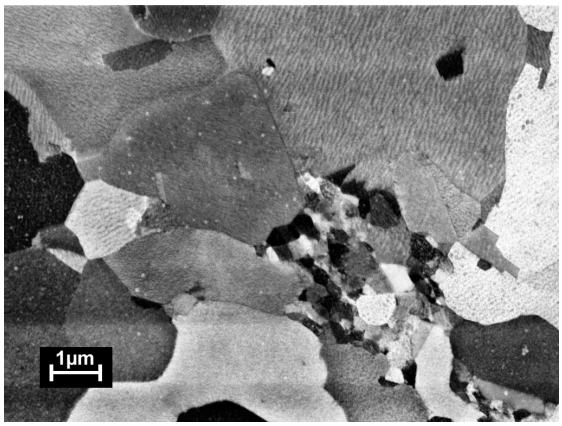

(c) HPT-Ni 493 K

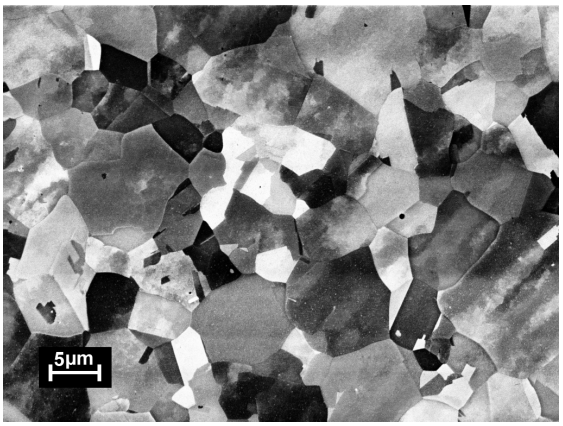

(d) HPT-Ni 673 K

Figure 4.21: Scanning electron micrographs of HPT-Ni with 5 revolutions in axial direction at different annealing steps. (For definition of the viewing direction see Fig. 3.7.) The magnification is 10 000 in a)-c) and 2 000 in d).

Fig. 4.21 shows SEM micrographs of HPT-Ni in the as-received state, after the stage A at 453 , after stage B at 493 K and at the maximum temperature of 673 K. In the AR state a lamellar grain structure can be observed, the grains are elongated in the tangential direction. Thus, for grain size analysis the line intercept method was applied (see Sec. 3.4). It delivered a grain diameter in the preferential (i.e. tangential) direction of $d_{\mathrm{t}} = 336$ nm and in the perpendicular (radial) direction $d_{\mathrm{r}} = 178$ nm, which corresponds to an aspect ratio of 1.9 of the crystallite diameter.

Upon annealing up to 453 K (i.e. up to the end of stage A) the grain size and the shape does not change very much (Fig. 4.21 b)). The line intercept analysis yields grain diameters of $d_{\mathrm{t}} = 298$ nm in tangential, $d_{\mathrm{r}} = 175$ nm in radial direction (aspect ratio of 1.7). Hence the grains after stage A are less elongated and even slightly smaller.

After stage B (Fig. 4.21 c)) large and rather spherical grains with island regions of small ones can be observed. Thus in stage B obviously most of the recrystallization takes place. The grain size analysis with the grain area method yields a mean value of 832 nm assuming spherical grains. Hence, the free volume annealed out in stage B (see Fig. 4.20) can be attributed to the removal of grain boundaries.

During stage C the grain growth continues, resulting in a mean grain size of $3.4\,\mu$m determined by the area method (Fig. 4.21 d)).

To reveal the entire microstructure of HPT-Ni in the as-prepared state, a SEM micrograph was made also in the radial direction (Fig. 4.22). The viewing direction is perpendicular to the HPT-axis with the axial direction vertical and the tangential direction horizontal (see sketch in Fig. 4.22). A lamellar grain structure very similar to the SEM micrograph in axial direction (Fig. 4.21 a)) can be observed. The grains are elongated in the tangential direction with a tilt of ca. $10°$. This tilt of elongated grains has been reported previously in HPT-deformed metals [5, 75]. The grain size analysis by means of the line intercept method revealed a grain diameter in the preferential tangential direction of $d_{\mathrm{t}} = 295$ nm and in the axial direction a slightly smaller value of $d_{\mathrm{a}} = 150$ nm compared to $d_{\mathrm{r}} = 178$ nm of Fig. 4.21 a). Summarizing, the grain shape can be described

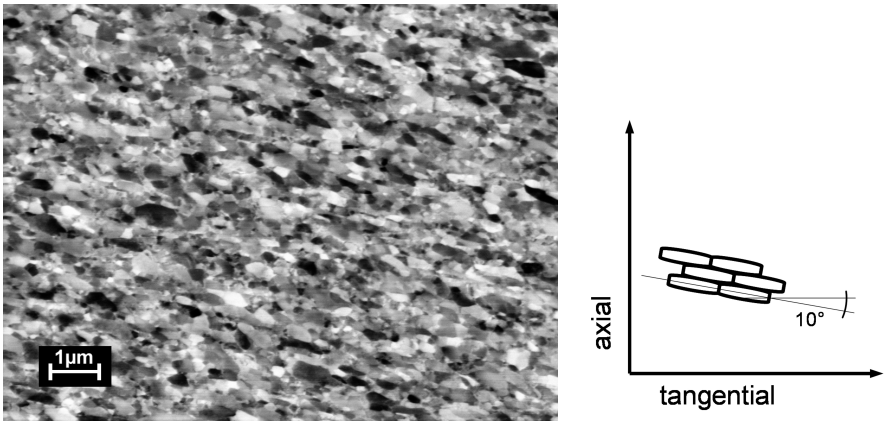

Figure 4.22: Scanning electron micrograph of HPT-Ni AR (deformation: 5 revolutions) taken in radial direction. The magnification is 10 000. The sketch aside shows the alignment of the micrograph with respect to the HPT axis as well as the tilt of the grains. (For definition of the viewing direction see Fig. 3.7.)

as ellipsoidal with the long axis in tangential direction and the ellipsoids slightly flattened in axial direction.

Electron Backscatter Diffraction

In order to verify the grain size results determined by means of SEM, also electron backscatter diffraction imaging (EBSD) was performed on the same Ni samples[7]. The inverse pole figure maps of this analysis is shown in Fig. 4.23.

The grain size evaluation by means of grain maps yields mean grain sizes ranging from a) 250 nm, b) 260 nm, c) 1.3 μm to d) 2.3 μm. The two latter values are less precise due to a limited number of grains available for analysis. The evaluation parameters are

[7] The EBSD measurements and evaluations were done by Dipl.-Ing. Klemens Jantscher and Univ.-Doz. Dr. Peter Pölt, Graz University of Technology.

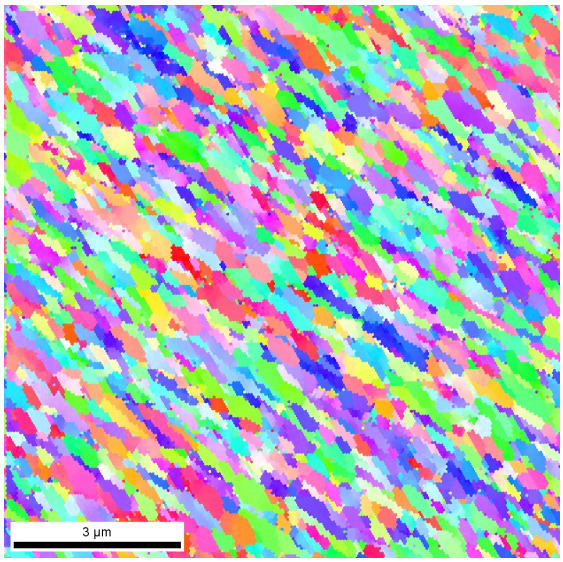

(a) HPT-Ni AR

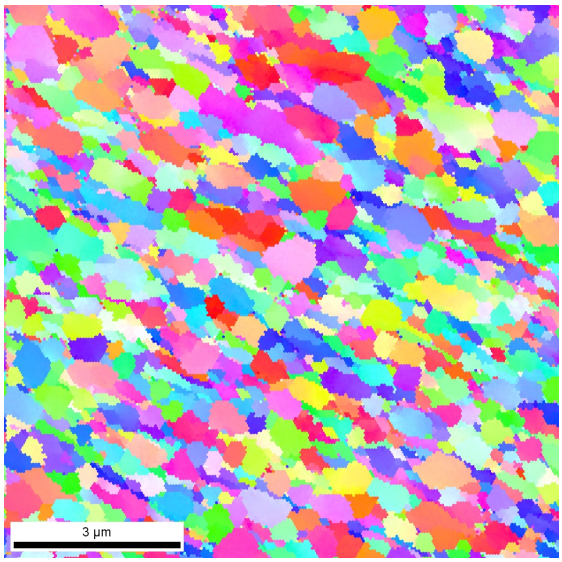

(b) HPT-Ni 453 K

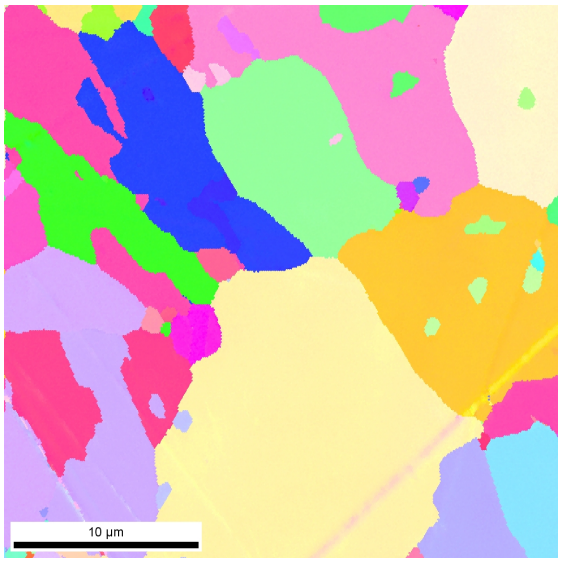

(c) HPT-Ni 493 K

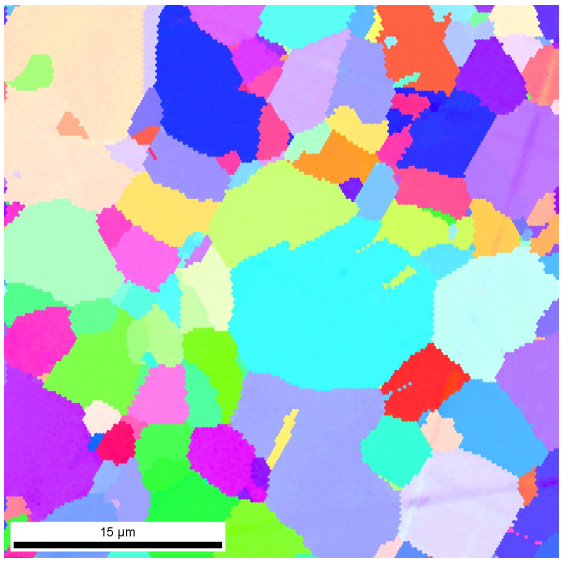

(d) HPT-Ni 673 K

Figure 4.23: EBSD images (inverse pole figures maps) of HPT-Ni with 5 revolutions in axial direction at different annealing steps. The magnification is ca. 12 000 in a) and b), 4 000 in c) and 3 000 in d).

4 pixel for the minimal grain size (grains smaller than 4 pixel are omitted for analysis), hexagonal-shaped pixels, 50 nm for the distance of the measuring points and 15° for the minimal misorientation angle defining a grain boundary.

The EBSD grain size analysis excellently confirms the grain growth observed in stage B already by SEM imaging. However, calculations requiring grain sizes are done with the SEM grain size data due to the benefit to determine grain sizes in specific directions easily.

Transmission electron microscopy

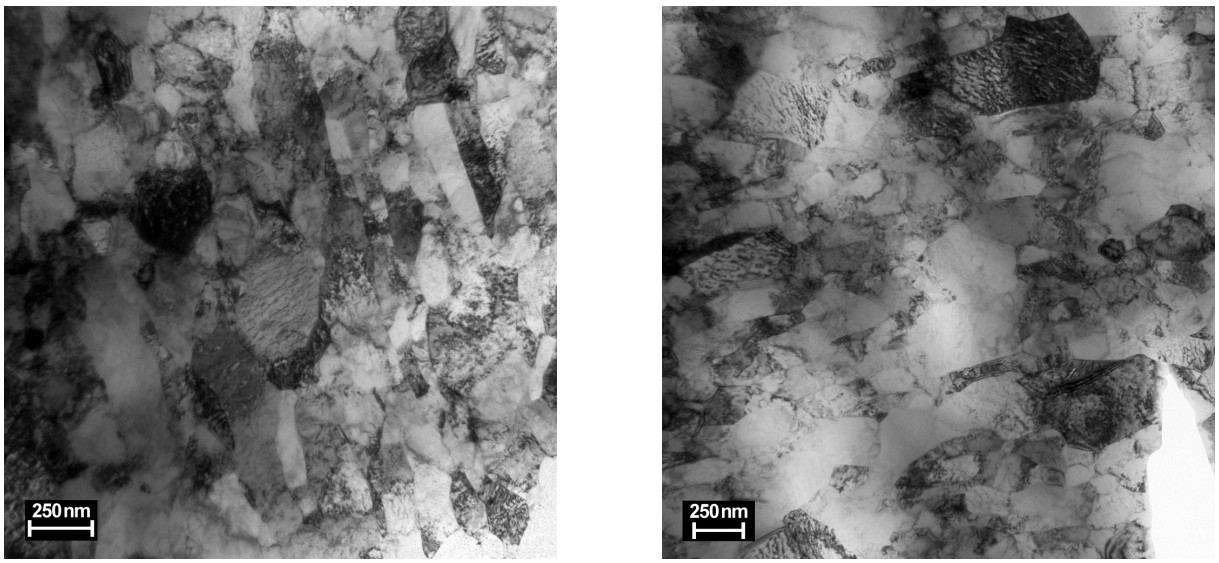

(a) HPT-Ni AR (b) HPT-Ni 453 K

Figure 4.24: Transmission electron micrographs of HPT-Ni with 5 revolutions in axial direction at room temperature and annealed at 453 K. The magnification is 52 000 in a) and 40 000 in b).

In order to investigate the microstructure during stage A more precisely, transmission electron microscopy (TEM) was performed on the samples used also for SEM (Fig. 4.21

a) and b)). The two resulting TEM images are presented in Fig. 4.24. Like in the SEM micrograph the AR sample exhibits small elongated grains. Moreover a high number of dislocations in almost all grains can be observed in the as-received state. After stage A (Fig. 4.24 b)) the grain structure remains similar, whereas the dislocation density is substantially reduced. In Chap. 5 a rough estimation of the amount of free volume annealing in stage A due to the removal of dislocations is given.

Positron annihilation

Positron lifetime measurements with the standard laboratory equipment were performed for the AR state. Saturation trapping with a lifetime of $\tau = 168 \pm 2\,\mathrm{ps}$ was revealed, which is slightly different to our previously published value of $178\,\mathrm{ps}$ [46] but more accurate due to a better source correction (see Sec. 3.3.1). This lifetime lies in between literature values for trapping at dislocations and at single vacancies [76, 77].

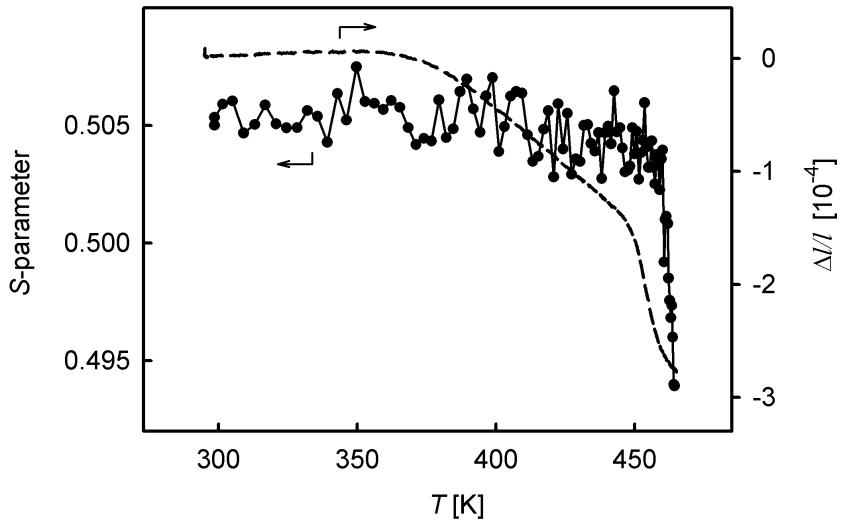

Figure 4.25: Doppler broadening S-parameter curve (-●-) and dilatometric difference curve (- - -) of HPT-Ni upon heating.

Like in the case of HPT-Fe (see Sec. 4.1.1) also HPT-Ni was investigated by means of Doppler broadening measurements at the high-intensity positron beam at the FRM II (see [46]). Again the non-linear heating program was recorded in order to perform subsequent dilatometric measurements under the same conditions. The results are shown in Fig. 4.25. Three stages of annealing can be distinguished. In the first one, no substantial change up to $380\,\mathrm{K}$ can be observed. The following stage, ranging from $380\,\mathrm{K}$ to almost $460\,\mathrm{K}$, a slight decrease of the S-parameter takes place followed by a steep decrease at $460\,\mathrm{K}$. The slight and the steep decrease can be identified as stage A and stage B, respectively, sketched in Fig. 4.20.

This gets evident looking at the corresponding length change in Fig. 4.25 performed with the identical temperature program. Dilatometry exhibits the characteristic slow length shrinkage from 365 to $445\,\mathrm{K}$ (stage A) and the distinct sigmoidal-shaped one (stage B) from $445\,\mathrm{K}$ up to the maximum temperature of $473\,\mathrm{K}$ as typical of HPT-deformed Ni (see Fig. 4.20). Due to the reduced maximum temperature compared with the measurement in Fig. 4.20 stage C here is not reached yet.

The following correlation between S-parameter and length change can be deduced (see Fig. 4.26). In the AR state the grain boundaries as well as intragranular defects, i.e., vacancy-type defects and dislocations, provide many trapping centres for the positrons. Due to saturation trapping the Doppler broadening S-parameter remains constant upon annealing up to $380\,\mathrm{K}$.

The slight decrease of the S-parameter in stage A ($380\,\mathrm{K}$ - $460\,\mathrm{K}$) indicates the annealing of free volume-type defects, since the *in-situ* measurement of a defect-free lattice would actually result in an increase of the S-parameter due to the thermal expansion of the lattice. An analogous behaviour could be observed for the W-parameter of Ni in literature [69] (page 109). Taking into account the constant crystallite size in this stage (see SEM, Fig. 4.21), the decrease of S-parameter and length indicates the annealing of

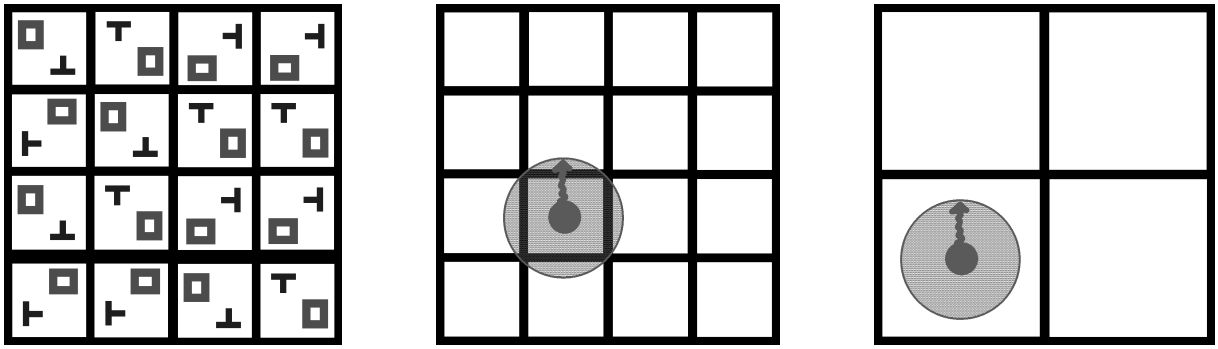

(a) as received (b) after stage A (c) after stage B

Figure 4.26: Positron trapping scheme at different annealing stages of HPT-deformed Ni. The various types of e^+-traps are indicated; square grid: grain boundaries, $\perp$: dislocations, $\square$: vacancy-type defects, shaded circle: regime probed by diffusing e^+.

vacancies and dislocations resulting in the situation sketched in Fig. 4.26 b). This conclusion is supported by comparing the trapping rates at vacancies and at grain boundaries. The value of annealed free volume in stage A amounts to 4.5×10^{-4}. Attributing this value to the concentration of vacancies yield a trapping rate of $\sigma_v C_v = 23 \times 10^{10}\,s^{-1}$, taking into account a specific vacancy trapping rate of $\sigma_v = 5 \times 10^{14}\,s^{-1}$. In contrast the trapping rate at grain boundaries calculates to $3\,\alpha/r = 3 \times 10^{10}\,s^{-1}$ [40] with the specific grain boundary trapping rate $\alpha = 10^3\,m^2 s^{-1}$ and a mean grain radius of $r = 100\,nm$. This more than seven times lower trapping rate at grain boundaries indicates a change of the positron trapping characteristics from saturation trapping at lattice vacancies below stage A to saturation trapping at grain boundaries above stage A.

Stage B is characterised by a steep decrease of the S-parameter and the relative length change, in which a distinct displacement of these two curves of about $20\,K$ is striking. The SEM images of Fig. 4.21 show strong grain growth in this stage. As it is sketched in Fig. 4.26 b) the positrons diffusion length L_+ is larger than the mean grain radius r

at the beginning of stage B. At the onset of grain growth the positrons can still reach the grain boundaries. Only when the crystallite size substantially exceeds the mean diffusion length L_+ (Fig. 4.26 c)) the S-parameter decreases dramatically. For a typical value for L_+ in metals is $200\,\text{nm}$, positrons start to annihilate from the defect-free state for grain sizes larger than $400\,\text{nm}$ in diameter. Beyond stage B positron annihilation in the free state becomes more and more predominant.

4.3.2 Orientation-dependent measurements

Similar as for high-purity HPT-Fe (Sec. 4.1.4) also HPT-Ni was analyzed regarding the spatial orientation of the dilatometry samples. Fig. 4.27 shows dilatometric measurements in axial, radial and tangential direction applying the same heating rate of $3\,\text{K/min}$ (for definition of the directions see Fig. 3.8). The different stages defined from the axial measurement can clearly be seen also in the radial and tangential case. The minimum peaks of the derivative, characterizing the maximum transition during recrystallization, are located at the same temperature of $475 \pm 2\,\text{K}$.
Whereas a relative length shrinkage can be observed for the axial and the radial sample in all stages, the stage A of the tangential sample is characterized by a distinct elongation. This behaviour was observed for all measurements in tangential direction. The anisotropic length change behaviour can also be observed considering the total relative length change in the different orientations. Whereas the stroke for axial sample amounts to -4.1×10^{-4}, it is only -2.5×10^{-4} for the radial and even smaller (-1.4×10^{-4}) for the tangentially orientated sample. Tab. 4.8 summarizes the radial and tangential measurements.
The substantial difference of the relative length changes in stage B between the axial and the tangential samples is used for calculations of the grain boundary excess volume (see Chap. 5).

Since HPT-Ni in the AR state exhibits a strong microstructural anisotropy (Fig. 4.21 a)), anisotropic annealing of free volume could be a possible explanation for the elongation

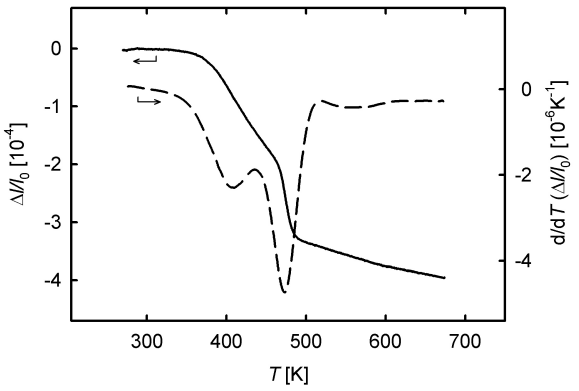

(a) HPT-Ni axial

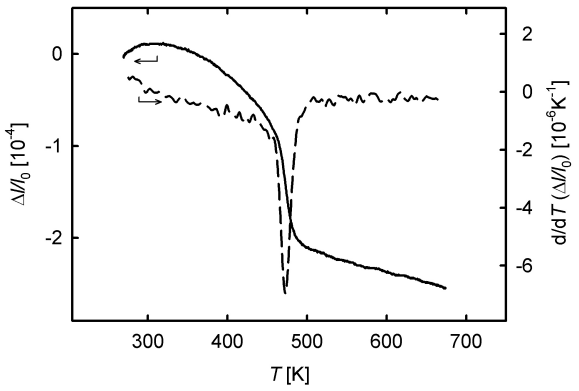

(b) HPT-Ni radial

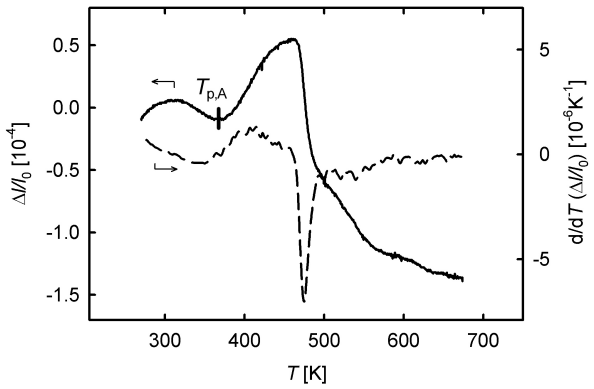

(c) HPT-Ni tangential

Figure 4.27: Dilatometric difference curves (—) of HPT-Ni in a) axial, b) radial and c) tangential direction upon linear heating with 3 K/min up to 673 K and derivatives after smoothing (- - -). For definition of the directions see Fig. 3.8.

Table 4.8: Dilatometric measurements on HPT-Ni in radial and tangential direction. Heating rate δ (in [K/min]), mean equivalent strain ε, according to Eq. 3.1 and 3.2 ($\Delta\varepsilon = 3$), the relative length changes $\Delta\ell/\ell_0$ (in $[10^{-4}]$) in total and for the stages A and B, the temperatures $T_{\mathrm{p,A}}$ (in [K]) at the beginning of the elongation, $T_{\mathrm{p,B}}$ ([K]) at the minimum peaks of the derivatives in stage B. For the error analysis see Sec. 3.2.1. The maximum temperature was 673 K.

HPT-Ni 5r tangential

δ	ε	$\Delta\ell/\ell_{0,\mathrm{tot}}$	$\Delta\ell/\ell_{0,\mathrm{A}}$	$\Delta\ell/\ell_{0,\mathrm{B}}$	$T_{\mathrm{p,A}}$	$T_{\mathrm{p,B}}$
3.0	26	-1.3	+0.7	-1.1	367	476
3.0	26	-2.2	+0.8	-1.0	361	477
6.0	26	-0.1	+0.5	-0.7	401	486
6.0	26	-0.9	+0.4	-0.8	394	487

HPT-Ni 5r radial

δ	ε	$\Delta\ell/\ell_{0,\mathrm{tot}}$	$\Delta\ell/\ell_{0,\mathrm{A}}$	$\Delta\ell/\ell_{0,\mathrm{B}}$	$T_{\mathrm{p,A}}$	$T_{\mathrm{p,B}}$
3.0	23	-2.6	-0.8	-1.2	-	473

prior recrystallization. A model for the anisotropic annealing of vacancies is presented in detail in Chap. 5.

Another explanation for the elongation of the tangential samples in stage A could be the presence of macrostresses (residual stress of first order) in the HPT samples. In order to clarify this item, XRD-studies were initiated in collaboration with J. Keckes[8]. Preliminar first results of these measurements are as follows. The XRD method used was the the $\sin^2\psi$ method [78, 79], in which the sample is measured with the azimuth at $\varphi = 0$ at different tilt angles ψ.
For the macrostress analysis a cross-section of a large HPT-Ni sample with dimensions of ca. $20 \times 7 \times 3\,\mathrm{mm}^3$ was prepared. The radial viewing direction allows the stress analysis in both, axial and tangential direction (cf. Fig. 3.7). Prior to measurements the sample was etched for $30\,\mathrm{min}$ in a solution of diluted nitric acid and copper(II) sulfate for elimination of potential preparation-induced stresses. The following macrostress analysis yielded no indication for compressive stresses neither in axial nor in tangential direction.

4.3.3 Stage B: more detailed analysis

The dilatometric measurements on HPT-Ni showed different amounts of length shrinkage in the recrystallization stage B for different orientated samples. Fig. 4.28 illustrates this issue for an axial and a tangential measurement. In addition, the dilatometric samples with the corresponding grain orientations are schematically depicted.

In total, 12 axial and 3 tangential measurements were performed with all samples prepared from the same HPT disc. Fig. 4.29 shows $\Delta\ell/\ell_{0,\mathrm{tot}}$ of these measurements, indicating the mean values and standard deviations. For the axial measurements $\Delta\ell/\ell_{0,\mathrm{mean}}$

[8] The XRD measurements and evaluations were done by Prof. Dr. Jozef Keckes, Leoben University.

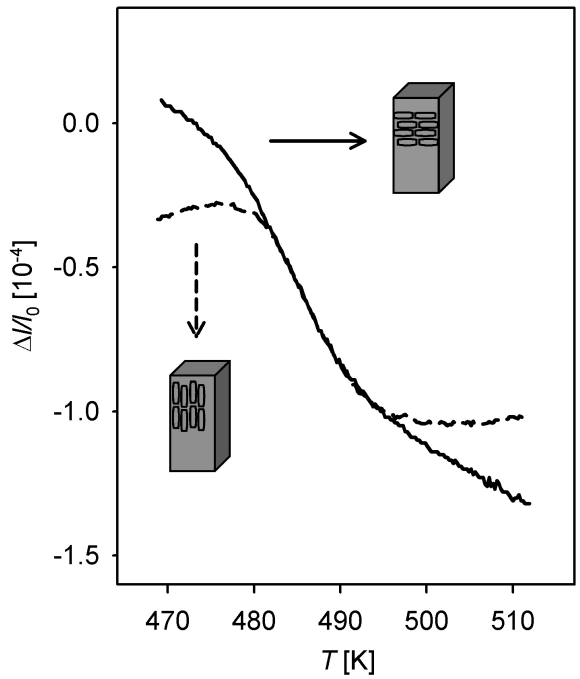

Figure 4.28: Dilatometric measurements of the recrystallization stage (stage B) of axial (—) and tangential (- - -) HPT-Ni samples. The $\Delta\ell/\ell_0$ curves are mutually shifted for better comparison (cf. Fig. 4.27).

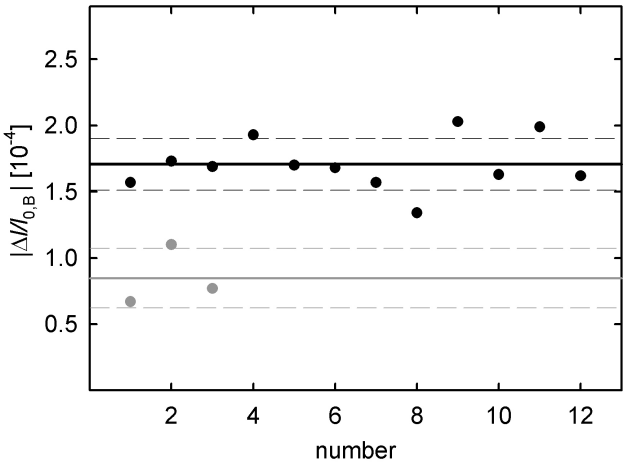

Figure 4.29: Absolute relative length change values in recrystallization stage B of 12 samples in axial (•) and 3 samples in tangential direction (•). Solid and dashed lines indicate the mean values and standard deviations, respectively.

amounts to $(-1.76 \pm 0.20) \times 10^{-4}$ and for the tangential direction a mean value of $(-0.85 \pm 0.24) \times 10^{-4}$ is obtained. These relative length change data – together with the grain sizes in the different measuring directions – can be used to determine the excess free volume (volume expansion) of a grain boundary in Ni. For the calculation see Chap. 5.

4.3.4 Analysis of kinetics

Since the dilatometric measurements on HPT-Ni were performed at different heating rates, the annealing kinetics can be studied. As it can be seen in Tab. 4.7 the minimum peak temperature T_p for the stage B shifts to higher temperatures with increasing heating rate. Fig. 4.30 shows this shift for the recrystallization stage in detail.

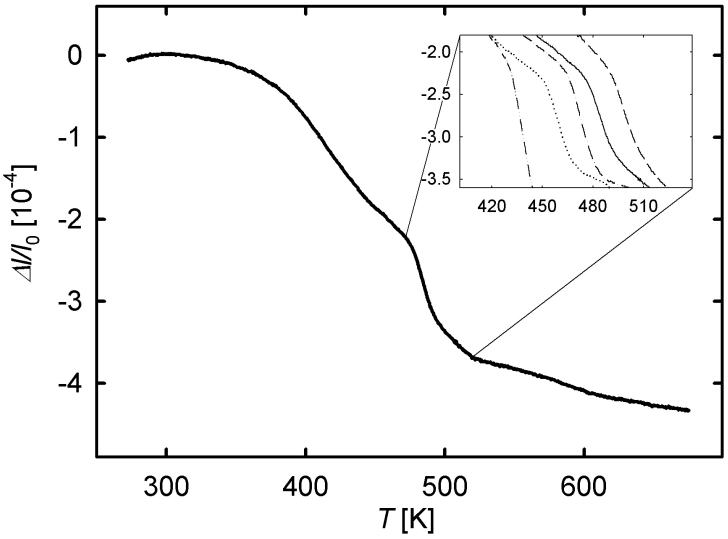

Figure 4.30: Dilatometric difference curve (—) of HPT-Ni upon linear heating with 6 K/min up to 673 K. The insert shows stage B for the measurements applying heating rate of 0.3, 1.5, 3, 6 and 10 K/min (curves from left to right).

The semilog Kissinger plot resulting from the analysis of the shift of T_p is shown in Fig. 4.31. With the slope of the regression line an activation energy of $Q = 1.20 \pm 0.04\,\mathrm{eV}$ according to Eq. 3.9 is obtained.

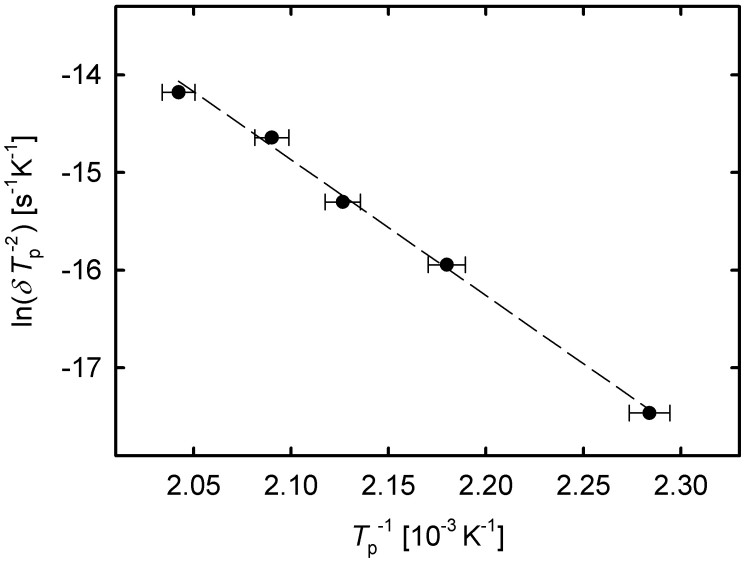

Figure 4.31: Kissinger plot (•) of HPT-Ni with 5 revolution and the appropriate regression line (- - -). The calculated activation energy Q amounts to $1.20 \pm 0.04\,\mathrm{eV}$ according to Eq. 3.9.

In addition to the above mentioned standard method of Kissinger, the recrystallization kinetics are furthermore analyzed by means of the more sophisticated theory of Johnson and Mehl [80], Avrami [81] as well as Kolmogorov [82] adapted for non-isothermal heating treatment. This analysis takes into account not only the shift but also the shape of the dilatometric difference curve.

The isothermal approach of Johnson-Mehl-Avrami-Kolmogorov (JMAK) describes the fraction $f_\mathrm{A}(t)$ of transformed material as:

$$f_{\mathrm{A}}(t) = 1 - \exp\left[-\left(K(T)t\right)^{n}\right] \tag{4.4}$$

at the time t and the temperature T with the Avrami exponent n and the rate constant $K(T)$. Its time derivative reads as follows:

$$\frac{\mathrm{d}f_{\mathrm{A}}}{\mathrm{d}t} = n(1 - f_{\mathrm{A}})\left[-\ln(1 - f_{\mathrm{A}})\right]^{\frac{(n-1)}{n}} K(T) \quad . \tag{4.5}$$

For the rate constant $K(T)$ an Arrhenius-type temperature dependence behaviour is assumed:

$$K(T) = K_0 \cdot \exp\left(-\frac{Q}{k_{\mathrm{B}}T}\right) \tag{4.6}$$

with the pre-exponential factor K_0, the activation energy Q and the Boltzmann constant k_{B}. Considering T as a function of time and $\mathrm{d}T/\mathrm{d}t =: \delta$ one can integrate Eq. 4.5 directly separating f_{A} and T [83]. This yields the non-isothermal solution [84]:

$$f_{\mathrm{A}}(t) = 1 - \exp\left[-\left(\frac{K_0 Q}{k_{\mathrm{B}}\delta}\int_x^{\infty}\frac{\exp(-x)}{x^2}\mathrm{d}x\right)^{n}\right] \tag{4.7}$$

$$\text{with} \quad x = \frac{Q}{k_{\mathrm{B}}T(t)} \quad . \tag{4.8}$$

The pre-exponential factor K_0 is correlated with the factor A of the method of Kissinger (Eq. 3.9) by the following equation:

$$A = \frac{k_{\mathrm{B}}K_0}{Q} \quad . \tag{4.9}$$

The numerical analysis was performed by means of a least-square fit according Eq. 4.7 and 4.8. The result is plotted in Fig. 4.32. Numerical fits yield $Q = 1.20\,\mathrm{eV}$ for the

activation energy, $K_0 = 1.92 \times 10^{10}\,\mathrm{s}^{-1}$ for the pre-exponential factor, and $n = 2.17$ for the Avrami exponent.

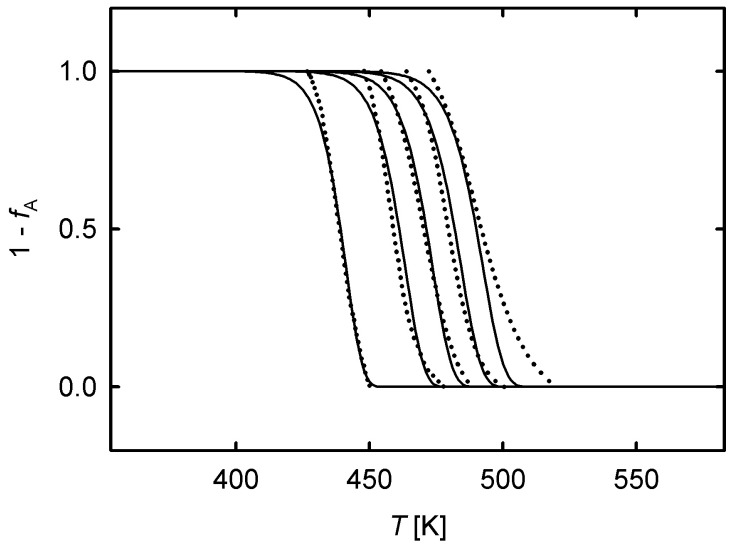

Figure 4.32: Normalized dilatometric difference curves of the recrystallization stage B in HPT-Ni showing the heating-rate dependent measured shift $(\cdots)$ (cf. insert in Fig. 4.30) and the non-isothermal JMAK kinetics based modeling (—). $1 - f_\mathrm{A}$ denotes the fraction of the non-recrystallized material at the temperature T.

The pre-exponential factor K_0 derived from the factor A of the Kissinger analysis amounts to $K_0 = (2.4 \pm 0.7) \times 10^{10}\,\mathrm{s}^{-1}$ according to Eq. 4.9.

In summary, both the standard Kissinger analysis as well as the more sophisticated JMAK-analysis adapted for linear heating yield kinetic data in excellent agreement.

4.4 Copper

Copper was the second investigated metal with fcc crystal structure. Four different samples were HPT deformed. Besides to dilatometric studies, SEM and positron annihilation, as well as differential scanning calorimetry (DSC) and residual electrical resistivity measurements (RER) were performed.
Two HPT billets, in the following labelled as Cu A and Cu B[9], with a purity of $99.99\,\%$ were HPT deformed with 3 revolutions and $2.65\,\text{GPa}$ resulting in a disk of $d = 30\,\text{mm}$ in diameter and $h = 3.5\,\text{mm}$ of height. Two thicker billets (Cu C and Cu D) with a purity of $99.995\,\%$ (see Tab. 4.9 for the chemical analysis) were deformed with 6 revolutions and $2.2\,\text{GPa}$ and yielded a large HPT disk of $d = 30\,\text{mm}$ and $h = 7\,\text{mm}$.

Table 4.9: Chemical analysis of copper used for sample series C and D according to specification of manufacturer (Alfa Aesar GmbH & Co KG). Elements with concentrations less than 1 ppm are omitted.

Sample	**Elements and concentration [weight ppm]**									
Cu C,D	Ag	As	Ni	O	P	Pb	S	Sb	Se	Sn
	8.0	1.0	1.0	2.0	2.0	1.0	8.0	1.0	2.0	1.0

4.4.1 Annealing behaviour and microstructure

For HPT-Cu a saturation deformation of $\varepsilon \approx 12$ is specified according to [66]. Hafok et al. [74] denote a value of $\varepsilon \approx 8$ for Cu of the same purity like Cu C and Cu D. Therefore, all samples were prepared from parts of the HPT discs located at radii larger than $4\,\text{mm}$ in order to guarantee saturation deformation according to Eq. 3.1 and 3.2.

[9] The samples Cu A and Cu B were HPT deformed and prepared by Dr. Daria Setman, Vienna University.

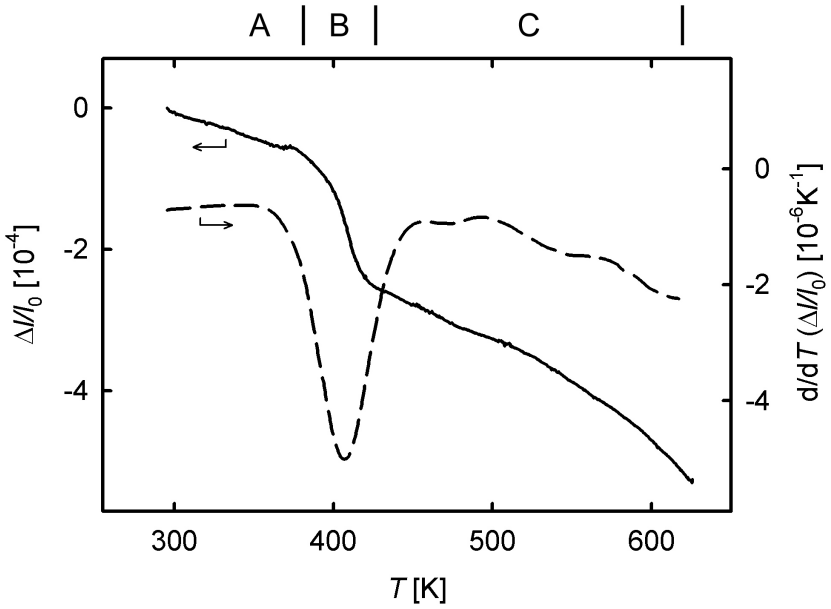

Figure 4.33: Dilatometric difference curve (—) of HPT-Cu A upon linear heating with 3 K/min up to 623 K, the derivative after smoothing (- - -) showing one pronounced minimum peak at 408 K, and A, B and C indicating the different annealing stages.

In Fig. 4.33 a dilatometric relative length change curve of HPT-Cu A at a heating rate of $3\,\mathrm{K/min}$ up to $623\,\mathrm{K}$ with the corresponding derivative is presented. Like in the case of HPT-Ni, several sub-stages in the length shrinkage can be clearly distinguished. Stage A exhibits a smaller relative length change compared to Ni and reaches only up to $372\,\mathrm{K}$. It is followed by stage B, ranging from $372\,\mathrm{K}$ to $435\,\mathrm{K}$, which shows a distinct sigmoidal length change, rather similar to the recrystallization stage of Ni. The major difference compared to Ni is stage C from $435\,\mathrm{K}$ to $623\,\mathrm{K}$. In the case of HPT-Cu this stage is characteristic for all measurements and yields a major contribution to the total relative length change.

Tab. 4.10 summarizes all dilatometric measurements, including the results for different sample orientation.The Cu A and Cu B samples were prepared perpendicular to the HPT axis (in plane) without specifying the direction any further. The results can be subsumed as follows:

- In contrast to Ni the length change characteristics is rather similar for all directions.
- No systematic dependence of the total relative length change $\Delta\ell/\ell_{0,\mathrm{tot}}$ on the equivalent strain ε can be observed.
- The minimum peak temperatures $T_{\mathrm{p,B}}$ shift to higher temperatures with increasing heating rate.
- For the samples prepared from the large HPT disc (Cu C, Cu D) $T_{\mathrm{p,B}}$ is about $30\,\mathrm{K}$ higher compared to Cu A and Cu B.

Fig. 4.34 shows SEM micrographs of HPT-Cu B in the as-received state, after stage B at $428\,\mathrm{K}$ and at the maximum temperature of $623\,\mathrm{K}$. In the as-received state a microstructure with slightly elongated grains can be observed. The grain size analysis revealed a

Table 4.10: Dilatometric measurements on HPT-Cu. Heating rate δ (in [K/min]), equivalent strain ε, according to Eq. 3.1 and 3.2 (uncertainty $\Delta\varepsilon = 3$), the relative length changes $\Delta\ell/\ell_0$ (in $[10^{-4}]$) in total and for stage B, the peak temperatures $T_{\mathrm{p,B}}$ (in [K]) for stage B as well as the sample orientation. The maximum temperature was 623 K for Cu A (1.5 and 3 K/min) and for Cu B; 673 K for all other measurements. For the error analysis see Sec. 3.2.1. For definition of axial, tangential and radial see Fig. 3.8.

δ	ε	$\Delta\ell/\ell_{0,\mathrm{tot}}$	$\Delta\ell/\ell_{0,\mathrm{B}}$	$T_{\mathrm{p,B}}$	orientation
HPT-Cu A					
1.5	29	-2.7	-1.1	401	in plane
3.0	38	-5.3	-1.9	408	in plane
6.0	23	-8.4	-2.7	424	in plane
HPT-Cu B					
1.5	39	-1.7	-1.0	400	in plane
3.0	39	-2.1	-1.0	410	in plane
6.0	39	-3.3	-0.9	425	in plane
HPT-Cu C					
3.0	22	-5.7	-1.8	433	axial
3.0	25	-3.7	-1.1	439	tang.
3.0	29	-4.3	-1.2	436	radial
HPT-Cu D					
1.25	39	-8.9	-2.1	421	axial
1.25	26	-9.5	-2.4	414	axial
2.5	27	-6.1	-1.4	426	axial
5.0	34	-5.6	-1.8	438	axial
5.0	25	-7.2	-2.2	444	tang.
5.0	29	-6.2	-1.6	442	radial
10.0	30	-9.6	-1.9	453	axial

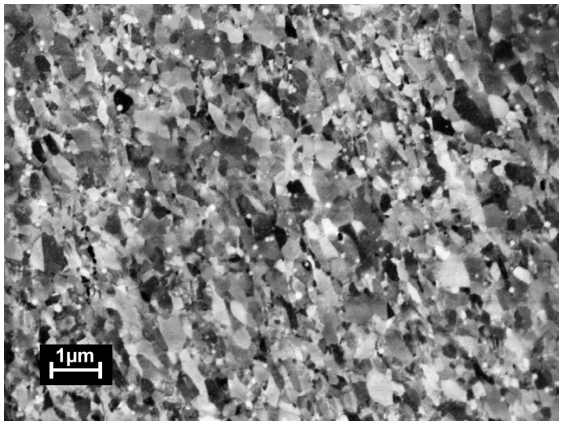

(a) HPT-Cu B AR

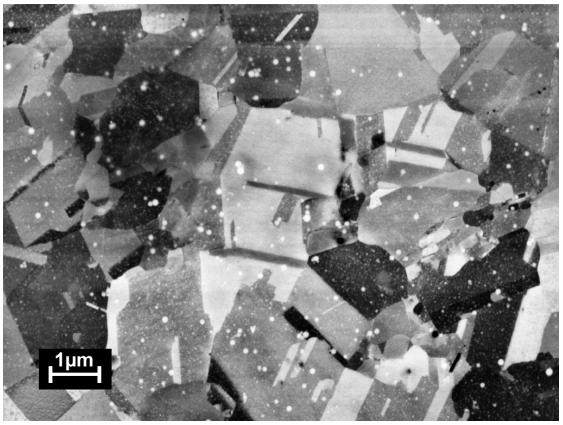

(b) HPT-Cu B 428 K

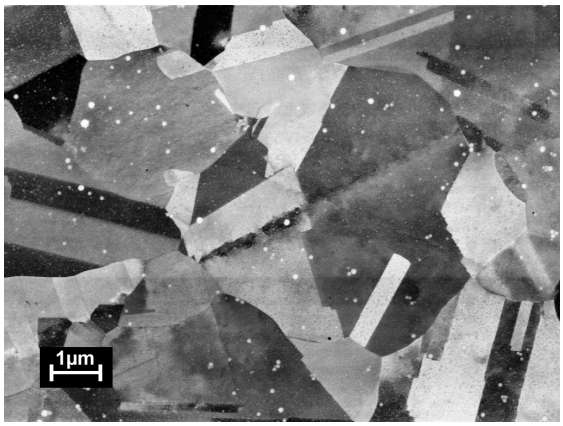

(c) HPT-Cu B 623 K

Figure 4.34: Scanning electron micrographs of HPT-Cu B with 3 revolutions in radial viewing direction at different annealing steps. The magnification is 10 000 for all micrographs.

mean grain size of $d = 242\,\text{nm}$. After stage B an isotropic recrystallized microstructure occurs with twinning in parts of the grains. The grain size in this state amounts to $d = 790\,\text{nm}$ (Fig. 4.34 b)). During stage C the grain growth and twinning are proceeding resulting in a diameter of $d = 1.54\,\mu\text{m}$.

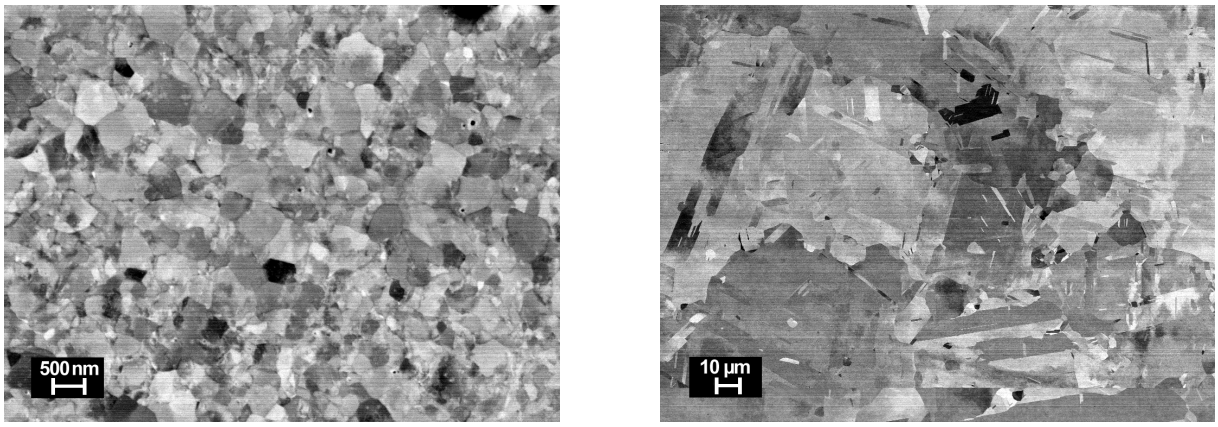

(a) HPT-Cu D AR (b) HPT-Cu D 723 K

Figure 4.35: Scanning electron micrographs of HPT-Cu D with 6 revolutions in axial direction a) in the as-prepared state at a magnification of 28 000, and b) after annealing at 723 K at a magnification of 1 000.

The SEM micrographs of HPT-Cu D (Fig. 4.35) revealed a rather similar picture compared to HPT-Cu B. The grain size analysis of the as-prepared state by means of the line intercept method yielded a slightly larger diameter of 257 nm. However, no elongation of the grains can be observed. For the sample annealed at 723 K a diameter of $7.73\,\mu\text{m}$ could be deduced. This larger size compared to HPT-Cu B (cf. Fig. 4.34 c)) is due to the higher annealing temperature employed for HPT-Cu D.

A more detailed picture of the microstructure prior to stage C is obtained from transmission electron microscopy (TEM). The TEM micrograph of a HPT-CU B sample annealed at 420 K (Fig. 4.36) shows relatively large twinned grains with a grain size sim-

Figure 4.36: Transmission electron microscopy image of HPT-Cu B with 3 revolutions in radial direction annealed at 420 K. The magnification is 17 500.

ilar to that of the SEM micrograph (cf. Fig. 4.34 b)). Some dislocations mostly at grain boundaries can be observed.

Positron annihilation

Positron lifetime spectroscopy in the standard laboratory technique was performed for HPT Cu A in the as-prepared state and for HPT Cu D after stage B. For the as-prepared Cu A one single lifetime of 170 ± 2 ps could be determined, which is slightly different to our previously published result of 160 ps [46] but more accurate due to a better source correction (see Sec. 3.3.1). This value lies in the typical regime of e^+-lifetimes at monovacancies and dislocations in copper [85, 86].

To determine the structural defects still present after the recrystallization stage B the HPT Cu D sample was annealed up to 458 K (i.e. up to the end of stage B), and cooled down rapidly. Apart from a short positron lifetime of $\tau_1 = 74$ ps with 28.4 %, a defect

lifetime of $\tau_{\mathrm{d}} = 160\,\mathrm{ps}$ with $71.6\,\%$ was revealed. A mean lifetime of $\tau_{\mathrm{m}} = 136\,\mathrm{ps}$ and – according to the simple e^+ trapping model – a bulk lifetime of $\tau_{\mathrm{b}} = 121\,\mathrm{ps}$ is obtained from τ_1, τ_{d} and the corresponding intensities. Literature values for τ_{b} ranging from 122 [85] to $130\,\mathrm{ps}$ [86] confirm the applicability of the simple trapping model.

The *in-situ* Doppler broadening measurements at the high-intensity positron beam at the FRM II delivered similar results compared to HPT-Ni (see Sec. 4.3.1). Fig. 4.37 shows the S-parameter in dependence of the heating temperature T. The temperature program was recorded in order to perform a dilatometric measurement under the same conditions. The Cu samples used for positron annihilation and dilatometry were prepared out of the same HPT disk Cu C.

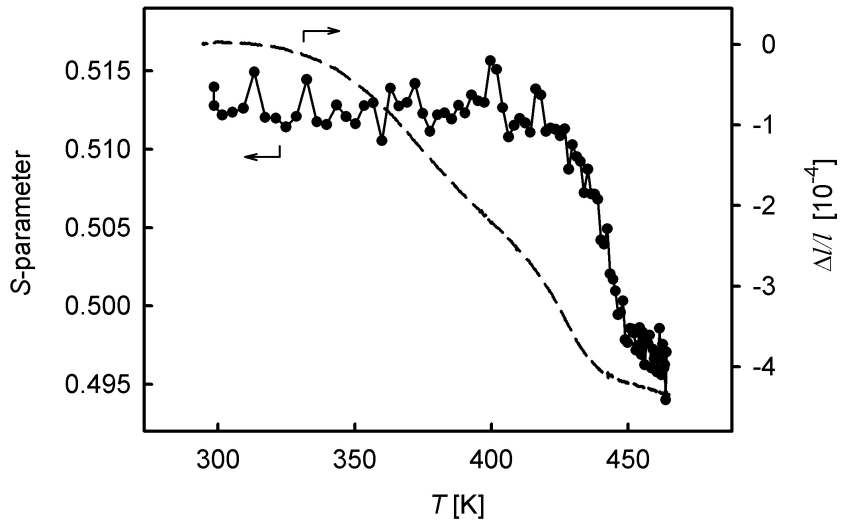

Figure 4.37: Doppler broadening S-parameter (–●–) and dilatometric difference curve (- - -) of HPT-Cu C upon heating.

The S-parameter remains constant up to $400\,\mathrm{K}$ due to saturation trapping of positrons. In stage A from 400 to $430\,\mathrm{K}$ S decreases slowly. Afterwards from $430\,\mathrm{K}$ to the maximum temperature of $464\,\mathrm{K}$ a steep S-parameter decrease is observed (stage B). This is in good accordance with positron lifetime measurements (see above), where at a

temperature of $458\,\mathrm{K}$ positron annihilation partially in the defect-free bulk could be detected.

Stage A in the dilatometric difference curve sets in at ca. $330\,\mathrm{K}$ and reaches up to ca. $410\,\mathrm{K}$ showing a moderate length shrinkage. From $410\,\mathrm{K}$ to $450\,\mathrm{K}$ a steep decrease of $\Delta\ell/\ell_0$ can be observed.

As described in detail in Sec. 4.3.1, the annealing behaviour in Fig. 4.37 can be understood by means of the scheme shown in Fig. 4.26 considering also the SEM micrographs of the corresponding annealing stages (Fig. 4.34). In summary, annealing of vacancies-type defects and dislocations takes place in stage A. In stage B grain growth occurs causing the observed decrease of the S-parameter and of $\Delta\ell/\ell_0$. The displacement of the two curves in stage B can be explained with the positron diffusion length, which is at the beginning of the recrystallization sufficiently large for the positrons to reach the grain boundaries (see Fig. 4.26).

4.4.2 Orientation-dependent measurement

In contrast to HPT-Fe and HPT-Ni, where the dilatometric measurements revealed a continuous shrinkage in axial and a partial elongation in tangential direction (see Sec. 4.1.4 and 4.3.2), HPT-Cu showed a different behaviour regarding the sample orientation. Fig. 4.38 exhibits the relative length change curves in the three orthogonal directions for HPT-Cu D at a heating rate of $5\,\mathrm{K/min}$. No substantial differences in the annealing behaviour can be observed. The differences between the total length changes discernible in Fig. 4.38 are within the statistical error. (cf. Tab. 4.10).

The reason for the different dilatometric result of the tangential Cu sample compared to the tangential Ni sample can possibly found in the different microstructure of the materials. This issue is discussed in detail in Chap. 5.

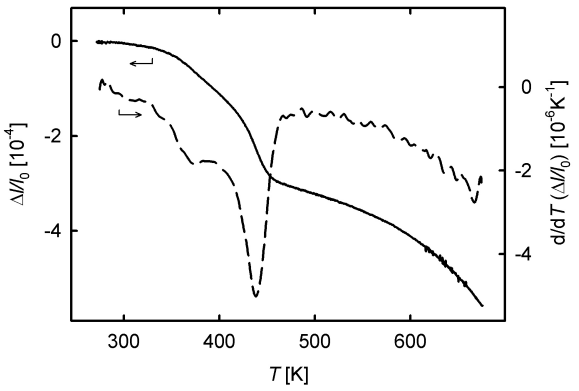

(a) HPT-Cu D axial

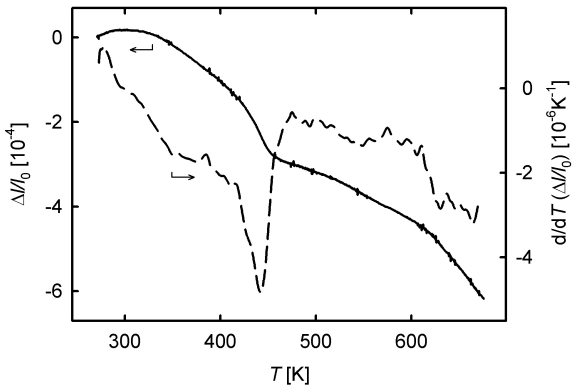

(b) HPT-Cu D radial

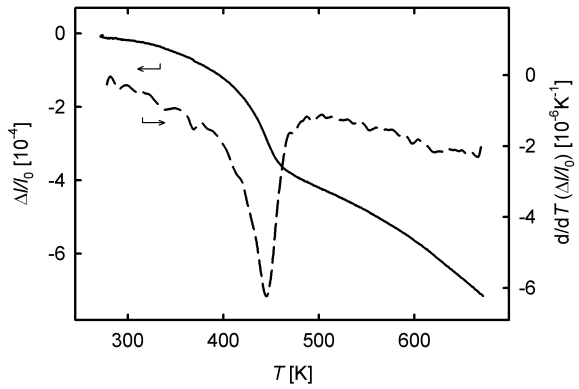

(c) HPT-Cu D tangential

Figure 4.38: Dilatometric difference curves (—) of HPT-Cu D in a) axial, b) radial and c) tangential direction upon linear heating with 5 K/min up to 673 K and derivatives after smoothing (- - -). For definition of the directions see Fig. 3.8.

4.4.3 Analysis of kinetics

The recrystallization kinetics of HPT-Cu can be deduced from the Kissinger analysis of the dilatometric data (see Sec. 3.2.4). Different heating rates ranging from 1.25 to $10\,\mathrm{K/min}$ were applied for the samples A, B, and D, causing a shift of the minimum peak of the derivatives (cf. Tab. 4.10). The temperature of the minimum peak $T_{\mathrm{p,B}}$ together with the corresponding heating rate δ is shown in Fig. 4.39 in the Kissinger representation.

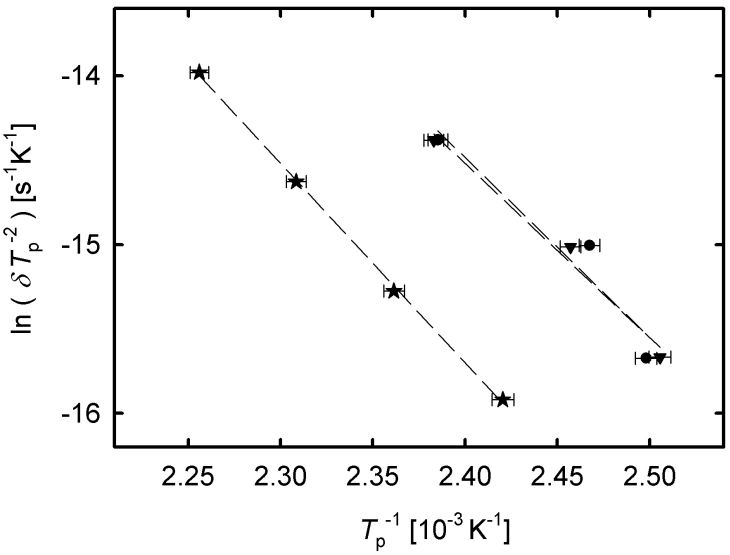

Figure 4.39: Kissinger plot of HPT-Cu A (•), HPT-Cu B (▼) and HPT-Cu D (★). $T_{\mathrm{p,B}}$: Minimum peak temperatures (see Tab. 4.10). δ: Heating rate ($\delta = 1.25$ to $10\,\mathrm{K/min}$). ---: Linear Arrhenius-type fit.

According to Eq. 3.9 the slope of the regression lines can be used to calculate the activation energies Q of the recrystallization process. For sample series A, B, and D values of Q of 0.92 ± 0.07 , 0.89 ± 0.02 and 1.02 ± 0.01 eV are obtained, respectively. The errors are deduced from the regression analysis.

Enhanced values of both Q and T_{p} can be observed for the sample series D compared to A and B. This is remarkable since the samples D are of slightly higher purity, thus containing less stabilizing impurities. The reason for this behaviour can be found in the lower pressure applied during HPT deformation (2.2 for D vs. 2.65 GPa for sample series A and B). Indeed, as reported by Setman et al. [9] from DSC measurements on HPT-Cu, the minimum peak temperatures T_{p} as well as the activation energy Q are enhanced for low HPT pressure compared to high pressure. A lower total strain has the same effect [9].

4.4.4 Comparison with differential scanning calorimetry

The kinetics of recrystallization was also studied exemplary for sample series D by means of differential scanning calorimetry (DSC)[10]. For that purpose 14 samples at three different positions in the HPT-disk were prepared. Six samples were cut out at a radius of $r = 9$ mm ($\varepsilon = 28$) at different heights in the disk. Four samples were each prepared at radii of $r = 9.3$ and $r = 7.3$ mm which corresponds to an equivalent strain of $\varepsilon = 29$ and 23, respectively. Thus, all samples are in saturation deformation.

By means of a power-compensated DSC (Perkin Elmer DSC7) the heat flow difference upon linear heating of a HPT sample is measured. A subsequent re-run of the measurement served as reference. Defect annealing can be monitored by DSC owing to the exothermic heat flow associated with the annealing process. The total heat release is related to the specific annealing process as well as to the concentration of annealing defects [87].

[10] The DSC preparation, measurements and evaluation were done by Dr. Daria Setman, University of Vienna.

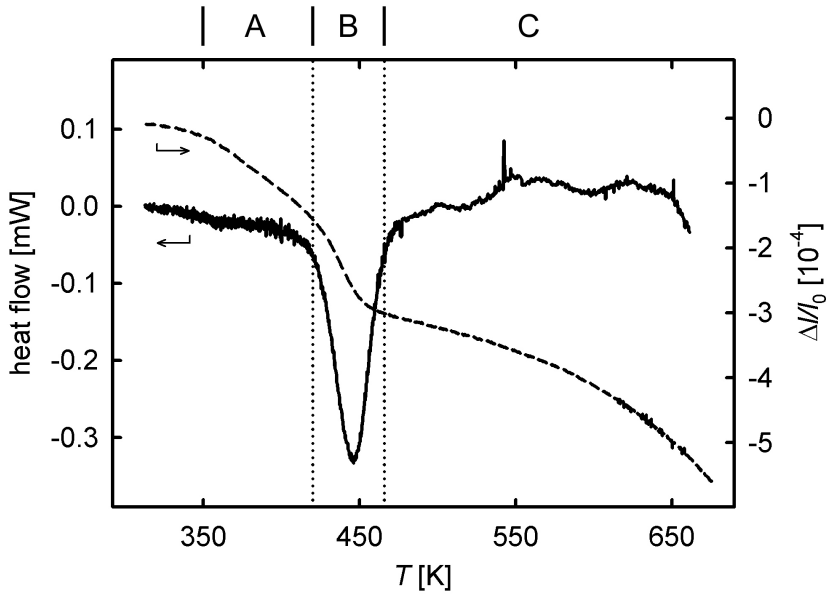

Figure 4.40: DSC heat flow (—) as well as relative length change (- - -) of HPT Cu D upon annealing up to 673 K with 5 K/min. The vertical lines indicate stage B as revealed from dilatometry.

All DSC measurements on HPT Cu D exhibit one exothermic peak centered in a temperature range where the recrystallization stage B in the dilatometric measurements was observed. Fig. 4.40 shows exemplarily a DSC curve together with a dilatometric measurement.

Applying higher heating rates caused a shifting of the DSC peak to higher temperature. The corresponding Kissinger plots of the samples at $r = 9$, 7.3, and 9.3 mm are shown in Fig. 4.41. The Kissinger analysis (Sec. 3.2.4) yields an activation energy Q of 1.03 ± 0.02 eV for the samples at $r = 7.3$ and 9.3 mm, and of 0.94 ± 0.06 eV for those at $r = 9$ mm. The higher error in the last result may be due to inhomogenities across the height of the disk (see Sec. 3.1).

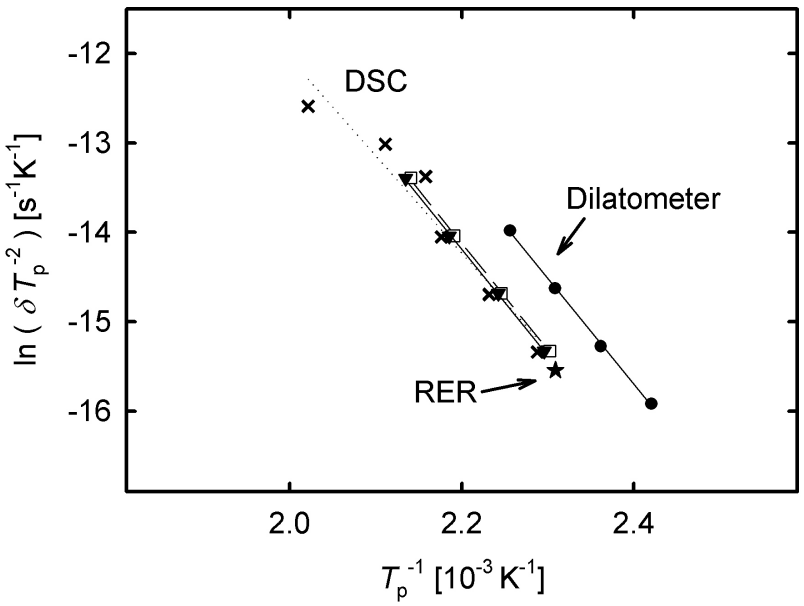

Figure 4.41: Kissinger plots of HPT-Cu D with 6 revolutions determined by means of dilatometry (•), DSC ($r = 7.3$ mm □, 9.3 mm ▼, 9 mm ×), and RER (★) with heating rates ranging from 1.25 to 50 K/min and the appropriate regression lines (- - -). For the single RER point see Sec. 4.4.5.

For comparison, Fig. 4.41 also shows the Kissinger analysis results derived by dilatometry (HPT-Cu D, Fig. 4.39). A single point determined by means of residual electrical resistance measurements (RER, see Sec. 4.4.5) assuming a pseudo-heating rate is also shown for the sake of completeness.

Although the temperatures of the dilatometry peaks are located at general lower temperatures, the dilatometry temperature range of stage B fits perfectly to the temperature range of energy release determined by DSC (see Fig. 4.40). Since stage B in the dilatometric measurements could be related to recrystallization, the released enthalpy ΔH can be attributed to grain boundaries. ΔH is determined from the area of the DSC peak in stage B. The mean enthalpy value deduced from all DSC measurements performed on HPT-Cu D amounts to $\Delta H = -0.92 \pm 0.07\,\mathrm{J/g}$.

The released enthalpy ΔH is connected to the the grain boundary energy γ according to following: In a simple model of cubic crystals with size d the ratio of total area of interfaces to volume amounts to $3d^2/d^3 = 3/d$. The released enthalpy ΔH_V per unit volume therefore yields $3\gamma/d$, which corresponds per unit mass to $\Delta H_\mathrm{m} = 3\gamma/(\rho\, d)$ with ρ the mass density. Written in terms of γ,

$$\gamma = \frac{\Delta H_\mathrm{m} \rho\, d}{3} \tag{4.10}$$

is obtained. Attributing the mean value of the released enthalpy ΔH of $0.92 \pm 0.07\,\mathrm{J/g}$ to the removal of grain boundaries totally, and taking the initial grain size d of $257 \pm 10\,\mathrm{nm}$ (deduced from SEM, Fig. 4.35), a grain boundary energy of $\gamma = 0.70 \pm 0.08\,\mathrm{Jm^{-2}}$ is obtained taking into account the bulk density $\rho_\mathrm{Cu} = 8.92\,\mathrm{g/cm^3}$. This value is reported to be typical of relaxed grain boundaries in Cu [88].

In summary, DSC shows, that grain boundaries which disappear in stage B are in a relaxed state.

4.4.5 Comparison with residual electrical resistance measurements

For HPT-Cu also residual electrical resistance (RER) measurements were performed[11]. Since lattice defects give rise to charge carrier scattering, RER similar to DSC and dilatometry can be applied for studies of defect annealing.

By means of spark erosion two samples in axial direction (see Fig. 3.8) with an equivalent strain of $\varepsilon = 37$ were prepared. The resistance was measured at liquid helium temperature by means of the conventional four-wire method. After each measurement the samples were annealed isochronally for 10 min in steps of 20 K. This corresponds to a pseudo-heating rate of 2 K/min. For temperatures below 473 K, the temperature treatment was made in an oil bath, for temperatures beyond in Ar atmosphere. By subtracting the residual resistance at the final annealing step, the relative resistance change $\Delta\rho/\rho_0$ was determined.

Fig. 4.42 exhibits the resulting RER change curve. The relative resistivity given for each annealing step represents the mean value of two rather similar measurements performed on the identically prepared samples. A dilatometric measurement of Cu D with a similar heating rate of 2.5 K/min is superimposed.
In the resistance change three distinct sub-stages can be discerned, clearly identifiable as the characteristic annealing stages A, B, and C from the relative length change measurements. This similarity of the RER and the dilatometry curves is remarkable.

Differentiating the RER measurement curve, a plot similar to the DSC measurements is obtained (not shown). The minimum peak temperature of the derivative at ca. 433 K together with the pseudo-heating rate of 2 K/min were used as proof for the Kissinger analysis of HPT Cu D (see Fig. 4.41).

[11] The RER preparation, measurements and evaluation were done by Dr. Daria Setman, University of Vienna.

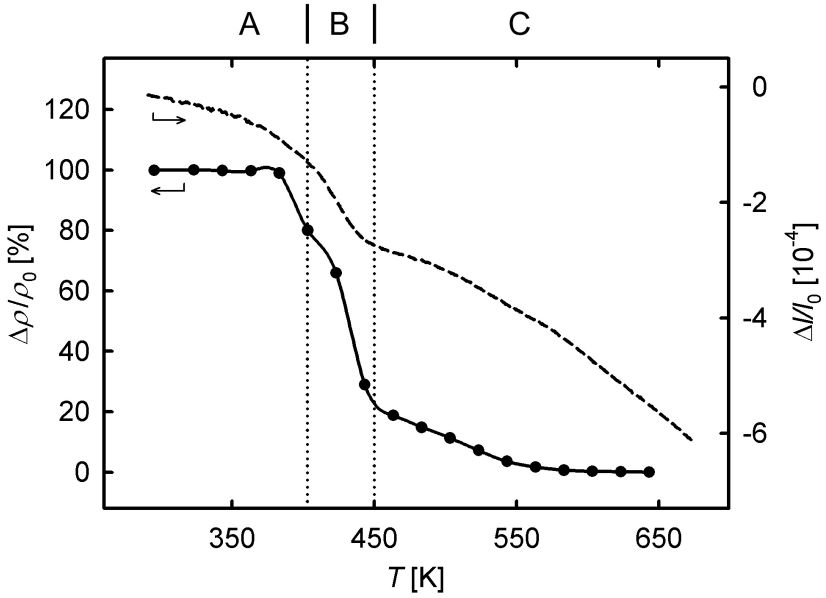

Figure 4.42: Relative electrical resistance change (-●-) of HPT-Cu D in dependence of the annealing temperature. $\Delta\rho/\rho_0$ is the average of two RER measurements on two identical samples. A dilatometric length change curve (- - -) of Cu D with a similar heating rate of 2.5 K/min is superimposed. The annealing stages A, B, and C are indicated by dotted vertical lines.

5
Discussion

Bulk nano- to ultra-fine grained samples of Fe, Ta, Ni and Cu – synthesized by means of high pressure torsion – were analyzed by a multitude of methods. Systematic investigations were performed with dilatometry and positron annihilation regarding type and amount of defects as well as the defect annealing kinetics. The microstructure was analyzed by means of electron microscopy (SEM and TEM) and microhardness measurements. Influences of the sample purity and sample orientation could be discerned.

In the following the kinetics of defect annealing, the fundamental parameter of grain boundary excess volume, the total free volume and its origin as well as the issue of anisotropy is discussed. We start the discussion with an overview of the HPT samples, the grain size achieved by HPT deformation, and the mean total volume reduction as determined by dilatometry (see Tab. 5.1).

As the comparison in Tab. 5.1 shows, the microstructure depends on the melting point as well as on the purity of the corresponding metal. The smallest grains could be achieved in the case of Ta, which has the highest melting point of $T_{\mathrm{m}} = 3290\,\mathrm{K}$. A com-

Table 5.1: Overview of the HPT metals studied in the present work, with the grain size d_1 in the as-received state and the total volume reduction $\Delta V/V_{0,\mathrm{tot}}$ deduced from the mean total relative length changes upon annealing (Eq. 3.4).

HPT samples overview

Material	d_1 [nm]	$\Delta V/V_{0,\mathrm{tot}}$ [10^{-4}]
ARMCO-Fe	144	20 - 30
HP-Fe	320	30
Ta	50 - 100	9
Ni	150	14
Cu A,B	242	12
Cu C,D	257	20

paratively larger grain size was observed for Cu with $T_\mathrm{m} = 1358\,\mathrm{K}$.

However, the largest grain size after HPT deformation occured for high-purity Fe. Comparing the grain sizes of ARMCO-Fe and HP-Fe in saturation deformation, a strong dependence on the sample purity is obvious. This issue has already been investigated more detailed and can be explained with a dynamic recrystallization during the deformation due to the lack of stabilizing impurities [5].

The total volume reduction $\Delta V/V_{0,\mathrm{tot}}$ – deduced from the mean total relative length changes upon annealing – is ranging from 9 to 30×10^{-4}. The smallest value was revealed for Ta, for which almost no recrystallization could be observed upon annealing at $773\,\mathrm{K}$. For the other materials, showing strong grain growth upon annealing, an estimation of the amount of free volume, localized at the various defects, is given in the section *total free volume* (see below).

Kinetics of annealing

In the present work dilatometry proved to be an excellent method to study defect kinetics of HPT deformed materials, owing to the possibility of defect annealing measurements in dependence of the heating rate. The results were evaluated applying thermal analysis methods such as the method of Kissinger (see Sec. 3.2.4). In the case of Ni, the theory of Johnson, Mehl, Avrami and Kolmogorov [80–82] for isothermal transformation processes was used in addition, by adapting this JMAK-theory for non-isothermal linear heating treatment as it was done by Henderson ([83], see Sec. 4.3.4).

For the fcc metals the analysis of kinetics was employed for stage B exclusively, yielding the activation energy for recrystallization. In the case of the bcc metals, only one broad annealing stage was observed. Hence, the determined activation energy has to be considered as an average of the whole annealing process, including the removal of vacancy-type defects and dislocations. Tab. 5.2 summarizes the activation energies of defect annealing which were deduced in Chap. 4. Literature data are listed for comparison. It is important to mention, that the definition of the rate constant K has to be taken into account when comparing the respective activation energies. JMAK 1 stands for an annealed fraction $f_{\mathrm{A}}(t)$ defined by $1 - \exp\left[-\left(Kt\right)^n\right]$ and JMAK 2 for $f_{\mathrm{A}}(t) = 1 - \exp\left[-Kt^n\right]$.

The values for HPT-Fe are all lying in a similar regime of ca. 0.7 - $0.8\,$eV and compare very well to the literature value of Voronova et al. [70]. The slight differences between the measurement in this work are probably caused by some unknown parameters in the HPT processing.
Regarding the activation energy of the annealing of HPT-Ta, literature data are scarce. A comparison with literature values of the migration energy of vacancies may be interesting, since hardly any recrystallization could be observed. Investigations of vacancy diffusion in Ta by means of high-voltage electron microscopy revealed an activation

Table 5.2: Recrystallization activation energies of HPT samples determined in the present work by means of dilatometry and DSC in comparison to literature values.

Processing	Exp. Method	Analysis	Q [eV]	Reference
Fe				
HPT (Armco 5r)	Dilatometry	Kissinger	0.83 ± 0.03	this work (Fig. 4.11)
HPT (Armco 8r)	Dilatometry	Kissinger	0.69 ± 0.05	this work (Fig. 4.11)
HPT (HP-Fe)	Dilatometry	Kissinger	0.75 ± 0.02	this work (Sec. 4.1.3, [52])
HPT	SEM	rate change calc.	0.93 ± 0.10	Voronova et al. [70]
Ta				
HPT	Dilatometry	Kissinger	1.18 ± 0.02	this work (Fig. 4.19)
Ni				
HPT	Dilatometry	JMAK 1	1.20 ± 0.01	this work (Fig. 4.32, [73])
HPT	Dilatometry	Kissinger	1.20 ± 0.04	this work (Fig. 4.31, [73])
HPT	DSC	Kissinger	0.95	Setman et al. [9]
Cold worked	TEM	JMAK 2	1.22 – 1.30	Detert and Dressler [89]
Cu				
HPT (Cu A)	Dilatometry	Kissinger	0.92 ± 0.07	this work (Fig. 4.39)
HPT (Cu B)	Dilatometry	Kissinger	0.89 ± 0.02	this work (Fig. 4.39)
HPT (Cu D)	Dilatometry	Kissinger	1.02 ± 0.01	this work (Fig. 4.39)
HPT (Cu D)	DSC	Kissinger	1.03 ± 0.02	this work (Fig. 4.41)
HPT	DSC	Kissinger	$0.48 - 0.78$	Setman et al. [9]
HPT	PALS	Göhler-Sachs	1.0 ± 0.1	Čížek et al. [42]
ECAP	DSC	Kissinger	0.80 ± 0.06	Cao et al. [90]
ECAP	FIB	JMAK 1	1.68 ± 0.10	Amouyal et al. [91]
ECAP	microhardness	JMAK 2	0.68	Molodova et al. [92]

enthalpy for vacancy migration of 1.1 ± 0.2 eV [93] and molecular dynamics simulations of point defects in bcc metals with the embedded atom method yielded a value of $Q = 0.96$ eV for monovacancies in Ta [94]. The excellent accordance of our value with these studies suggests the involvement of vacancies in the annealing process.

For HPT-Ni an activation energy of 1.20 eV is determined both by means of non-isothermal JMAK 1 modeling and by means of the Kissinger method. This is somewhat higher than literature values for HPT-Ni determined by DSC (0.95 eV, [9]). Detert and Dressler [89] reported 1.22 - 1.30 eV with an Avrami exponent of 1.38 for cold-worked Ni using the definition of JMAK 2. This corresponds to 0.88 - 0.94 eV according to the definition of JMAK 1, which again is lower than our value. On the other hand, the present value found for Ni nicely fits to that of Cu if the different melting points T_m are taken into consideration. Indeed, scaling the value of 1.2 eV with the ratio factor $T_{\mathrm{m,Ni}}/T_{\mathrm{m,Cu}} = 1.27$ yields a value of 0.94 eV for Cu.

The measured values for Cu are lying in the range from ca. 0.91 eV for Cu A and B up to 1.02 eV for Cu D. DSC measurements on the same sample Cu D yielded a value of 1.03 eV. The reason for the lower values for the sample series A and B can be found in the higher pressure applied during HPT deformation. For Cu the activation energy Q is reported to decrease with increasing HPT pressure [9].
In comparison, the values of Čížek et al. (1.0 eV [42]) for HPT-Cu and Cao et al. (0.8 eV [90]) for ECAP-Cu match our values very well. The results of Setman et al. and Molodova et al. are considerably lower; the authors explain the low values by the increased shear strain, known to decrease the activation energy [9, 92]. A remarkably higher value of 1.68 eV, caused by O and P impurities segregating at grain boundaries, was observed by Amouyal et al. [91].

Grain boundary excess volume

The excess free volume of a grain boundary compared to the perfect lattice – the volume expansion e_{GB} – represents a key parameter for the physics of grain boundaries and is hardly quantifiable directly. Because of the mismatch of the lattice at grain boundaries, the total number of atoms in a polycrystalline single-phase solid occupies more volume than it would be the case if arranged perfectly in a single crystal. Given that no other lattice defects are present, the grain boundary excess volume e_{GB} can be determined from the macroscopic volume change upon grain growth. The grain boundary excess volume is then defined as the fraction of volume change to grain boundary unit area and has the dimension of a length ([$\mathrm{m}^3/\mathrm{m}^2$]). The grain boundary excess volume should not be confused with the grain boundary thickness δ_{GB}, usually of the order of 0.5 - 1 nm [95].

As the dilatometric studies of HPT-Ni have shown, the annealing of HPT-Ni occurs in two stages A and B. In combination with positron annihilation, SEM, and literature data [96, 97], it can be concluded, that in stage A annealing of vacancies and dislocations takes place, whereas stage B is due to the removal of grain boundaries (see Sec. 4.3.1).

Within stage A in HPT-Ni, the mean grain size does not change significantly as was confirmed by the grain size analysis of the SEM micrographs (see Fig. 4.21). Actually, a slight decrease of the grain size in radial direction due to a rearrangement of dislocations could be observed. The stability of grains during stage A is also supported by the fact, that two different micrographs, one in radial direction in the AR state (Fig. 4.22), the other one in axial direction after stage A (Fig. 4.21 b)) reveal virtually the same grain size of 295 nm in tangential direction.
In stage B, however, the defects remaining in the samples are predominantly grain boundaries and the relative length change observed by dilatometry is only caused by

the removal of grain boundaries due to grain growth.

For HPT-Cu the grain boundaries annealing in stage B were found to be relaxed equilibrium grain boundaries as determined by means of differential scanning calorimetry (Sec. 4.4.4). This can be also assumed for Ni, since there are indications for the relaxation of grain boundaries in ECAP-Ni below $400\,\mathrm{K}$ [98].

The advantage, that the two stages, stage A with the annealing of vacancies and dislocations, and stage B the grain growth stage, can clearly be separated, allows the determination of the excess volume e_{GB} of relaxed grain boundaries according to

$$\left.\frac{\Delta\ell}{\ell_0}\right|_{\mathrm{GB}} = e_{\mathrm{GB}}\left(\frac{1}{d_{\mathrm{initial}}} - \frac{1}{d_{\mathrm{final}}}\right) \quad , \tag{5.1}$$

with $\Delta\ell/\ell_{0,\mathrm{GB}}$ the relative length change due to the removal of grain boundaries, and d_{initial} and d_{final} the grain diameter at the beginning and at the end of the grain growth, respectively (cf. Eq. 3.7).

In Sec. 4.3.3 the relative length changes for all dilatometric measurements on HPT-Ni in axial as well as in tangential direction were presented. Concentrating on the axial measurements first, a mean value $\Delta\ell/\ell_{0,\mathrm{axial}}$ of $(1.76 \pm 0.20) \times 10^{-4}$ deduced from 12 single measurements can be denoted. Since no grain growth could be observed in stage A, the grain size of the as-deformed sample in axial direction of $d_{\mathrm{initial}} = 150\,\mathrm{nm}$ (Fig. 4.22) can be used for the grain boundary excess volume analysis. After stage B, spherical grains with a diameter of $d_{\mathrm{final}} = 832\,\mathrm{nm}$ (Fig. 4.21 c)) could be discerned. With these values, a grain boundary excess volume e_{GB} of $32 \pm 5\,\mathrm{pm}$ is determined according to Eq. 5.1.

In tangential direction 3 single dilatometric experiments were performed, yielding a mean length change $\Delta\ell/\ell_{0,\mathrm{tang}}$ of $(0.85 \pm 0.24) \times 10^{-4}$. With the grain size in tangen-

tial direction of $d_{\mathrm{initial}} = 295\,\mathrm{nm}$ (Fig. 4.22) and the same final grain size, an e_{GB} of $39 \pm 12\,\mathrm{pm}$ can be deduced. The fact that rather identical values e_{GB} are deduced for tangential and axial direction shows that the observed length change in the two directions exactly corresponds with the different number of grain boundaries in these directions. This confirms that the observed $\Delta\ell/\ell_0$ in stage B is due to grain boundaries and underlines the accuracy of the determined value of the grain boundary excess volume.

Furthermore it has to be considered whether there is an influence of the linear thermal expansion of a grain boundary, if that differs from that of the bulk. Birringer et al. [99] found the linear thermal expansion coefficient of a grain boundary α_{GB} in nanocrystalline Pd being by a factor of 1.1 higher than α_{cryst} of the crystal. Employing a rule of mixture for the total reversible thermal expansion for the nanocrystal $\alpha_{\mathrm{nc}} = (1-x)\alpha_{\mathrm{cryst}} + x\alpha_{\mathrm{GB}}$ and taking into account that for the present case the grain boundary fraction x is less than $1\,\%$, then for a physical grain boundary width δ of $0.5\,\mathrm{nm}$ and a temperature increase by $170\,\mathrm{K}$ the contribution to the value of e_{GB} is by far less than $1\,\mathrm{pm}$ and thus negligible.

Also the contribution of dislocations in stage B is considered to be negligible due to the following. Assuming a value of an initial dislocation density ρ in the as-prepared state of $3 \times 10^{15}\,\mathrm{m}^{-2}$ as has been reported for HPT deformed Ni [96], such a dislocation density would contribute an amount of $\Delta\ell/\ell_0 = 3.1 \times 10^{-5}$ to the length change value according to Eq. 3.5. This is $18\,\%$ of $\Delta\ell/\ell_{0,\mathrm{axial}}$. However, the value of the dislocation density in SPD deformed Ni is lowered upon annealing up to $470\,\mathrm{K}$ by at least one order of magnitude as, e.g., reported in Ref. [97]. Therefore, annealing of remnant dislocations during the grain growth process likely contributes only a few percent to the value of the grain boundary excess volume.

As summarized in Tab. 5.3, investigations on the grain boundary excess volume e_{GB} were also performed for HPT-Cu and Fe. The relative length change for Cu is the mean

value determined from three axial measurements[1]. In the case of ARMCO- and HP-Fe, $\Delta\ell/\ell_0$ is taken from the high temperature part of the dilatometric difference curve, i.e. from 673 K to 753 K for ARMCO-Fe and 648 K to 753 K for HP-Fe. Assuming, that at these temperatures vacancy-type defects and dislocations have annealed completely, the remaining length change can be attributed to grain boundaries, allowing the determination of e_{GB}. The error for the relative length change is estimated to 0.2×10^{-4} each. However, the calculations for HPT-Fe are based on single dilatometric measurements and the results have therefore to be regarded as preliminary. This is especially the case for HP-Fe, where the measured length change in the high temperature regime is rather small. Thus, in the following only the preliminary value for ARMCO-Fe is considered.

Table 5.3: Grain boundary excess volume e_{GB} according to Eq. 5.1. d_1 and d_2 denote the grain diameters before grain growth and after the recrystallization stage B in the case of Ni and Cu, and from the high temperature part of annealing in the case of Fe ($\Delta d_1 = 4\,\mathrm{nm}$, $\Delta d_2 = 12\,\mathrm{nm}$), $\Delta\ell/\ell_0$ the relative length change due to the removal of grain boundaries. The measuring direction and the number of measurements are quoted.

Calculation of grain boundary excess volume

Material	d_1 [nm]	d_2 [nm]	$\Delta\ell/\ell_0$ [10^{-4}]	e_{GB} [pm]	direction	Nr.
HPT-Ni	150	832	1.76 ± 0.20	32 ± 5	axial	12
HPT-Ni	295	832	0.85 ± 0.24	39 ± 12	tangential	3
HPT-Cu	242	790	0.97 ± 0.10	34 ± 5	axial	3
ARMCO-Fe	214	406	0.73 ± 0.20	33 ± 12	axial	1
HP-Fe	1010	4900	0.40 ± 0.20	(51 ± 26)	axial	1

[1] For calculation of e_{GB} for Cu from $\Delta\ell/\ell_0$ in stage B, it has not been checked as in the case of Ni, that the grain size remains stable in stage A. However, since stage B in Cu starts at 372 K already, it can be assumed, that grain growth in stage A is negligible as in the case of Ni.

Table 5.4: Literature data of grain boundary excess volume e_{GB} determined experimentally and by simulations. The investigated materials and the used methods are quoted.

Literature values determined experimentally

Material	e_{GB} [pm]	Method	Reference
Fe	19	grain growth kinetics	Krill et al. [100]
Ni	160	X-ray diffraction	Kuru et al. [101]
Pd	23[2]	density measurements	Birringer et al. [99]
Au	12	high-resolution TEM	Buckett and Merkle [102]
Au	60[3]	high-resolution TEM	Merkle [103]
Al	64	GB angle measurements	Shvindlerman et al. [104]

Literature values determined by simulation

Ni	39 - 41[4]	molecular dynamic sim.	Zhang and Srolovitz [105]
Ni	28 - 42[5]	molecular static sim.	Olmsted [106]
Fe	72	molecular dynamic sim.	Wolf and Merkle [107]

In the following the data are compared with literature. For the grain boundary volume expansion only few experimental data is available in literature (see Tab. 5.4). For nanocrystalline Fe a value of $e_{GB} = 19\,\text{pm}$ was derived from modeling of experimental data on grain growth kinetics [100], slightly lower than our preliminary result for ARMCO-Fe. From density measurements on nanoycrystalline Pd a value of $e_{GB} = 23\,\text{pm}$ was determined [99]. There have been efforts to determine e_{GB} by means

[2] Deduced from the quoted excess volume per grain boundary atom.
[3] Deduced from Fig. 5 of Ref. [103].
[4] Deduced from Fig. 11 of Ref. [105].
[5] Deduced from Fig. 4 of Ref. [106].

of high-resolution TEM for isolated grain boundaries with distinct orientation. For Au values of $12\,\mathrm{pm}$ [102] and ca. $60\,\mathrm{pm}$ [103] have been specified. Shvindlerman et al. [104] utilizes the change of grain boundary equilibration angle as a function of hydrostatic pressure on tricrystals in Al with a well-prepared orientation relation. This approach relies on thermodynamic grain boundary modeling. A value of $64\,\mathrm{pm}$ was determined. A much higher value of $160\,\mathrm{pm}$, determined from X-ray diffraction of stressed nanocrystalline Ni thin films, has been reported from Kuru et al. [101].
Data sets of the grain boundary excess volume are also available from computer simulations. Although simulation techniques nowadays are quite powerful, the results for the grain boundary excess volume are sensitively dependent of the choice of the interatomic potential [108]. Recently, values of $e_{\mathrm{GB}} = 39$ to $41\,\mathrm{pm}$ [105] have been reported from molecular dynamic simulations on nickel $\Sigma 5$ grain boundaries and of $e_{\mathrm{GB}} = 28$ to $42\,\mathrm{pm}$ [106] for nickel high-angle grain boundaries. The matching of these data with our values of 32 to $39\,\mathrm{pm}$ is remarkable.

It can be concluded that dilatometry represents an excellent method determining the grain boundary volume expansion in a direct and straight-forward manner.

Total free volume and the issue of lattice vacancies

The dilatometric measurements revealed irreversible relative length changes upon annealing for all HPT-deformed samples of Fe, Ta, Ni, and Cu. Positron annihilation as well as electron microscopy imaging have shown that these relative length changes are caused by the annealing of structural free volume defects. An overview of all investigated HPT samples with the total volume reduction $\Delta V/V_{0,\mathrm{tot}}$ was already given in Tab. 5.1. This total free volume can be attributed to the various lattice defects such as vacancies, vacancy agglomerates, dislocations, and grain boundaries in the relaxed and the non-relaxed state. In the following, an estimation of the amount of free volume, localized at these various types of defects, is given for Fe, Ni, and Cu. For Ta this

estimation is omitted since the available grain size data are not as precise as required for that purpose.

Regarding dislocations the free volume can be calculated according to Eq. 3.5. The maximum dislocation density ρ_{disl} introduced by HPT deformation is of the order of $(2-6) \times 10^{15}\,\mathrm{m}^{-2}$ [109, 110]. With these values the maximum possible amount of free volume release due to dislocations $\Delta V/V_{0,\mathrm{disl}}$ can be deduced. Tab. 5.5 summarizes this estimation related to the total free volume release $\Delta V/V_{0,\mathrm{tot}}$.

Table 5.5: Free volume release $\Delta V/V_{0,\mathrm{disl}}$ due to the annealing of dislocations according to Eq. 3.5. $\Delta V/V_{0,\mathrm{tot}}$: total volume reduction deduced from the mean total relative length changes. $F_{\mathrm{GB}} = \frac{\Delta V/V_{0,\mathrm{disl}}}{\Delta V/V_{0,\mathrm{tot}}}$: fraction in per cent. b: magnitude of the Burgers vector (Eq. 3.6). The lower and upper value of $\Delta V/V_{0,\mathrm{disl}}$ corresponds to the lower $(2 \times 10^{15}\,\mathrm{m}^{-2})$ and upper value $(6 \times 10^{15}\,\mathrm{m}^{-2})$ of the dislocation density [109, 110].

Estimation of free volume at dislocations

Material	b [pm]	$\Delta V/V_{0,\mathrm{disl}}$ [10^{-4}]	$\Delta V/V_{0,\mathrm{tot}}$ [10^{-4}]	F_{disl} [%]
ARMCO-Fe	248.3	0.6 - 1.9	20 - 30	2 - 9
HP-Fe	248.3	0.6 - 1.9	30	2 - 6
Ni	249.2	0.6 - 1.9	14	4 - 13
Cu A,B	255.6	0.7 - 2.0	12	6 - 16
Cu C,D	255.6	0.7 - 2.0	20	4 - 10

Grain growth to various degrees could be observed for all HPT samples upon annealing (see SEM, Fig. 4.2, 4.21, 4.34). The free volume release due to the removal of relaxed grain boundaries can be estimated using the determined values for the grain boundary excess volume e_{GB} (see above) as well as the grain sizes d_1 and d_2. This consideration takes into account not only the recrystallization in stage B, but the entire grain growth

process including the low temperature grain growth in the case of Fe and stage C in the case of Ni and Cu. Therefore, d_1 and d_2 denote the grain sizes in the as-prepared state and at the maximum annealing temperature, respectively.

Tab. 5.6 exhibits the resulting $\Delta V/V_{0,\mathrm{GB}}$ as a percentage of the total volume release $\Delta V/V_{0,\mathrm{tot}}$. Since the final grain size d_2 has only little influence on the total volume release, for Cu and Ni the values of $(\Delta V/V_{0,\mathrm{tot}}) \times 1/3$ is rather similar to the relative length change $\Delta\ell/\ell_0$ shown in Tab. 5.3.

Table 5.6: Free volume release $\Delta V/V_{0,\mathrm{GB}}$ due to the removal of grain boundaries according to Eq. 5.1. e_{GB}: grain boundary excess volume according to Tab. 5.3. d_1, d_2: grain diameters in the as-prepared state and after annealing at the maximum temperature, respectively. (For the exact temperature values see SEM micrographs of the corresponding material.) $\Delta V/V_{0,\mathrm{tot}}$: total volume reduction taken from the mean total relative length changes. $F = \frac{\Delta V/V_{0,\mathrm{GB}}}{\Delta V/V_{0,\mathrm{tot}}}$: fraction in per cent.

Estimation of free volume at grain boundaries

Material	e_{GB} [pm]	d_1 [nm]	d_2 [nm]	$\Delta V/V_{0,\mathrm{GB}}$ $[10^{-4}]$	$\Delta V/V_{0,\mathrm{tot}}$ $[10^{-4}]$	F_{GB} [%]
ARMCO-Fe	33	144	406	4.4	20 - 30	15 - 22
HP-Fe	33	320	4900	2.9	30	10
Ni	36	150	3400	6.9	14	49
Cu A,B	34	242	1540	3.6	12	30
Cu C,D	34	257	7733	3.8	20	19

Tab. 5.7 shows the free volume release $F_{\mathrm{res}} = 100 - F_{\mathrm{disl}} - F_{\mathrm{GB}}$, which neither can be attributed to dislocations nor to relaxed grain boundaries. This remaining free volume release has therefore to be attributed to vacancies, vacancy agglomerates, or excess volume associated with unrelaxed grain boundaries.

Table 5.7: Percentage of free volume release $F_{\mathrm{res}} = 100 - F_{\mathrm{disl}} - F_{\mathrm{GB}}$, which neither can be attributed to dislocations nor to relaxed grain boundaries.

Estimation of residual free volume

Material	F_{disl} [%]	F_{GB} [%]	F_{res} [%]
ARMCO-Fe	2 - 9	15 - 22	69 - 83
HP-Fe	2 - 6	10	84 - 88
Ni	4 - 12	49	39 - 47
Cu A,B	6 - 16	30	54 - 64
Cu C,D	4 - 10	19	71 - 77

This estimation shows that generally a minor part of free volume is localized at dislocations. $\Delta V/V_{0,\mathrm{disl}}$ amounts to a maximum of $16\,\%$ of $\Delta V/V_{0,\mathrm{tot}}$ in the case of Cu. Regarding the possible amount of free volume localized at grain boundaries very different results due to the different initial grain sizes were obtained. In any case, a high percentage for the residual free volume was revealed.

In detail, F_{res} amounts to more than $80\,\%$ for Fe of both purities. This result has to be regarded as a rough estimate, since the grain boundary excess volume e_{GB} for Fe of $33\,\mathrm{pm}$ is a preliminary value. With a higher value of $e_{\mathrm{GB}} = 72\,\mathrm{pm}$, deduced from molecular dynamics simulations [107], a still high percentage for F_{res} of 59 and $73\,\%$ for ARMCO-Fe and HP-Fe is obtained, respectively. This high amount of additional excess free volume indicates a high concentration of vacancy-type defects in addition to relaxed grain boundaries and dislocations.

For Ni the residual free volume amounts to ca. $43\,\%$. This corresponds to a volume change of $\Delta V/V_0$ of 6×10^{-4} mainly occuring during stage A. Assuming that this $\Delta V/V_0$ can be attributed to vacancies totally, a vacancy concentration of 7.5×10^{-4} can be estimated, taking into account a relaxed vacancy volume of $0.8\,\Omega$, where Ω denotes the

atomic volume [111]. (A detailed explanation of the vacancy relaxation is given in the section *anisotropy*.) This attribution to vacancies is supported by dilatometric measurements on the same Ni samples after pre-annealing at $353\,\mathrm{K}$ where vacancies are becoming mobile according to literature [112]. In fact, $\Delta\ell/\ell_0$ in stage A is strongly reduced after pre-annealing [73]. This evidence of high vacancy concentrations exceeding 10^{-4} nicely fits to earlier results obtained for HPT-Ni by Setman et al. by means of DSC and RER [8].

However, the relaxation of non-equilibrium grain boundaries in this temperature of stage A has to be taken into consideration as another source of free-volume release. This is directly concluded from enhanced diffusivities observed in metals after SPD processing [19, 113]. These enhanced diffusivities decrease towards values typical of conventional grain boundaries at slightly elevated temperatures, indicating a structural relaxation due to the annealing of excess free volume. For ECAP-Ni the relaxation of grain boundaries is reported to take place below $400\,\mathrm{K}$ [98], i.e., in the regime of stage A.

Regarding Cu, the high residual free volume value is somewhat surprising, particularly since the annealing stage of monovacancies in Cu is located around $250\,\mathrm{K}$ [112] and monovacancies probably are not present at room temperature anymore. The origin for the high value of F_{res} can be mainly found in the strong length shrinkage in stage C, which in most measurements is notably larger than $\Delta\ell/\ell_0$ of the recrystallization stage B. Non-equilibrium grain boundaries as possible source for excess free volume can be safely ruled out, since there are indications of diffusion experiments that the relaxation of such grain boundaries in Cu already occurs at room temperature [114].

Stage C might partly arise from microvoids, being stable up to temperatures beyond $450\,\mathrm{K}$. This is supported by Čížek et al. [42], who observed the annealing of voids with a volume of 5 to 8 monovacancies and a concentration of the order of 10^{-6} in HPT-Cu at temperatures in the regime of stage C. For ECAP-Ti, Lapovok et al. [115] identified voids of 10 to $200\,\mathrm{nm}$ size with a volume fraction in the range of some 10^{-5} by means

of small-angle neutron scattering. In both of these studies, however, the volume fraction of voids is notably smaller than the observed free volume release in stage C in this work.

The yet unsolved question of anisotropy

One novel question emerging from this work and still being unresolved pertains to the strong anisotropic annealing behaviour as revealed by dilatometry for Ni and HP-Fe in axial and tangential direction (cf. Sec. 4.1.4, 4.3.2). Whereas in the case of axial samples an irreversible shrinkage occurred, tangential samples showed an elongation in the lower temperature part of the annealing (stage A in the case of Ni).
A possible explanation for this issue can be found in the strong anisotropic microstructure in the case of HPT-Ni. Elongated grains in tangential direction could be observed. As discussed in the following, the anisotropic length change might be associated with the anisotropic annealing of vacancies.

Fig. 5.1 illustrates the different arrangement of elongated grains in dilatometric samples prepared in axial or tangential direction from the HPT disc (cf. Fig. 3.8). It can be assumed, that vacancies preferentially anneal out in the plane perpendicular to the elongation axis of the grains, owing to the smaller diffusion length compared to the direction of elongation.
If the volume of a vacancy equals the atomic volume, the preferential annealing perpendicular to the elongation axis will cause *no* length change in the direction of elongation. On the other hand, anisotropic annealing of *relaxed* vacancies gives rise to an increase of length along the elongation axis due to the expansion of the lattice when relaxed vacancies are replaced by atoms. This will be considered in the following quantitatively.

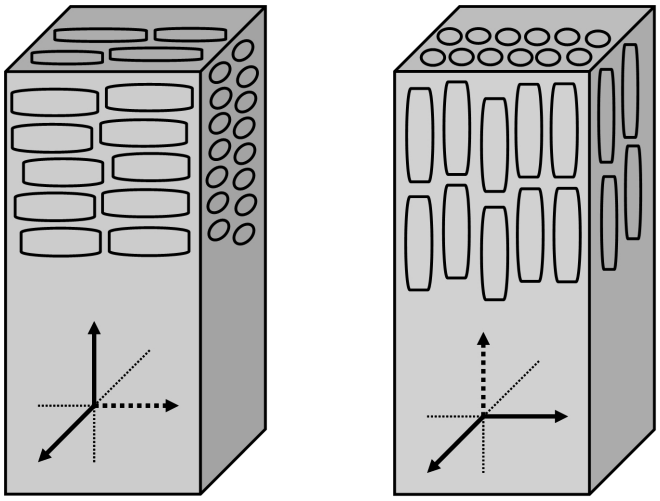

(a) axial (b) tangential

Figure 5.1: Illustration of anisotropic annealing of vacancies in dilatometric HPT samples in (a) axial and (b) tangential measuring direction (see Fig. 3.8 for orientation). The solid arrows indicate the preferential direction of annealing perpendicular to the elongated grain axis (dashed arrow).

The volume V_v of a relaxed lattice vacancy is reduced compared to the atomic volume Ω by:

$$V_\mathrm{v} = (1 - r) \cdot \Omega \tag{5.2}$$

with the relaxation factor

$$r = \frac{\Omega - V_\mathrm{v}}{\Omega} = 1 - \frac{V_\mathrm{v}}{\Omega} \quad . \tag{5.3}$$

When relaxed vacancies anisotropically anneal out, the relative length increase in tangential measuring direction, i.e., parallel to the axis of elongation (Fig. 5.1 b)) is given by:

$$\left.\frac{\Delta\ell}{\ell_0}\right|_\mathrm{tang.} = +\frac{1}{3} C_\mathrm{v} r \tag{5.4}$$

with the vacancy concentration C_v. When the plane of preferential vacancy annealing lies parallel to the measuring direction (axial direction, Fig. 5.1 a)), the relative length change is given by the same elongation due to the lattice expansion, less the shrinkage due to the annealing of the relaxed vacancies:

$$\left.\frac{\Delta\ell}{\ell_0}\right|_\mathrm{axial} = +\frac{1}{3} C_\mathrm{v} r - \frac{1}{2} C_\mathrm{v} (1 - r) \tag{5.5}$$

The factor $1/2$ is due to the annealing of the vacancies in two directions, namely axial and radial. Calculating the ratio M of the tangential and axial relative length change, the vacancy concentration C_v cancels out, which yields:

$$M := \frac{\Delta\ell/\ell_0|_\mathrm{tang.}}{\Delta\ell/\ell_0|_\mathrm{axial}} = \frac{\frac{1}{3} r}{-\frac{1}{2}(1 - r) + \frac{1}{3} r} = \frac{2r}{5r - 3} \tag{5.6}$$

From Eq. 5.6 the relaxation factor

$$r = \frac{3M}{5M - 2} \tag{5.7}$$

can be deduced. We note that in the framework of anisotropic vacancy annealing, the relaxation factor can be directly determined form the ratio M of the length change in both directions.

For HPT-Ni, two series of orientation-dependent measurements on sample sets prepared from two different HPT discs were performed. The ratios of the tangential and axial relative length change for the two series amount to $M_1 = -0.33$ and $M_2 = -0.41$ (cf. Tab. 4.7 and 4.8). According to Eq. 5.7 a value for r of 0.27 and 0.30, respectively, is obtained, which corresponds to a vacancy volume of $0.73\,\Omega$ and $0.70\,\Omega$, respectively.

A literature value for the vacancy volume in Ni amounts to $V_\mathrm{v} = 0.8\,\Omega$, determined by means of diffuse X-ray scattering [111]. Scholz and Seeger [116] calculated a value of $0.7\,\Omega$ for the vacancy relaxation in germanium. From the inward relaxation reported by Khanna et al. [117] for molybdenum a value of $0.8\,\Omega$ can be estimated. These values are in good accordance with our findings.

It can therefore be concluded, that this vacancy relaxation model is capable of explaining the anisotropic annealing behaviour of HPT-Ni completely. Furthermore, it is strongly supported by evidences for high vacancy concentrations in HPT-Ni as shown in this work as well as by e.g. Setman et al. [9].
However, the model is only of relevance in materials with anisotropic grain structure as prerequisite for anisotropic annealing of vacancies. Even stronger elongation of HPT samples in tangential direction was observed for high-purity Fe. Since the vacancy relaxation in Fe is not very pronounced ($0.95\,\Omega$ [111]) and furthermore the SEM

micrographs of HP-Fe reveal a rather spherical grain structure, the vacancy relaxation model can not be employed here. For the moment, the question of anisotropic annealing behaviour in Fe remains therefore unsolved.

For the issue of anisotropy, HPT-Ni was also investigated regarding macrostresses, performed by means of XRD measurements. First preliminary investigations revealed no macrostresses in neither of the two directions axial and tangential [118]. However, more detailed studies of macrostress will be necessary in order to unambiguously attribute the observed anisotropic length change in Ni to the anisotropic vacancy annealing. Nevertheless, a new possibility to study vacancy relaxation by means of dilatometry might be offered.

6 Summary & Conclusion

With the aim to study free volume type defects in SPD processed metals, samples of Fe, Ta, Ni and Cu were deformed by means of HPT and investigated by high-precision difference dilatometry and positron annihilation spectroscopy.

For all samples high absolute concentrations of excess free volume could be directly determined by dilatometry. The values for the total volume change $\Delta V/V_{0,\mathrm{total}}$ are ranging from 1×10^{-3} to 3×10^{-3} depending on the material. Estimations of the amount of free volume localized at dislocations and relaxed grain boundaries revealed high percentages of residual free volume, which may arise from vacancy-type defects (monovacancies and agglomerates) as well as from non-equilibrium grain boundaries.

The different annealing behaviour of bcc and fcc metals as observed by dilatometry has to be pointed out. Whereas Fe and Ta exhibited one broad annealing stage, in the case of Ni and Cu distinct sub-stages A, B and C were observed which were further stud-

ied by positron annihilation and electron microscopy. Comparative measurements on HPT-Cu by differential scanning calorimetry and residual electrical resistivity experiments supported the annealing behaviour as determined by dilatometry.

By means of scanning electron microscopy, the sub-stages observed by dilatometry could be attributed to specific defects. In particular, the length change in stage B could be identified with the removal of grain boundaries in the wake of recrystallization for both fcc metals Ni and Cu. This offered the possibility to reveal the fundamental parameter of the grain boundary excess volume, using the initial and final grain sizes as well as the relative length change in this stage. The values for the grain boundary excess volume e_{GB} yielded 36 ± 9 and 34 ± 5 for Ni and Cu, respectively. The value for Ni can be considered as statistically reliable, since it was determined from a variety of samples oriented in two different directions.

By variation of the dilatometric heating rate, the analysis of defect annealing kinetics was possible. For HPT-Fe an activation energy Q for the broad annealing stage of about 0.76 eV could be determined, which compares well to literature data. The value for Ta of $Q = 1.18$ eV is in good accordance with literature values for monovacancy migration. This indicates, that vacancies are involved in the annealing process of HPT-Ta. The recrystallization kinetics of HPT-Ni were analyzed by means of non-isothermal Johnson-Mehl-Avrami-Kolmogorov modeling as well as with the method of Kissinger, yielding the same activation energy of 1.20 eV. This value nicely scales with that of Cu taking into account the different melting temperatures of Ni and Cu. The values of Q for HPT-Cu, determined by the Kissinger method, are in the range of 0.89 - 1.02 eV. DSC measurements revealed $Q = 1.03$ eV. This activation energy found for HPT-Cu is in good agreement with literature data.

Positron annihilation turned out to be complement to dilatometry in an ideal manner. The Doppler-broadening experiments at the positron beam of the FRMII clearly identified the annealing of atomic free volume defects. The S-parameter change showed

very similar annealing characteristics, i.e. one stage in the case of Fe and sub-stages in the case of Ni and Cu, as revealed in the dilatometric measurements. The shift of the S-parameter curve compared to the dilatometric length change towards higher temperatures could be understood in the framework of diffusion-limited trapping at grain boundaries. By means of positron lifetime spectroscopy, free volume type defects, such as vacancies and dislocations, could be identified.

An interesting issue emerging in the wake of this thesis pertains to the different annealing behaviour for different orientated samples observed for Ni and HP-Fe. Whereas the axial samples exhibit a continuous length shrinkage upon annealing, the tangential samples partially increase in length. In the case of Ni the elongation takes place in stage A. Preliminary XRD measurements did not reveal an indication of macrostresses which might cause the anisotropy. On the other hand, the anisotropy of the length change could be quantitatively analyzed within a model of anisotropic annealing of relaxed vacancies associated with the shape anisotropy of the oriented crystallites. However, the model can not be applied for Fe, where a rather spherical grain structure does not support anisotropic vacancy annealing. In order to clarify this issue, further measurements of both, dilatometry and XRD macrostress analysis are required.

In conclusion, high-precision difference dilatometry has proven capable of the comprehensive analysis of atomic free volume in bulk nanocrystalline metals. Structural defects such as vacancies, dislocation and grain boundaries and the corresponding absolute concentration of free volume could be discerned according to their individual annealing stage. In addition, the associated thermally activated annealing process was studied by applying different heating rates, yielding defect annealing and recrystallization activation energies. Furthermore, the grain boundary excess volume, a fundamental parameter directly related to the grain boundary energy, could be determined making use of SEM grain size data. Finally, the combination of dilatometry with positron annihilation spectroscopy brought a more profound understanding of the complex atomic defect structure of bulk nanocrystalline metals.

BIBLIOGRAPHY

[1] C. C. Koch, Nanostructured Materials: Processing, Properties and Applications, 2nd ed., William Andrew Publishing, New York, 2007.

[2] R. Z. Valiev, R. K. Islamgaliev and I. V. Alexandrov, Bulk nanostructured materials from severe plastic deformation, *Prog. Mater. Sci.* **45** (2000) 103–189.

[3] M. J. Zehetbauer and R. Valiev (eds.), Nanomaterials by severe plastic deformation, Wiley-VCH, Weinheim, 2004.

[4] M. Furukawa, Z. Horita, M. Nemoto and T. G. Langdon, The use of severe plastic deformation for microstructural control, *Mater. Sci. Eng. A* **324** (2002) 82–89.

[5] R. Pippan, F. Wetscher, M. Hafok, A. Vorhauer and I. Sabirov, The limits of refinement by severe plastic deformation, *Adv. Eng. Mater.* **8** (2006) 1046–1056.

[6] A. Seeger and G. Schottky, Die Energie und der elektrische Widerstand von Grosswinkelkorngrenzen in Metallen, *Acta. Metall.* **7** (1959) 495–503.

[7] H. Mehrer, Diffusion in solids, Springer, Berlin, 2007.

[8] D. Setman, E. Schafler, E. Korznikova and M. J. Zehetbauer, The presence and nature of vacancy type defects in nanometals detained by severe plastic deformation, *Mater. Sci. Eng. A* **493** (2008) 166–122.

[9] D. Setman, M. B. Kerber, E. Schafler and M. J. Zehetbauer, Activation enthalpies of deformation-induced lattice effects in severe plastic deformation nanometals

measured by differential scanning calorimetry, *Metall. Mater. Trans. A* **41** (2010) 810–815.

[10] R. Pippan, S. Scheriau, A. Hohenwarter and M. Hafok, Advantages and limitations of HPT: a review, *Mater. Sci. Forum* **584-586** (2008) 16–21.

[11] A. Vorhauer and R. Pippan, On the homogeneity of deformation by high pressure torsion, *Scripta Mater.* **51** (2004) 921–925.

[12] X. Sauvage, F. Wetscher and P. Pareige, Mechanical alloying of Cu and Fe induced by severe plastic deformation of a Cu-Fe composite, *Acta Mater.* **53** (2005) 2127–2135.

[13] X. Sauvage and R. Pippan, Nanoscaled structure of a Cu-Fe composite processed by high-pressure torsion, *Mater. Sci. Eng. A* **410-411** (2005) 345–347.

[14] A. A. Mazilkin, B. B. Straumal, E. Rabkin, B. Baretzky, S. Enders, S. G. Protasova, O. A. Kogtenkova and R. Z. Valiev, Softening of nanostructured Al-Zn and Al-Mg alloys after severe plastic deformation, *Acta Mater.* **54** (2003) 3933–3939.

[15] E. Schafler, G. Steiner, E. Korznikova, M. Kerber and M. Zehetbauer, Lattice defect investigation of ECAP-Cu by means of X-ray line profile analysis, calorimetry and electrical resistometry, *Mater. Sci. Eng. A* **410-411** (2005) 169–173.

[16] M. J. Zehetbauer, E. Schafler and T. Ungár, Vacancies in plastically deformed copper, *Z. Metallk.* **96** (2005) 1044–1048.

[17] U. Essmann, U. Gösele and H. Mughrabi, A model of extrusions and intrusions in fatigued metals. (I) Point-defect production and the growth of extrusion, *Phil. Mag. A* **44** (1981) 405–426.

[18] H. Tanimoto, P. Farber, R. Würschum, R. Z. Valiev and H.-E. Schaefer, Self-diffusion in high-density nanocrystalline Fe, *Nanostruct. Mater.* **12** (1999) 681–684.

[19] R. Würschum, S. Herth and U. Brossmann, Diffusion in nanocrystalline metals and alloys – a status report, *Adv. Eng. Mater.* **5** (2003) 365–372.

[20] Y. R. Kolobov, G. P. Grabovetskaya, M. B. Ivanov, A. P. Zhilyaev and R. Z. Valiev, Grain boundary diffusion characteristics of nanostructured nickel, *Scripta Mater.* **44** (2001) 873–878.

[21] R. Z. Valiev, I. M. Razumovskii and V. I. Sergeev, Diffusion along grain boundaries with non-equilibrium structure, *phys. stat. sol. (a)* **139** (1993) 321–335.

[22] Y. Amouyal, S. V. Divinski, Y. Estrin and E. Rabkin, Short-circuit diffusion in an ultrafine-grained copper-zirconium alloy produced by equal channel angular pressing, *Acta Mat.* **55** (2007) 5968–5979.

[23] R. O. Simmons and R. W. Balluffi, Measurements of Equilibrium Vacancy Concentrations in Aluminum, *Phys. Rev.* **117** (1960) 52–61.

[24] R. O. Simmons and R. W. Balluffi, Measurement of Equilibrium Concentrations of Vacancies in Aluminum, *Phys. Rev.* **119** (1960) 600–605.

[25] R. O. Simmons and R. W. Balluffi, Measurement of Equilibrium Concentrations of Vacancies in Gold, *Phys. Rev.* **125** (1962) 862–872.

[26] R. O. Simmons and R. W. Balluffi, Measurement of Equilibrium Concentrations of Vacancies in Copper, *Phys. Rev.* **129** (1963) 1533–1544.

[27] R. Feder and A.S. Nowick, Use of Thermal Expansion Measurements to Detect Lattice Vacancies near the Melting Point of Pure Lead and Aluminum, *Phys. Rev.* **109** (1958) 1959–1963.

[28] H.-E. Schaefer, K. Frenner and R. Würschum, Time-differential length change measurements for thermal defect investigations: Intermetallic B2-FeAl and B2-NiAl compounds, a case study, *Phys. Rev. Lett.* **82** (1999) 948–951.

[29] F. Ye, W. Sprengel, R. K. Wunderlich, H.-J. Fecht and H.-E. Schaefer, Reversible atomic processes as basic mechanism of the glass transition, *Proc. Natl. Acad. Sci.* **104** (2007) 12962–12965.

[30] B. Oberdorfer, B. Lorenzoni, K. Unger, W. Sprengel, M. Zehetbauer, R. Pippan and R. Würschum, Absolute concentration of free volume-type defects in ultrafine-grained Fe prepared by high-pressure torsion, *Scripta Mater.* **63** (2010) 452–455.

[31] E.-M. Steyskal, B. Oberdorfer, W. Sprengel, M. Zehetbauer, R. Pippan and R. Würschum, Direct experimental determination of grain boundary excess volume in metals, *Phys. Rev. Lett.* (2011) in press.

[32] B. Oberdorfer, E.-M. Steyskal, W. Sprengel, R. Pippan, M. Zehetbauer, W. Puff and R. Würschum, Recrystallization kinetics of ultrafine-grained Ni studied by dilatometry, *J. Alloys Comp.* **509S** (2011) S309–S311.

[33] H.-E. Schaefer, R. Würschum, R. Birringer and H. Gleiter, Structure of nanometer-sized polycrystalline iron investigated by positron lifetime spectroscopy, *Phys. Rev. B* **38** (1988) 9545–9554.

[34] R. Würschum, K. Reimann, S. Gruß, A. Kübler, P. Scharwaechter, W. Frank, O. Kruse, H. D. Carstanjen and H.-E. Schaefer, Structure and diffusional properties of nanocrystalline Pd, *Phil. Mag. B* **76** (1997) 401–417.

[35] R. Würschum, A. Kübler, S. Gruß, P. Scharwaechter, W. Frank, R. Z. Valiev, R. R. Mulyukov and H.-E. Schaefer, Tracer diffusion and crystallite growth in ultrafine grained Pd prepared by severe plastic deformation, *Annales de Chimie - Science des Matériaux* **21** (1996) 471–482.

[36] E. Shapiro, R. Würschum, H.-E. Schaefer, H. Ehrhardt, C. E. Krill and R. Birringer, Structural stability and high-temperature positron lifetime study of mechanically alloyed nanocrystalline Pd-Zr, *Mater. Sci. Forum* **343-346** (2000) 726–731.

[37] R. Würschum, P. Farber, R. Dittmar, P. Scharwaechter, W. Frank and H.-E. Schaefer, Thermal vacancy formation and self-diffusion in intermetallic Fe_3Si-crystallites of nanocomposite alloys, *Phys. Rev. Lett.* **79** (1997) 4918–4921.

[38] W. Puff, H. Rabitsch, G. Wilde, G. P. Dinda and R. Würschum, Chemical sensitive free volume study of amorphization of $Cu_{60}Zr_{40}$ induced by cold rolling and folding, *J. Appl. Phys.* **101** (2007) 123512/1–123512/9.

[39] W. Lechner, W. Puff, B. Mingler, M. J. Zehetbauer and R. Würschum, Microstructure and vacancy-type defects in high-pressure torsion deformed Al-Cu-Mg-Mn alloy, *Scripta Mater.* **61** (2009) 383–386.

[40] R. Würschum and A. Seeger, Diffusion-reaction model for the trapping of positrons in grain boundaries, *Phil. Mag. A* **73** (1996) 1489–1501.

[41] B. Oberdorfer and R. Würschum, Positron trapping model for point defects and grain boundaries in polycrystalline materials, *Phys. Rev. B* **79** (2009) 184103/1–184103/7.

[42] J. Čížek, I. Prohazka, M. Cieslar, R. Kuzel, J. Kuriplach, F. Chmelik, I. Stulikova, F. Becvar, O. Melikhova and R. K. Islamgaliev, Thermal Stability of ultrafine grained copper, *Phys. Rev. B* **65** (2002) 094106/1–16.

[43] J. Čížek, I. Prohazka, M. Cieslar, I. Stulikova, F. Chmelik and R. K. Islamgaliev, Positron-Lifetime Investigation of Thermal Stability of Ultra-Fine Grained Nickel, *Phys. Stat. Sol.* **191** (2002) 391–408.

[44] S. Van Petegem, F. Dalla Torre, D. Segers and H. van Swygenhoven, Free volume in nanostructured Ni, *Scripta Mater.* **48** (2003) 17–22.

[45] R. Krause-Rehberg, V. Bondarenko, E. Thiele, R. Klemm and N. Schell, Determination of absolute defect concentrations for saturation trapping of positrons - deformed polycrystalline Ni as a case study, *Nucl. Instr. Meth. Phys. Res. B* **240** (2005) 719–725.

[46] B. Oberdorfer, E.-M. Steyskal, W. Sprengel, W. Puff, P. Pikart, C. Hugenschmidt, M. Zehetbauer, R. Pippan and R. Würschum, *In situ* probing of fast defect annealing in Cu and Ni with a high-intensity positron beam, *Phys. Rev. Lett.* **105** (2010) 146101(1)–146101(4).

[47] A. Vorhauer and R. Pippan, On the Onset of a Steady State in Body-Centered Cubic Iron during Severe Plastic Deformation at Low Homologous Temperatures, *Metall. Mater. Trans. A* **39A** (2008) 417–429.

[48] M. Hafok and R. Pippan, Comparison of single crystalline and polycrystalline behavior under high pressure torsion, *Mater. Sci. Forum* **550** (2007) 277–282.

[49] A. Hohenwarter, A. Bachmaier, B. Gludovatz, St. Scheriau and R. Pippan, Technical parameters affecting grain refinemnet by high pressure torsion, *Int. J. Mat. Res.* **100** (2009) 1653–1661.

[50] R. Würschum, B. Oberdorfer, E.-M. Steyskal, W. Sprengel, W. Puff, P. Pikart, C. Hugenschmidt and R. Pippan, Free volumes in bulk nanocrystalline metals studied by the complementary techniques of positron annihilation and dilatometry, *Physica B* accepted: Jan 11, 2012.

[51] J. Hirth and J. Lothe, Theory of dislocations, John Wiley, New York, 1982.

[52] B. R. Scherwitzl, Dilatometrische Untersuchung freier Volumen in submikrokristallinem Eisen nach Hochverformung, Master thesis, Graz University of Technology, Austria, 2012.

[53] K. Unger, Bestimmung der Curie-Temperatur von Nickel zur heizratenunabhängigen Temperaturkalibrierung eines Differenz-Dilatometers, Bachelor thesis, Institute of Materials Physics, Graz University of Technology, Austria, 2010.

[54] G. Mohapatra, F. Sommer and E.J. Mittemeijer, Calibration of a quenching and deformation differential dilatometer upon heating and cooling: Thermal expansion of Fe and Fe-Ni alloys, *Thermochimica Acta* **453** (2007) 31–41.

[55] M. Yousuf, P. C. Sahu, H. K. Jajoo, S. Rajagopalan and K. G. Rajan, Effect of Magnetic Transition on the Lattice Expansion of Nickel, *J. Phys. F: Met. Phys.* **16** (1986) 373–380.

[56] P. K. Gallagher, Zhi min Zhong, E. L. Charsley, S. A. Mikhail, M. Todoki, K. Taniguahi and R. L. Blaine, A study of the effect of purity on the use of nickel as a temperature standard for thermomagnetometry, *J. Therm. Anal.* **40** (1993) 1423–1430.

[57] H. E. Kissinger, Variation of peak temperature with heating rate in differential thermal analysis, *J. Res. Nat. Bur. Stand.* **57** (1956) 217–221.

[58] W. Puff, PFPOSFIT: A new version of a program for analysing positron lifetime spectra with non-Gaussian prompt curve, *Comp. Phys. Commun.* **30** (1983) 359–368.

[59] C. Hugenschmidt, B. Löwe, J. Mayer, C. Piochacz, P. Pikart, R. Repper, M. Stadlbauer and K. Schreckenbach, Unprecedented intensity of a low-energy positron beam, *Nucl. Instr. Methods A* **593** (2008) 614–619.

[60] S. Dannefaer, V. Avalos, D. Kerr, R. Poirier, V. Shmarovoz and S. H. Zhang, Annealing of electron-, proton-, and ion-produced vacancies in Si, *Phys. Rev. B* **73** (2006) 115202/1–115202/14.

[61] J. Ohser and F. Mücklich, Statistical analysis of microstructures in materials science, 1 ed., John Wiley, New York, 2000.

[62] M. D. Abramoff, P. J. Magalhaes and S. J. Ram, Image processing with ImageJ, *Biophotonics Int.* **11** (2004) 36–42.

[63] W. F. Hosford, Materials Science, Cambridge University Press, 2007.

[64] J. Ohser, Quantitative Gefügeanalyse, Metallographie (H. Schumann and H. Oettel, eds.), Wiley VHC, 2004, pp. 250–284.

[65] A. Vehanen, P. Hautojärvi, J. Johansson, J. Yli-Kauppila and P. Moser, Vacancies and carbon impurities in α-iron: electron irradiation, *Phys. Rev. B* **25** (1982) 762–780.

[66] F. Wetscher, A. Vorhauer and R. Pippan, Strain hardening during high pressure torsion deformation, *Mater. Sci. Eng. A* **410-411** (2005) 213–216.

[67] P. Hautojärvi, A. Vehanen and V. S. Mikhalenkov, Recovery of deformed iron studied by positrons, *Appl. Phys.* **11** (1976) 191–192.

[68] E. Kuramoto, F. Hori, M. Ohmura and M. Takenaka, Positron lifetime study of low temperature neutron-irradiated Fe and Ni, *Mater. Sci. Forum* **363-365** (2001) 159–162.

[69] H.-E. Schaefer, Gitterlücken und Positronenzerstrahlung in Metallen, Habilitation thesis, Stuttgart University, Germany, 1981.

[70] L. M. Voronova, M. V. Degtyarev and T. I. Chashchukhina, Recrystallization of the ultradispersed structure of pure iron formed at different stages of the deformation-induced strain hardening, *Phys. Met. Metall.* **104** (2007) 262–273.

[71] H.-E. Schaefer, P. Valenta, B. Saile and K. Maier, Positron annihilation in electron irradiated refractory metals, Positron Annihilation 5 (R. R. Hasiguti and K. Fujiwara, eds.), Japan Institute of Metals, Sendai, 1979, p. 747.

[72] P. Hautojärvi, H. Huomo, M. Puska and A. Vehanen, Vacancy recovery and vacancy-hydrogen interaction in niobium and tantalum studied by positrons, *Phys. Rev. B* **32** (1985) 4326–4331.

[73] E.-M. Steyskal, Untersuchung freier Volumen in submikrokristallinem Nickel mit der Methode der Dilatometrie, Master thesis, Graz University of Technology, Austria, 2010.

[74] M. Hafok, A. Vorhauer, J. Keckes and R. Pippan, HPT deformation of copper and nickel single crystals, *Mater. Sci. Forum* **503-504** (2006) 621–626.

[75] M. Hafok and R. Pippan, High-pressure torsion applied to nickel single crystals, *Phil. Mag.* **88** (2008) 1857–1877.

[76] B. Barbiellini, M. J. Puska, T. Korhonen, A. Harju, T. Torsti and R. M. Nieminen, Calculation of positron states and annihilation in solids: A density-gradient-correction scheme, *Phys. Rev. B* **53** (1996) 16201–16213.

[77] J. C. Robles, E. Ogando and F. Plazaola, Positron lifetime calculation for the elements of the periodic table, *J. Phys. Condens. Matter* **19** (2007) 176222.

[78] B. Eigenmann and E. Macherauch, Röntgenographische Untersuchung von Spannungszuständen in Werkstoffen. Teil II., *Materialwiss. Werkstofftech.* **26** (1995) 199–216.

[79] J. Keckes, E. Eiper, K. J. Martinschitz, P. Boesecke, W. Gindl and G. Dehm, In-situ X-ray diffraction as a tool to probe mechanical phenomena down to the nano-scale, *Adv. Eng. Mater.* **8** (2006) 1084–1088.

[80] W. A. Johnson and R. Mehl, Reaction kinetics in processes of nucleation and growth, *T. Am. I. Min. Met. Eng.* **135** (1939) 416–442.

[81] M. Avrami, Kinetics of phase change 1 - general theory, *J. Chem. Phys.* **7** (1939) 1103–1113.

[82] A.N. Kolmogorov, On the statistical theory of metal crystallisation, *Izv. Acad Nauk SSSR, Ser Fiz.* **3** (1939) 355–359.

[83] D.W. Henderson, Thermal analysis of non-isothermal crystallization kinetics in glass forming liquids, *J. Non-Cryst. Solids* **30** (1979) 301–315.

[84] E. Louis and C. Garcia-Cordovilla, On the determination of kinetic parameters through the peak temperature method for differential scanning calorimetry, *J. Therm. Anal.* **29** (1984) 1139–1150.

[85] R. H. Howell, A positron-lifetime study of irradiation effects in copper irradiated with energetic protons, *Phys. Rev. B* **18** (1978) 3015–3025.

[86] B. T. A. McKee, S. Saimoto, A. T. Stewart and M. J. Stott, Positron trapping at dislocations in copper, *Can. J. Phys.* **52** (1974) 759–765.

[87] D. Setman, Lattice defects in HPT processed fcc nanometals studied by differential scanning calorimetry, Doctoral thesis, Vienna University, Austria, 2010.

[88] Y. Amouyal and E. Rabkin, A scanning force microscopy study of grain boundary energy in copper subjected to equal channel angular pressing, *Acta Mat.* **55** (2007) 6681–6689.

[89] K. Detert and G. Dressler, Rekristallisationsverhalten von zonengeschmolzenem Nickel, *Acta Metall.* **13** (1965) 845–853.

[90] W. Q. Cao, C. F. Gu, E. V. Pereloma and C. H. J. Davies, Stored energy, vacancies and thermal stability of ultra-fine grained copper, *Mater. Sci. Eng. A* **492** (2008) 74–79.

[91] Y. Amouyal, S. V. Divinski, L. Klinger and E. Rabkin, Grain boundary diffusion and recrystallization in ultrafine grain copper produced by equal channel angular pressing, *Acta Mat.* **56** (2008) 5500–5513.

[92] X. Molodova, G. Gottstein, M. Winning and R. J. Hellmig, Thermal stability of ECAP processed pure copper, *Mater. Sci. Eng. A* **460-461** (2007) 204–213.

[93] F. Phillipp, B. Saile and K. Urban, Investigation of vacancy diffusion in niobium, molybdenum and tantalum by means of high-voltage electron microscopy, Point Defects and Defect Interactions in Metals. Proceedings of the Yamada Conference V (J.-I. Takamura, M. Doyama and M. Kiritani, eds.), North-Holland, Amsterdam, 1982, pp. 261–264.

[94] P. A. T. Olsson, Semi-empirical atomistic study of point defect properties in BCC transition metals, *Comput. Mater. Sci.* **47** (2009) 135–145.

[95] I. Kaur, Y. Mishin and W. Gust, Fundamentals of grain and interphase boundary diffusion, 3rd ed., Wiley, Chichester, 1995.

[96] E. Schafler and R. Pippan, Effect of thermal treatment on microstructure in high pressure torsion (HPT) deformed nickel, *Mater. Sci. Eng. A* **387-389** (2004) 799–804.

[97] Z. Q. Yang, Effect of dynamical heating on microstructure and microhardness of Ni processed by high-pressure torsion, *Mater. Lett.* **60** (2006) 3846–3850.

[98] S. V. Divinski, G. Reglitz, H. Rösner, Y. Estrin and G. Wilde, Ultra-fast diffusion channels in pure Ni severely deformed by equal-channel angular pressing, *Acta Mater.* **59** (2011) 1974–1985.

[99] R. Birringer, C. E. Krill and M. Klingel, Orientation-phase-spaced-averaged properties of grain boundaries, *Philos. Mag Lett.* **72** (1995) 71–77.

[100] C. E. Krill, L. Helfen, D. Michels, H. Natter, A. Fitch, O. Masson and R. Birringer, Size-dependent grain-growth kinetics observed in nanocrystalline Fe, *Phys. Rev. Lett.* **86** (2001) 842–845.

[101] Y. Kuru, M. Wohlschlögel, U. Welzel and E. J. Mittemeijer, Large excess volume in grain boundaries of stressed, nanocrystalline metallic thin films: Its effect on grain-growth kinetics, *Appl. Phys. Lett.* **95** (2009) 163112.

[102] M. I. Buckett and K. L. Merkle, Determination of grain boundary volume expansion by HREM, *Ultramicroscopy* **56** (1994) 71–78.

[103] K. L. Merkle, Quantification of atomic-scale grain boundary parameters by high-resolution electron microscopy, *Ultramicroscopy* **40** (1992) 281–290.

[104] L. S. Shvindlerman, G. Gottstein, V. A. Ivanov, D. A. Molodov, D. Kolesnikov and W. Łojkowski, Measurements of Equilibrium Vacancy Concentrations in Aluminum, *J. Mater. Sci.* **41** (2006) 7725–7729.

[105] H. Zhang and D. J. Srolovitz, Simulation and analysis of the migration mechanism of $\Sigma 5$ tilt grain boundaries in an fcc metal, *Acta Mater.* **54** (2006) 623–633.

[106] D. L. Olmsted, S. M. Foiles and E. A. Holm, Survey of computed grain boundary properties in face-centered cubic metals: I. Grain boundary energy, *Acta Mater.* **57** (2009) 3694–3703.

[107] D. Wolf and K. Merkle, Materials interfaces: Atomic-level structure and properties, Chapman & Hall, London, 1992.

[108] D. Wolf, Correlation between energy and volume expansion for grain boundaries in fcc metals, *Scripta Metall.* **23** (1989) 1913–1918.

[109] T. Ungár, E. Schafler, P. Hanák, S. Bernstorff and M. J. Zehetbauer, Vacancy production during plastic deformation in copper determined by in situ X-ray diffraction, *Mater. Sci. Eng. A* **462** (2007) 398–401.

[110] M. J. Zehetbauer, J. Kohout, E. Schafler, F. Sachslehner and A. Dubravina, Plastic deformation of nickel under high hydrostatic pressure, *J. Alloys Comp.* **378** (2004) 329–334.

[111] H. J. Wollenberger, Point defects, in: Physical metallurgy, 4 ed., vol. 2, North-Holland Publishing Company, 1996.

[112] P. Ehrhart, Atomic Defects in Metals, in: Landolt-Börnstein: Numerical Data and Functional Relationships in Science and Technology - New Series / Condensed Matter, vol. 25, Springer, Berlin, 1991.

[113] R. Würschum, Struktur und Diffusionseigenschaften nanokristalliner Metalle und Legierungen, Habilitation thesis, Stuttgart University, Germany, 1997.

[114] S. V. Divinski, private communication, 2012.

[115] R. Lapovok, D. Tomus, J. Mang, Y. Estrin and T. C. Lowe, Evolution of nanoscale porosity during equal-channel angular pressing of titanium, *Acta Mater.* **57** (2009) 2909–2918.

[116] A. Scholz and A. Seeger, Verzerrungsfeld und mechanische Relaxation von Leerstellen in Germanium, *Phys. stat. sol. B* **3** (1963) 1480–1490.

[117] S. N. Khanna, B. K. Rao, P. Jena, D. Esterling and M. J. Puska, Atomic relaxations around vacancy clusters in molybdenum and their effects on trapped-positron lifetime, *Phys. Rev. B* **37** (1988) 6–11.

[118] J. Keckes, private communication, 2012.

Acknowledgement / Danksagung

Die vorliegende Arbeit entstand in den Jahren 2008 bis 2012 während meiner Tätigkeit als wissenschaftlicher Mitarbeiter am Institut für Materialphysik der TU Graz. Sie wäre nicht möglich gewesen ohne die Unterstützung der vielen nun folgenden Personen.

Mein besonderer Dank gilt Herrn Prof. Dr. Roland Würschum für die Vergabe und Betreuung dieser Arbeit, die vielen Ideen, intensiven Diskussionen und Ermutigungen sowie das große Vertrauen in meine Fähigkeiten.

Herrn Prof. Dr. Rainer Birringer danke ich vielmals für die Co-Begutachtung dieser Dissertation.

Herzlich bedanken möchte ich mich bei Prof. Dr. Wolfgang Sprengel für die fruchtbare Zusammenarbeit, die vielen anregenden Diskussionen sowie die Unterstützung in allen erdenklichen Bereichen, angefangen von den Positronenmessungen in Garching bis hin zum alltäglichen Laborbetrieb.

Herrn Prof. Dr. Reinhard Pippan danke ich für die gute Zusammenarbeit während meines Aufenthalts am Erich-Schmid Institut in Leoben, für die hervorragende und unbürokratische Kooperation im Rahmen des NFN-Projekts sowie für die zahlreichen wertvollen Ideen und Diskussionen.

Herrn Prof. Dr. Michael Zehetbauer bin ich für die ausgezeichnete Leitung und Organisation des NFN-Projekts sowie für die gute Zusammenarbeit zu großem Dank verpflichtet.

Herrn Prof. Dr. Christoph Hugenschmidt sowie Herrn Dr. Philip Pikart danke ich für die Messungen am Positronenstrahl des FRMII und die hervorragende Zusammenarbeit.

Meinen Kollegen in der Nano-Arbeitsgruppe Frau DI Eva-Maria Steyskal, Herrn DI Boris R. Scherwitzl, Herrn DI Bernd Lorenzoni, Herrn DI Peter Parz und Herrn DI Xiang Zhou danke ich sehr herzlich für die produktive wissenschaftliche Zusammenarbeit und die vielen fruchtbaren Diskussionen.

Ganz besonders möchte ich mich bei den Mitarbeitern und Mitarbeiterinnen des Erich-Schmid-Instituts in Leoben für die kollegiale Aufnahme ins Team bedanken. Im Speziellen bedanke ich mich bei Dr. Anton Hohenwarter, Dr. Andrea Bachmaier, DI Doris Luef und DI Oliver Renk für die Hilfe bei der Elektronenmikroskopie, bei Dr. Andrea Bachmaier auch für die TEM Bilder von HPT-Ni, bei DI Peter Kutlesa für die HPT-Verformungen und bei Silke Modritsch, Edeltraud Haberz und Gabriele Moser für die oft aufwändigen Probenpräparationen.

Frau Dr. Daria Setman danke ich sehr herzlich für die gute Zusammenarbeit im Rahmen der DSC- und RER-Messungen an HPT-Cu und Fe sowie für die Probenpräparationen von HPT-Cu.

Herrn Dr. Clemens Mangler danke ich für die TEM-Bilder von HPT-Cu.

Herrn Prof. Dr. Jozef Keckes danke ich für die Untersuchungen zu Makrospannungen in HPT-Ni sowie für die anregenden Diskussionen.

Meinem Diplomarbeitsbetreuer Herrn Prof. Dr. Werner Puff danke ich herzlich für die Positronenmessungen an HPT-Fe sowie für die wertvollen Anregungen im Rahmen der Auswertungen.

Herrn Prof. Dr. Ulrich Brossmann danke ich für die Hilfe bei den XRD-Messungen und die vielen Diskussionen.

Herrn Univ.-Doz. Dr. Peter Pölt und Herrn DI Klemens Jantscher danke ich für die EBSD-Bilder von HPT-Ni und Cu.

Herrn DI Martin Luckabauer danke ich für die Erstellung der CAD-Skizzen in dieser Arbeit sowie die vielen interessanten Gespräche.

Bei Herrn Thomas Friedl vom Institut für Werkstoffkunde und Schweißtechnik bedanke ich mich für das chemische Ätzen der Tantalproben.

Frau Katrin Unger, Frau Katrin Koren und Frau Anna Weitzer danke ich für die gute Zusammenarbeit im Rahmen ihrer Bakkalaureatsarbeiten.

Allen Mitgliedern des Instituts für Materialphysik danke ich für die angenehme Zeit, insbesondere möchte ich mich bei Frau Regina Steingasser für die stete Hilfsbereitschaft bei Verwaltungsangelegenheiten und bei Frau Eva Kniewasser für die Hilfe bei Werkstatttätigkeiten und Bildbearbeitungen bedanken.

Meinen Eltern DI Dr. Dieter und Gertraud Oberdorfer danke ich für ihre fortwährende Unterstützung und ihr Interesse an meiner Arbeit.

Meiner Freundin Mag. Birgit Hofstadler danke ich von ganzem Herzen für ihre unermüdliche Unterstützung, für Motivation und Rückhalt.

Diese Arbeit wurde vom österreichischen Fonds zur Förderung der wissenschaftlichen Forschung (FWF, Projektnummer: P21009-N20) finanziert.